VTT PUBLICATIONS 343

A propeller-ice contact model

Harri Soininen

VTT Manufacturing Technology

Dissertation for the degree of Doctor of Technology to be presented
with due permission for public examination and debate in Auditorium K216
at Helsinki University of Technology (Espoo, Finland)
on the 15th of May, 1998, at 12 o'clock noon.

TECHNICAL RESEARCH CENTRE OF FINLAND
ESPOO 1998

ISBN 951–38–5227–X (soft back ed.)
ISSN 1235–0621 (soft back ed.)

ISBN 951–38–5228–8 (URL: http://www.inf.vtt.fi/pdf/)
ISSN 1455–0849 (URL: http://www.inf.vtt.fi/pdf/)

JULKAISIJA – UTGIVARE – PUBLISHER

Valtion teknillinen tutkimuskeskus (VTT), Vuorimiehentie 5, PL 2000, 02044 VTT
puh. vaihde (09) 4561, faksi (09) 456 4374

Statens tekniska forskningscentral (VTT), Bergsmansvägen 5, PB 2000, 02044 VTT
tel. växel (09) 4561, fax (09) 456 4374

Technical Research Centre of Finland (VTT), Vuorimiehentie 5, P.O.Box 2000, FIN–02044 VTT, Finland
phone internat. + 358 9 4561, fax + 358 9 456 4374

VTT Valmistustekniikka, Laiva- ja konetekniikka, Tietotie 1, PL 17051, 02044 VTT
puh. vaihde (09) 4561, faksi (09) 464 424

VTT Tillverkningsteknik, Skepps- och maskinteknik, Datavägen 1, PB 17051, 02044 VTT
tel. växel (09) 4561, fax (09) 464 424

VTT Manufacturing Technology, Maritime and Mechanical Engineering,
Tietotie 1, P.O.Box 17051, FIN–02044 VTT, Finland
phone internat. + 358 9 4561, fax + 358 9 464 424

Technical editing Leena Ukskoski

Libella Painopalvelu Oy, ESPOO 1998

Soininen, Harri. A propeller-ice contact model. Espoo 1998, Technical Research Centre of Finland, VTT Publications 343. 116 p.

UDC 629.1.037/.038:629.124.79
Keywords propellers, propeller blades, ice loads, loads (forces), icebrakers

ABSTRACT

The propeller-ice loads consist of both actual contact loads due to propeller penetration into an ice block and non-contact loads that are hydrodynamic disturbance loads generated by the presence of an ice block in the vicinity of a propeller. In this work the contact loads are studied experimentally during a milling type open propeller ice contact. A model of the ice failure process is developed based on the experiments. An effective load model is also developed in order to be able to calculate load levels.

In the laboratory experiments a tool having a propeller-like profile was attached to a pendulum and impacted with an ice sheet. The global loads on the tool and the pressure distribution along the tool profile at mid-depth of the ice sheet were measured. The failure process was observed. A process model was formed. The blade leading edge opens cracks towards the groove formed by the previous blade and accordingly the face side hardly experiences any contact at all. On the back side a spall is formed and the ice is crushed within the spall. In the case of large confinement local crushing may also occur instead of spalling. The crushed ice is extruded towards both the leading edge and the trailing edge of the profile. Two-dimensional behaviour is assumed.

The failure loads of solid ice are studied with slip-line theory using the Mohr-Coulomb failure criterion. The pressure distributions due to extrusion of crushed ice are studied using both viscous and granular models. The effective load of a section is considered to be the average of instantaneous loads during the process. A simplified method to calculate the effective load is formed for various contact geometry and ice strength parameters. The total load of a blade is the integrated effective loads of each section. The calculated total load is validated against some measured full-scale values. A relatively good result is achieved.

PREFACE

My attention was first directed to the propeller-ice interaction problem by Professor Ernst Enkvist at the end of 1986, when I was to start my assignment at Wärtsilä Arctic Research Centre (WARC). The background was the unique full-scale test series performed for IB Karhu a couple of years earlier in which the propeller blade load was measured simultaneously on a ducted and an open screw. In the winter of 1988, I participated in the complementing tests, where simultaneous measurements for two open screws with different diameters were performed on IB Sampo. The preliminary analysis of these tests gave me the basic understanding of the problems involved.

In 1991, the Canadian National Research Council and the Finnish Board of Navigation entered into an agreement on JRPA#6 (Joint Research Project Arrangement # 6) with the objective of developing a new physically justified propeller-ice interaction model. The model was further to be used as a basis for new Canadian Arctic and Finnish-Swedish machinery ice regulations. The bulk of the present research was conducted at the Technical Research Centre of Finland (VTT) within the JRPA#6 project. The experimental part was conducted in 1993 at the VTT Research Hall ice basin.

I wish to express my warmest thanks to the supervisor of this work, Professor Petri Varsta, who guided and supported me through all these years. His constructive criticism was an invaluable help for me in elaborating my work to its final form.

I am deeply indebted to many people for their kind contribution during the process of this work. As my superiors in VTT, Professor Juhani Sukselainen and Dr. Matti Hakala provided an excellent working environment. Mr. Matti Jussila, Mr. Pekka Koskinen and Mr. Sauli Liukkonen at VTT worked with me in the JRPA#6 team. Without their great support, this work would not have materialised. I have had the privilege and pleasure to increase my understanding of structure-ice contact problem through discussions with the researchers of the “ice community” at the Ship Laboratory of the Helsinki University of Technology (HUT), Professor Kaj Riska, Dr. Pentti Kujala, Dr. Jukka Tuhkuri and Dr. Brian Veitch, now at the Institute for Marine Dynamics (IMD). I have also had the opportunity for having fruitful discussions on the subject with Professor Claude Daley of the Memorial University of Newfoundland, Professor Mauri Määttänen of HUT and Dr. Valery Belyashov of the Krylov Shipbuilding Research Institute. The exchange of views with the Canadian team of JRPA#6, especially with Dr. Stephen J. Jones of IMD and Dr. Arno Keinonen of AKAC Inc., was a source of great inspiration.

During the experimental phase of the work, I was assisted by a team. The test arrangement was designed and the measurements performed by Mr.

Sauli Liukkonen. Mr. Panu Korri of Finnyards designed the test rig and supervised its manufacture at Finnyards. The PVDF measuring system was designed and the data recording performed by Mr. Ari Muhonen, who also prepared the thin section specimens. Mr. Risto Koskivaara performed the ice strength measurements. Various FE calculations of loaded ice wedges were performed during the work by Mr. Sauli Liukkonen, Mr. Kalle Kanervo and Mr. Keijo Koski. Mr. Matti Jussila performed verification calculations by the simulation method he developed, Mr. Pekka Koskinen assisted in processing the existing full-scale data for verification purposes and Mr. Jussi Martio assisted in the programming work for the simplified pressure calculations. Ms. Eila Moring assisted me in the finishing of the manuscript, Mr. Pentti Tuononen in the digital figure handling and Mr. Matthew Patey in the editing of the English text. I am deeply greatful for all of them.

This research has been funded through the Finnish part of the JRPA#6 by the Finnish Technology Development Centre (TEKES), VTT, the Finnish Board of Navigation, the Swedish Maritime Administration, Aquamaster-Rauma Oy, Finnyards Oy (originally Rauma Yards Oy), Finnscrew Oy, FG-Shipping Oy, ILS Oy, Neste Oy and Silja Line Oy. The work was further supported by the Maritime Foundation. This support is gratefully acknowledged.

Finally, I wish to thank my wife Kristiina and our children Eeva, Heikki and Jukka for all their support and patience during the years I have spent with this work.

Helsinki, March 1998
Harri Soininen

CONTENTS

LIST OF SYMBOLS

b_1	contact length along the arc of the leading edge
b_2	contact length along the face side
c	cohesion
C_1 , C_2	parameters for a spiral
d	grain diameter
d_{hub}	propeller hub diameter
D	propeller diameter
E	modulus of elasticity
F	load
h	thickness of an ice sheet, distance from the middle of the ice-propeller contact length of a section to the edge of the ice block in radial direction, width of a crushed ice channel
h_c	width of a crushed wedge tip
ho	the crushed ice channel thickness at x = 0
H	projection of the distance between the cinematic leading edge to the tangential point of contact at back side of the blade profile in y-direction
J	propeller advance ratio
k	correction factor, constant, lateral pressure coefficient
K	extrusion pressure coefficient
Ka	extrusion pressure coefficient for a sloping channel of crushed ice
K_T	propeller thrust coefficient
K_Q	propeller torque coefficient
L	length of a crushed ice channel
l	length of a spall
l_1	distance between wedge tips in x-direction
l_2	distance for the blade to proceed between two wedge tips
L_1 , L_2 , L_3 , L_4	part lengths of crushed ice channel
L’	part length of a crushed ice channel along the solid ice
M_b	propeller blade bending moment
n	propeller speed
p	pressure, normal pressure (Mohr-Coulomb criterion)
p_{av}	average pressure
p_c	critical pressure
p_L	wall pressure at the end of crushed ice channel
p_{LE}	the mean pressure at the leading edge
p_{MA}	the maximum value of average pressure distribution along a section
p_{max}	maximum pressure

p_r	critical peak pressure in radial direction (polar coordinates)
p_{WA}	the average pressure at a solid ice wedge tip during one cycle
p1 - p21	pressure sensors No 1 - 21
p_φ	pressure in φ-direction (polar coordinates)
pox	ice pressure in x direction at $x = 0$
Q	propeller shaft torque
Q_{net}	net mass flow
r	radius of a blade section, polar coordinate radius
S_c	uniaxial compressive strength
S_t'	nominal uniaxial tensile strength
T	temperature
u	speed of crushed ice flow in a channel
u_a	average speed of crushed ice flow in a channel
U	tangential speed of a profile surface
U_P	speed of a blade section in angle of attack direction
v	relative speed of blade profile surface against solid ice wall
V_1 , V_2	volumes of crushed ice
V_S	ship speed
w	cut width of ice
w_{b1}	maximum cut width of ice due to load in profile direction
X	the distance from leading edge of the maximum pressure along the section
Z	number of propeller blades
α	angle between blade profile surface and solid ice, slope angle of a crushed ice channel
α_A	angle of attack of a section
β	the angle between the angle of attack line and profile surface tangent direction
β_r	angle of advance of a section
Δt	a time increment
δ	angle of a secondary wedge
ε	strain
γ	the angle between the normal of the face side and the angle of attack direction
ϕ	internal friction angle
ϕ_r	pitch angle of a section
φ	polar coordinate angle
μ	ice-ice inner friction factor, friction coefficient, dynamic viscosity
μ_i	ice-ice friction coefficient
μ_0	viscosity in atmospheric pressure
μ_p	viscosity in pressure p

μ_s	ice-structure friction coefficient
σ	brittle uniaxial compressive strength
σ_1	major principal stress
σ_3	minor principal stress
σ_{horiz}	compressive strength of ice across grain direction
σ_{vert}	compressive strength of ice along grain direction
σ_{pc}	crack propagation stress
σ_y	stress in y-direction
σ_z	stress in z-direction
σ_φ	stress in φ–direction
τ	shear stress
τ_c	critical shear stress
τ_y	the rate independent shear stress in the viscoplastic flow model
ψ	angle between the fractured plane and maximum principal stress (Mohr-Coulomb criterion), angle between the angle of attack line and the solid ice wall
ζ	angle between a symmetry-axis and wedge surface
ω	wedge half angle

Abbreviations

ASME	American Society of Mechanical Engineers
CP	controllable pitch propeller
EAR	expanded area ratio
FE	finite element
FFT	Fast Fourier transformation
FP	fixed pitch propeller
IAHR	International Association for Hydraulic Research
IMD	Institute for Marine Dynamics
ISOPE	International Offshore and Polar Engineering Conference
OMAE	International Offshore Mechanics and Arctic Engineering Symposium
POAC	International Conference on Port and Ocean Engineering under Arctic Conditions
PVDF	polyvinylidene difluoride
SNAME	The Society of Naval Architects and Marine Engineers

1 INTRODUCTION

1.1 SCOPE OF THE WORK

The contact loads that a marine propeller encounters in a propeller-ice interaction event are analysed in this work. Propeller ice interaction is an extremely complicated process. The propeller load is based both on direct contact forces due to the penetration of the blade into an ice block, and hydrodynamic non-contact loads. The dynamics between the block and the propeller affects the build-up of the load during several blade passes. The ice block size, location and orientation in relation to the blade influence the dynamics. The exposure of the blade is affected by the operative conditions of the vessel and the design of the after body in relation to the propeller. The major factors are the location of the propeller, and whether the vessel has one or two screws. The relative magnitude between the contact and non-contact loads is affected by the propulsion concept, i.e. open propeller vs. ducted design. The total propeller-ice load can be achieved with a simulation process, Koskinen et al. (1996), Veitch (1995), Figure 1. The propeller geometry, ice block geometry, pitch angle, ship speed and propeller speed give the contact geometry conditions at any moment. The contact geometry, in turn, affects the magnitude and distribution of both contact and non-contact loads. The force balance changes the velocity pattern of the ice block and accordingly the contact geometry.

This work was carried out in the context of a joint Canadian Finnish research project (JRPA#6, Propeller Ice Interaction, in 1991 - 1996) that was aimed at developing a new physically justified propeller-ice interaction model to be further used in formulating new machinery regulations for Arctic and Baltic ice conditions. The aim of the present work is to develop a model that describes the ice propeller contact load process. The non-contact loads, which can be of meaningful magnitude, Koskinen et al. (1996), and the dynamics between the blade and ice block are outside the scope of the work. The contact load model may be used as input in the simulation process mentioned above. The model is to be based on accepted physical phenomena and be able to predict the effective load level and distribution. The approach taken is to develop a model describing the contact process, called the process model here onwards, formulate the physical relationships between the elements of this process model, and verify the model by performing effective load calculations of known full-scale measurement events, Figure 2. As background for the process model a test series was performed for this work, Soininen et al. (1995), in which the pressure distribution was measured along a propeller blade profile impacting ice.

The work is restricted to open propellers and milling type contact, in which contact exists between the ice block and the leading edge of the propeller blade. The main emphasis is on the load at the back side of the blade

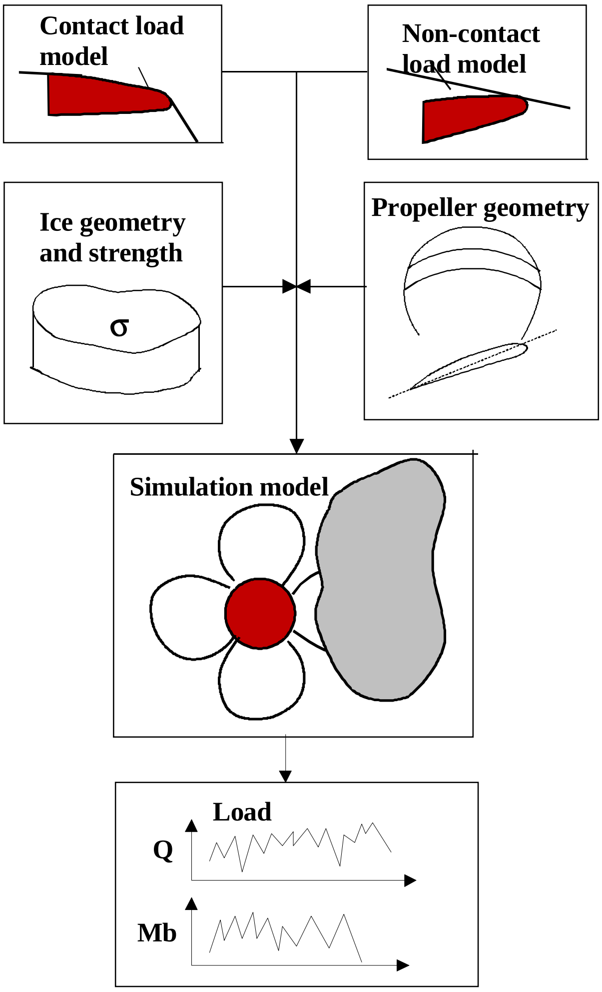

Figure 1. Schematic presentation of the overall propeller ice load simulation model.

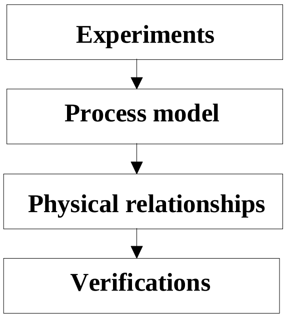

Figure 2. The approach used in the work.

because both full-scale and laboratory tests indicate that the maximum loads bend the blade astern in normal ship operating conditions. The model is developed for two-dimensional contact of propeller blade sections. The total contact load is achieved by integrating the individual section loads. The two-dimensionality assumption is corrected at the tip sections of the propeller and at sections that are close to the free edge of the ice block.

The proposed model assumes the contact load distribution to be developed by extrusion mechanisms of crushed ice, whereas the maximum load levels are governed by the stress state that the surrounding intact ice can sustain without failure. Failure is assumed to take place by spalling or local crushing. The slip surface emergence and geometry that form the spall depend on the confinement conditions of the pressure distribution. The ice is crushed within the spall and a new geometry for a channel of crushed ice is formed. This geometry, in turn, affects the extrusion and pressure distribution. The proposed model is new in the respect that it is the first one that attempts to describe the process during the actual contact. The effective load that a section experiences is considered to be the mean of instantaneous loads during various phases of the process. The model cannot be directly verified against full-scale measurement results, because the existing full-scale measurements are response measurements. It is not, for example, possible to distinguish clearly between the hydrodynamic non-contact loads induced by the presence of ice blocks and the actual contact loads. The verification must thus take place by means of an overall simulation model. However, the results of the laboratory pressure distribution tests made for this work in order to isolate the pure contact loads are available for limited verification, although it has to be remembered that the model itself is based on these tests.

1.2 PROPELLER-ICE CONTACT GEOMETRY DEFINITIONS

The contact loads are usually separated into milling- or impact-type loads. The difference between these is not very clear. The load has often been classified as a milling load if the contact lasts more than one revolution, i.e. if the same blade hits the ice block more than twice. In this work, the contact is always considered to be of the milling type when the leading edge of the blade comes into contact with ice, even if the ice block is small and the contact does not last more than one blade pass. If the blade and ice block velocity geometry is such that the block hits the blade at the back or face side, without leading edge contact, the contact load is classified as an impact load.

Different quadrants for the operational condition of a propeller are defined by the ratio between the direction of propeller rotational speed and advance speed. For a FP propeller the quadrants are shown in Figure 3. The I quadrant, where the ship is running ahead and the propeller thrust acts ahead is of course the most common case. The leading edge of the propeller blade comes into contact with ice and thus the interaction is usually milling-type. An impact contact is also possible in I quadrant if there is a slight negative angle of attack at some radia and a small ice block bounces from one blade to the back of the next blade. The backing situation, III quadrant, is in principle similar to I quadrant, in that the trailing edge comes into contact with ice. The other quadrants are related to manoeuvring situations of the ship in which the propeller thrust and the ship speed act in opposite directions. The ice comes into contact either at the blade face or back side. The situation differs in the case of a CP propeller; the quadrants II and III are not possible, Figure 4. The interaction type changes according to the pitch of the propeller.

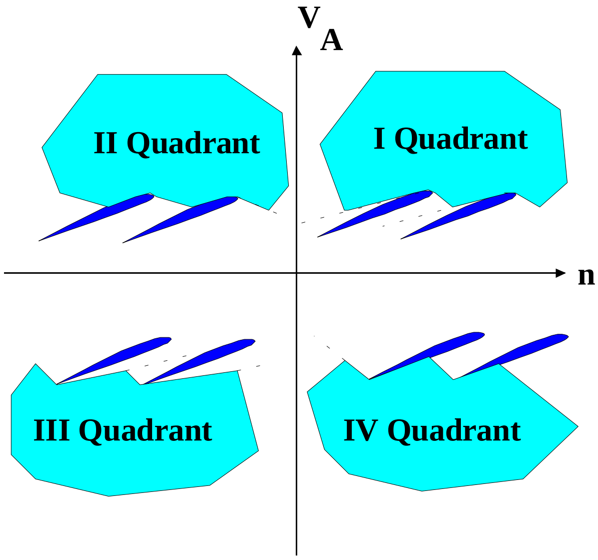

Figure 3. Interaction quadrants between ice and a FP propeller.

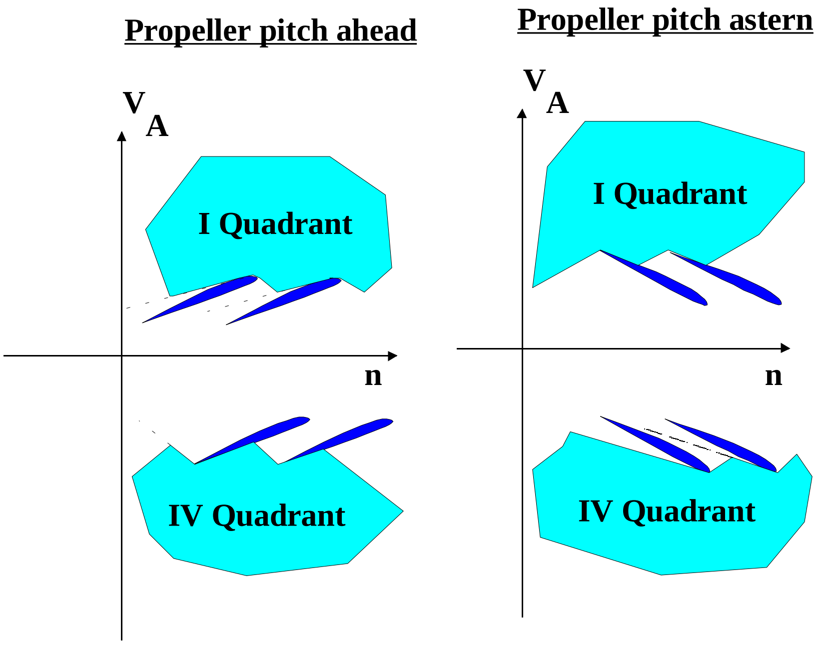

Figure 4. Interaction quadrants between ice and a CP propeller.

As stated above the process model in this work is restricted to milling type contact and situations in which the ship and propeller are proceeding in the same direction: for a FP propeller quadrants I and III, and for a CP propeller quadrants I in pitch ahead mode and IV in pitch astern mode.

The contact geometry between an ice block and the blade back side depends on the angle of attack as shown in Figure 5. The angle of attack is accordingly one of the main parameters in contact load calculations. It is, however, not well known in practice, since the actual wake factor at the disk level in ice conditions is not known. The propeller can accelerate the ice block before contact or the ice block can be supported by other ice blocks. Therefore an apparent angle of attack is used to indicate the contact geometry in this work, assuming the ice block enters into contact at the ship speed, V_S, see Figure 5, and the wake factor to be thus zero.

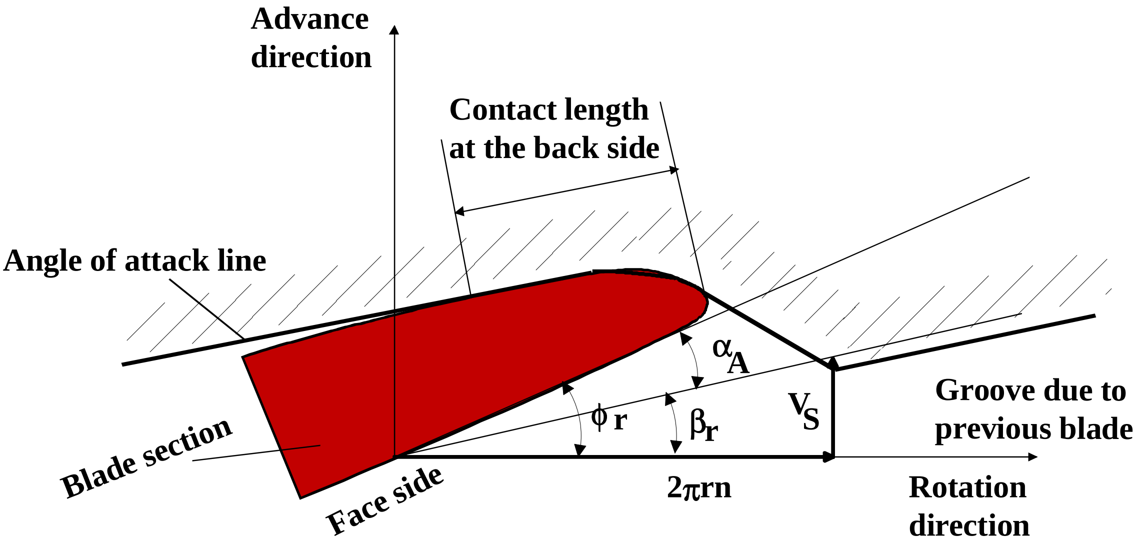

Figure 5. Contact length between ice and the back side of a blade section. α_A *is the apparent angle of attack for the blade section,* V_S *is the ship speed, n is the propeller speed, r is radius of the section,* β_r *is angle of advance of the section and* ϕ_r *is the pitch angle of the section.*

1.3 REVIEW OF EXISTING MODELS

1.3.1 Ice failure against an indentor

Two basic scenarios of ice failure caused by an indentor exist. The first scenario, the layer or finite failure model, assumes a layer of crushed ice between the indentor and the solid ice, Kurdyumov and Kheisin (1976), Timco and Jordaan (1987), Kärnä and Turunen (1989). It is assumed that when the crushed ice is extruded the crushed ice channel narrows and the pressure rises. Microcracks start to grow in the solid ice, subsequent growth and coalesence of micro-cracks creates granular material and the crushed ice forms a layer at some depth.

The second basic scenario assumes contact through a line-like high pressure or “hot spot” contact area and accordingly failure by flaking, for example Joensuu and Riska (1989), Riska (1991), Fransson et al. (1991), Daley (1991) and Tuhkuri (1996). The flakes are either removed whole or in the case of some confinement the ice is crushed and extruded. Crushing between macrocracks has been reported from some indentation tests, both from field tests, Meaney et al. (1991), and laboratory tests, Tuhkuri (1995). These tests have been performed at considerably lower speeds than what is the case in propeller ice interaction, but yet clearly in the brittle range. Daley et al. (1996) give as an explanation for the ice crushing mechanism in this condition that macro-cracks result in the rapid release of stress and the resulting tension waves may break up the material. One explanation may also be the changed conditions for the critical crack propagation stress. After the crack has formed the spall is loose from the parent ice mass, and the confining compressive stress due to the three-dimensional stress state may ease. The effect of compressive confining pressure on the crack propagation criterion in a triaxial load condition has been discussed for example, by Hallam (1986) and Hallam and Nadreau (1987). It has been shown that the compressive cracking is propagation controlled. The stress may have already reached nucleation level before the formation of the macrocrack. After the confinement in the flake is eased the critical propagation stress drops to the stress level already existent. In Tuhkuri´s (1996) model flakes are formed through initiation and growth of macro cracks. The crack initiation starts at a critical K_{IC} value. After developing, the flakes break and form the crushed ice. The cracking and subsequent flaking takes place as a cascade starting from the least confined ice edge towards the contact line. In the tests performed by Tuhkuri the solid ice had always a direct line-like contact with the structure.

Daley et al. (1996) suggest that depending on the conditions of the process several of the crushing scenarios described above may take place. Saeki and Ozaki (1980) discuss the qualitative failure process trends in the ice indentation of vertical structure against the ice edge. The various ranges can be labelled as crushing, intermediate and flaking. With small indentation speeds, most of the ice fails by crushing. When the speed increases, the area of crushed ice narrows and flakes start to form. The amount of flaking increases further with higher speeds. It is further proposed that a higher compressive strength increases the susceptibility to flaking. Consequently the colder the ice is, the more it fails by flaking. A ship propeller is working in conditions of fairly warm ice but, however, the speeds are high.

1.3.2 Milling-type propeller ice interaction models

Most of the existing propeller ice interaction models are based on continuous loads due to failure in a milling-type contact scenario. The models assume that the load mainly affects the face side of the blade. The models use very simplified approaches when defining the failure process. The models do not describe the failure process, rather they define the critical load. A literature review of existing propeller ice load models was performed by Jussila and Soininen (1991).

The first category of the models handles the problem using global blade loads caused by ice failure in either a crushing or shear mode against the blade or its projection in some direction. The load usually acts against the blade face side and is caused by shearing of ice to the groove formed by the previous blade. The first published propeller ice interaction calculation method was the classical Jagodkin (1963) model of this type. Some of the more recent models are based at least partially on the Jagodkin model. In his model the first component is, as described above, the load from the face side due to shear failure of ice. The other load component is caused by crushing failure generated by the blade projection in the pitch direction. In some overload conditions where propeller speed has decreased considerably a pure crushing is applied to the projection of the blade in the advance direction. Simple uniaxial shearing and crushing strength values are used. The model is calibrated with some full-scale shaft torque measurements and simultaneous measurements of milled ice block dimensions. Ignatiev (1964) developed a model for calculating the required strength of an icebreaker propeller blade. The ice loads in the milling process are determined even more simply than in the Jagodkin model. They are based on an assumption of the ratio between the open water bollard torque and ice torque. The torque is converted into a force bending the blade at an assumed radius. In addition the axial ice load component is determined based on the thickness of the cut ice layer between successive blades and the strength of the ice without any consideration of the actual failure mode, i.e. shearing or crushing. The present propeller ice regulations are usually based on the ice torque principle. The shaft torque that is caused by the ice has been measured in full-scale, and converted to an ice load acting on the blade using certain assumptions and simplifications. Noble and Bulat (1981) discuss the differences between results of full-scale tests and the Jagodkin model. The main contradictions are the observed blade loads that bend the blade backwards even if the vessel is proceeding ahead. This is explained by shifting the load from the blade face side to the back side according to changes in the angle of attack during the blade milling. The study is made in a projection that is parallel to the plane of the ice floe. Laskow and Revill (1986) analyse the results of M/S Robert Lemeur full-scale propeller measurement data. The main emphasis is on the impact load scenario. The milling scenario is handled briefly. The assumption is that in practice all of the milling load acts as an in-plane load, i.e. along the section. The load is calculated in principle similarly to the crushing load in Jagodkin’s model.

The second category of the models equates the internal energy needed for the failure of ice to the external energy that is caused by the pressure against the blade when it moves. The blade is modelled with cylindrical strips. The ice is assumed to fail independently against each of these strips. The total load is integrated from each section. Sasajima and Mustamäki (1984) have based their model on shear failure of ice. The shear failure produces prism-like ice flakes. Depending on the thickness of the slice to be cut away the failure takes place at the face side either towards the groove of the previous blade or towards the bottom surface of the ice floe. At zero angle of attack the failure can also take place from the back side towards the bottom surface of the ice floe. A value for ice shear strength is assumed. The external energy is defined using a nominal contact pressure and the dimensions of the section strips. Kotras et al. (1985) discuss the effect of the difference in contact geometry between the blade and ice depending on the operating quadrant. The method is in principle applicable to all quadrants. The section geometry is simplified with plane facets. The geometry of ice that has to be removed by an individual blade to the groove formed by the previous blade is handled with cantilever analogy. The penetration starts with pure crushing and continues with either bending or shearing. Detailed information is given only for the crushing mode. The internal energy that is needed to crush a certain volume of ice when the blade moves a distance is equated to the external energy. The equation for internal energy contains an assumed crushing strength of ice. The external energy is formed from normal and tangential (frictional) forces that act against the strip when the blade moves.

A more rigorous analytic approach to the failure stress at the face side has been used in the next category of models. Belyashov and Shpakov (1983) and Belyashov (1993) present a method that takes into account the stress state around the blade more accurately than most of the models. Some tests performed with a propeller blade-like tool are the basis for the model. The ice was found to flake towards the free ice edge at the face side of the blade. The flaking took place immediatelly behind the leading edge. A load model that bends the blade towards the back side is developed. The load at the back side is not modelled, though it is considered to be important in some loading geometries. The failure stress required for a flake to form is defined with a parabolic rule, shear stress squared being a function of compressive stress to the first power. Both frictional and normal components of pressure against the blade are considered. The contact conditions for various propeller ice velocity conditions are discussed. Veitch (1992), (Veitch and Laukia, 1993) has assumed in his early model a similar face side failure mechanism as Belyashov and has applied a steady contact pressure along the back side contact length. The various load components are integrated on each section and the total propeller load is integrated from each section.

In one published method, Chernuka et al. (1989), the stress distribution in the ice that surrounds the propeller has been estimated by FE analysis. The load is defined for two-dimensional sections. Three contact scenarios are considered: shearing at the face side towards the previous groove resulting in a point load at the leading edge, crushing at the back side and crushing at the face side if the distance to the previous groove is large compared to the projected width of the section in the advance direction. Corresponding simplified indentation geometries are used for the FE analysis. The contact pressure distribution for each scenario is calculated using prescribed displacements. The pressure distributions for each scenario are tabulated as a function of contact length, curvature and distance to the groove formed by the previous blade. The values are normalised against the uniaxial crushing strength of ice. A computer program is developed to calculate the integrated loads for the whole blade.

The latest models take into account the dynamics between the ice block and the propeller and use a simulation type approach illustrated in Figure 1. Veitch (1995) has used as the basis of his model a test series with blade-like tools. The conceptual basis of the experiments was provided by the work of Belyashov and Shpakov (1983), which was extended. The pressure distribution at the leading edge area was analysed computationally with boundary element models. A Hertz-type contact pressure distribution was developed for the leading edge area and extended for longer contacts towards the trailing edge. The maximum pressure distribution used in the model concentrates on the leading edge area. Ice failure at the leading edge is characterised by an ice chipping process. On the back side the ice failure is explained to be mostly due to coalescence of small cracks. A spherical shaped ice-block is used in the blade-ice dynamics calculations. The calculation of non-contact load component uses the openwater K_T and K_Q parameters applied for a nominal J of the disk area not obstructed by ice and for a blocked flow J of the disk area obstructed by ice. The simulation runs are verified by some available full-scale measurements. Koskinen et al. (1996) and Soininen et al. (1998) have published a method that is in principle similar. Some of the early results of the present work have been used for the contact model. The non-contact model is based on some model and cavitation tests in the blocked condition (Newbury et al. 1993, 1994, Newbury 1996, Walker and Bose 1994). The ice block propeller dynamics simulation is performed for a variety of propeller and ice block dimensions and verified with the M/S Gudingen full-scale data (Koskinen and Jussila 1991). Finally the results of the parameter runs are transferred to simple regression type load equations.

1.3.3 Impact-type propeller ice interaction models

A few impact-type approaches have also been published. In Wind´s model (1983) the maximum probable size of an impacting ice block is first calculated based on ice thickness and ship breadth. The linear momentum of the ice block is calculated. The impact force is calculated assuming the velocity difference between the ship and ice becomes zero in a time interval that is defined to be a certain fraction of one revolution of a propeller. The impact is considered to take place against the back side of the blade. The model does not include any effect of rotation of the block or cutting. Laskow and Revill (1986) have worked out formulas both for ducted and open propellers. For ducted propellers both an elastic impact and plastic impact are considered. In the elastic model the elastic behaviour outside the contact zone is used. A wedge-like impact geometry is used in the plastic model. The eccentricity of the impact and the limiting force due to splitting the ice block are taken into account. For a single impact at zero pitch for open propellers a momentum equation similar to Wind´s model is used. For a single impact at nonzero pitch for an open propeller the ducted propeller plastic impact approach is used. Kannari (1994) assumes in his model that the loads that bend the blade ahead originate from impacts. The ice blocks are either sucked into the propeller disc between two successive blades or cracked loose from a parent ice block by leading edge contact. The blade force is calculated with a momentum equation similar to Wind´s model. The relative velocity between the blade and ice block is based on propeller speed and ship speed. The duration of the impact is based on full-scale propeller ice load measurements of IB Sampo. The block shape has been varied. The contact pressure is considered to be constant regardless of the contact area. The model is calibrated against some full-scale measurements.

2 PROPELLER-ICE CONTACT EXPERIMENTS

2.1 GENERAL

A lot of full-scale tests have been performed in which global shaft and blade ice loads are measured. Results have been published by Jussila (1983), Laskow and Revill (1986) and Laskow et al. (1986), Kannari (1988), Jussila and Koskinen (1989a, 1989b), Koskinen and Jussila (1991) and Kannari (1994). The measurements are, however, strain-gauge response measurements, where the strain is transformed into the blade load. Calibration has been possible only against loads that bend the blade in its weakest direction. Full-scale tests are extremely valuable and give an understanding of the load magnitudes, the statistics of the magnitudes, the location of the concentrated load on the blade and contact dynamics. However, it is not possible to get an insight into the origin of various types of loads. Which part of the load is produced by the ice propeller contact itself and which part of the hydrodynamic disturbance loads is due to the presence of an ice block?

A multitude of laboratory tests with propeller models have also been reported. Enkvist and Johansson (1968) performed tests in a circulating water tank. Milling, impact and indentation tests using ice fed into a model propeller rotated by a lathe are reported by Airaksinen (1970), Edwards (1976), Sasajima et al. (1981), Okamoto et al. (1981a, 1981b), Sasajima and Mustamäki (1984), Bulat et al. (1985) and Sasajima (1985). Results of model tests in ice basins are reported by Juurmaa and Segercrantz (1981), Keinonen and Browne (1990), Browne et al. (1991), Browne and Keinonen (1991), Newbury et al. (1993, 1994) and Newbury (1996). There exist also a few test series with propeller blade profile-like tools. Belyashov and Shpakov (1983) have performed impact tests and observed the failure phenomena varying the angle of attack. Jussila (1991) has performed impact cutting tests with realistic blade speeds, up to 30 m/s, and measured the global loads. Several test parameters are varied. Veitch and Kivelä (1993) and Veitch (1994, 1995) report a test series of blade-like tools at a cutting speed of 0.13 m/s. Tool shape, angle of attack and some other parameters are varied. The global loads are measured.

None of the tool type laboratory tests give information on the load distribution along the blade profile. In order to get more insight into the contact phenomena and load distribution it was therefore decided that a new test series should be performed. Since results of basic tests with profile-like tools were available it was considered that a test type that more closely simulates the actual propeller ice interaction event should be used for the present work. The aim was to measure pressure distribution along the blade profile using realistic impact speeds. These tests and their results have been reported briefly by Soininen and Liukkonen (1994) and Soininen et al. (1998) and in a test report by Soininen et al. (1995).

2.2.1 Test set-up

The tests were performed in an ice tank. The testing equipment consisted of a massive pendulum, to which an instrumented tool was attached, Figure 6. The tool represented a part of the propeller of MS Gudingen in a 1:1 scale. The reason for selecting this profile geometry was that the most extensive available full-scale measurements are those of MS Gudingen, Koskinen and Jussila (1991). The pendulum gave the tool its velocity.

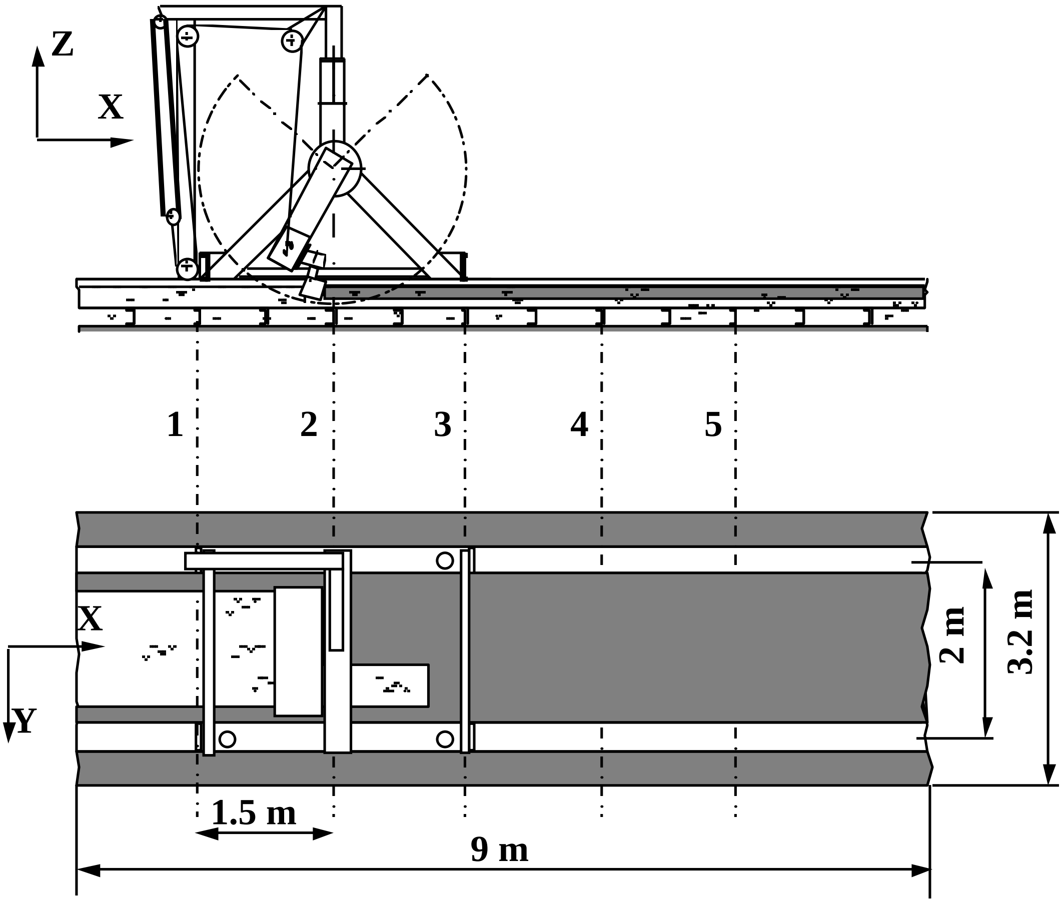

Figure 6. Schematic presentation of the test rig and the test set-up. Numbers 1 to 5 indicate the location of the test rig for each set of tests within an ice field.

In principle the brittle range of failure is reached at a specific strain rate and higher strain rates do not affect the strength of the ice. On the other hand, realistic propeller speeds result in far higher strain rates than most of the test data of uniaxial ice compressive strength. It was considered that high impact speeds as well as the opportunity to use also lower speeds could give insight into the phenomena. A pendulum is the simplest means of producing a high controlled impact speed. The pendulum arrangement also results in a rotational movement of the blade thus simulating the real propeller-ice contact. The pendulum mass was approximately 1500 kg. The drop height of the centre of gravity was 2 m, which was the maximum that the free height of the tank allowed. The maximum tangential blade speed at the time of the first contact with ice was accordingly about 8.3 m/s. At the end of the contact the tangential speed was about 7.5 m/s. This is about one third to one half of the tip speed of actual propeller blade profiles. However, this speed was considered to give realistic load values. In Jussila´s (1991) tests the increase in longitudinal force is some 25 % and the increase in transversal force within the scatter, when the cutting speed is increased from 9 m/s to 24 m/s. The available kinetic energy in the present tests was 29 kJ. The tool impacted with an approximately 20 cm thick ice field. The shape of the tool is presented in Figure 7. The blade profile was covered with a layer of Inerta 160 epoxy paint, about 2-3 mm thick, and thus the actual blade shape differs slightly from the propeller, being somewhat thicker. The blade was welded into a stiff 110 mm diameter shaft. The shaft in turn was attached to a base plate with a conical joint, which allowed the angle of attack to be adjusted to any desired value. The base plate was bolted onto the pendulum mass, and it could be moved in the transverse direction.

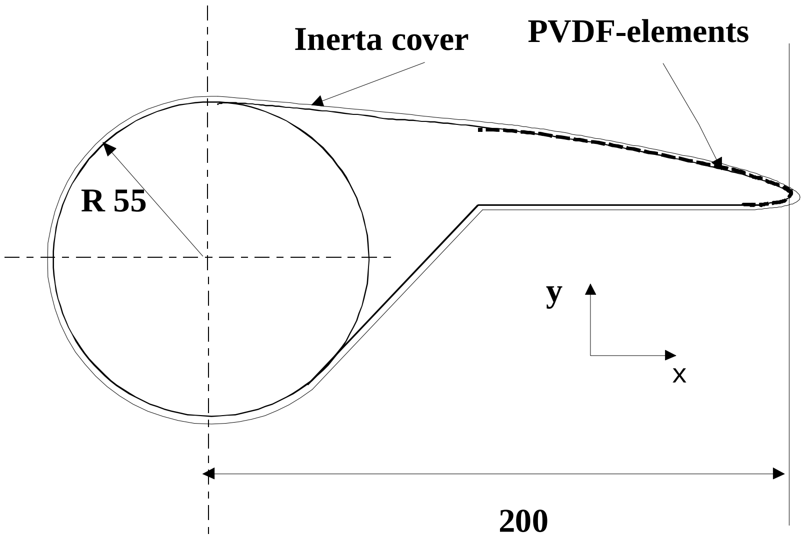

Figure 7. The shape of the used propeller blade profile used, attached to a stiff steel shaft.

2.2.2 Measurements and observations

The ice pressures against the tool were measured with 21 pressure-sensitive polyvinylidene difluoride (PVDF) elements. Both longitudinal and transversal accelerations were recorded. The total blade profile ice forces were measured from the shaft using strain gauges. The measured components were torque, longitudinal and transverse forces and bending moments. The position of the pendulum was recorded with a pulse transducer, and the same signal was used to define the speed of the profile. The signals were recorded with analog tape recorders and afterwards digitised with frequency of 104 000 Hz/channel. The tape speed used covered a frequency band up to 10 000 Hz.

PVDF film has been used earlier in several test series to measure local ice pressures, Joensuu and Riska (1989), Riska et al. (1990) and Muhonen et al. (1992). The PVDF elements were integrated into one big sheet. The signals were led to the top of the profile with small silver paste cables. The whole sheet was glued on to the surface of the tool. Five out of the 21 elements failed, four at the construction phase and one during the tests. The locations of the pressure elements at the back side and leading edge plus the strain gauges are shown in Figure 8.

Four of the tests were observed with high speed film with a frame interval of about 0.8 ms. Thin section photographs were produced of the impacted ice associated with each test type.

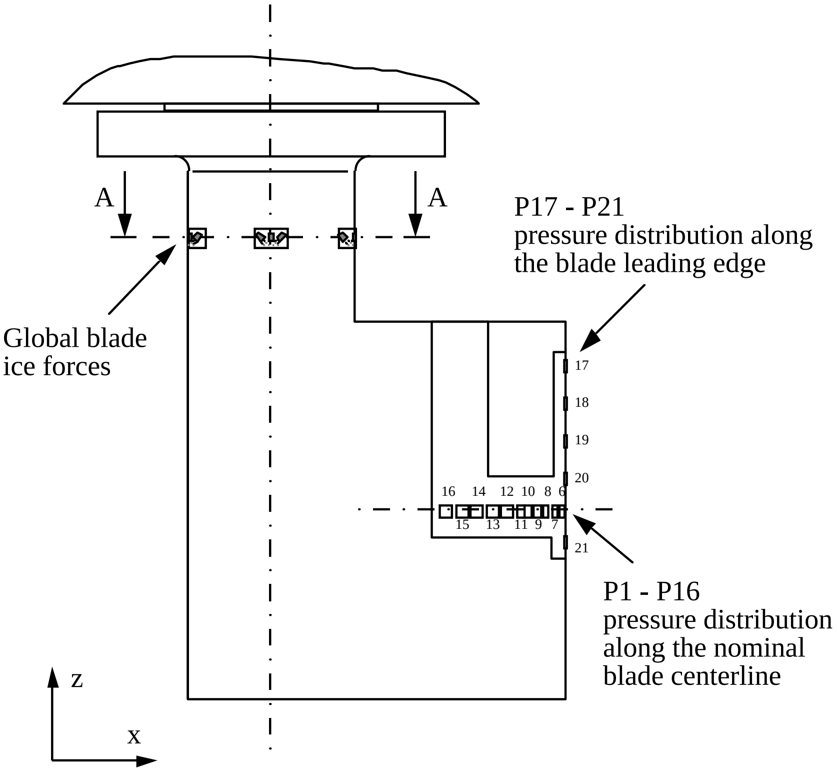

Figure 8. The pressure element and strain gauge locations.

2.2.3 Calibration

The PVDF elements were calibrated with an impact hammer. This method has been shown to give reliable results, Joensuu (1988). The overall accuracy of the PVDF measurement system was estimated to be about 15% based on the calibration results, temperature sensitivity and deviation of linearity, and measured to be less than 10 % up to 100 MPa, Joensuu (1988). The global force measurement system was physically calibrated with a 1.5 ton manual winch. The dynamics of both the rig and the blade profile were studied with impact hammer tests. The governing modes and their frequencies are listed in Table 1. The frequency content of the signals was studied against the natural frequencies of the test arrangement by performing a FFT analysis with a signal analyser. The longitudinal and transverse moment and acceleration signals plus the pressure signals of sensors No 7 and 9 were analysed. Three representative tests were analysed. The lowest natural frequencies of the test tool (200 - 300 Hz) were identified from the force and moment signals as well as from the accelerations. The transverse vibrations were more remarkable than the longitudinal. The pressure signals did not reveal any critical frequencies of the test arrangement. Thus it is considered that the pressure signals and the mean values of the force signals over some time periods can be used in the analysis without fear that they have been disturbed by critical frequencies of the test arrangement.

Table 1. Governing natural modes and frequencies of the test equipment.

Frequency / Hz	Mode
17	Transverse mode of the whole test rig
153	Torsion mode of the pendulum
222	Longitudinal cantilever beam mode of the tool (pivot point in attachment to the pendulum mass)
309	Transverse cantilever beam mode, as above
351	Longitudinal bending of the pendulum
959	Transverse bending of the blade profile (pivot point in attachment to the stiff shaft)

2.2.4 Ice

Natural low salinity sea water outside Helsinki was used in the tank. Saline water was chosen instead of fresh water in order to avoid the possibility of the impact producing extensive macrocracking that would have ruined the use of the ice sheet for subsequent tests. The S2-type ice sheets were produced in a temperature of about -20 °C up to a thickness of 20 cm. Altogether three sheets were produced. The mean salinity of the ice for each sheet was approximately 3 ppm. The water in the tank was cooled to about 1 °C by stirring. When the water surface started to freeze the ice was skimmed and the water seeded by spraying fresh water. The result was columnar grained ice with a thin top layer of granular ice. The grain size varied from 4 to 8 mm. The tests were performed at -8 °C air temperature. Four cold tests were performed in -20 °C air temperature immediately after the freezing period of one of the sheets. The ice temperature at the depth of the pressure sensors was in average -4.5 ^{o} C for the cold tests and -2.2 ^{o} C for the rest of the tests. Two tests were performed in massive ice that was produced from the second thin ice sheet by letting part of it grow during the freezing and testing period of the third sheet. A thickness of 36 cm was reached. The vertical temperature distribution naturally differed in the thin and massive ice sheets. Thus the temperature at the depth of the pressure sensors for the massive ice was -3.3 ^{o} C. The average uniaxial compressive strength was fairly low, 2 MPa in the grain direction and 1 MPa across the grain direction. For the colder ice the respective values are 4 and 2 MPa and for the massive ice 3.7 and 3.1 MPa. The compression tests were performed with a strain rate 2 x 10^{-4} s^{-1}.

2.2.5 Test parameters

Five longitudinal positions of the test rig could be used within each field, see Figure 6. The maximum amount of individual tests at each longitudinal position was four. Altogether 46 individual tests were performed. The main parameter that was varied in the tests was the angle of attack, α_A. It governs the contact length at the profile back side and, by assumption based on full-scale tests, the transverse load. Figure 9 presents the contact conditions and the main parameters, the angle of attack α_A and the cut width w. Other parameters which were studied were the cut width, the ice temperature, the impact speed, the grain direction and wet vs. dry contact. The original set-up of the tests did produce cracking and extrusion of crushed ice in the vertical direction towards the top and bottom level of the ice sheet. In the case of a propeller interaction with a massive ice block this is not possible. Therefore the set-up was changed and the effect of the spalling and extrusion direction was studied in two tests by confining the ice with a steel plate from the top level and letting the ice grow well below the test tool. The full test matrix is presented in Table 2.

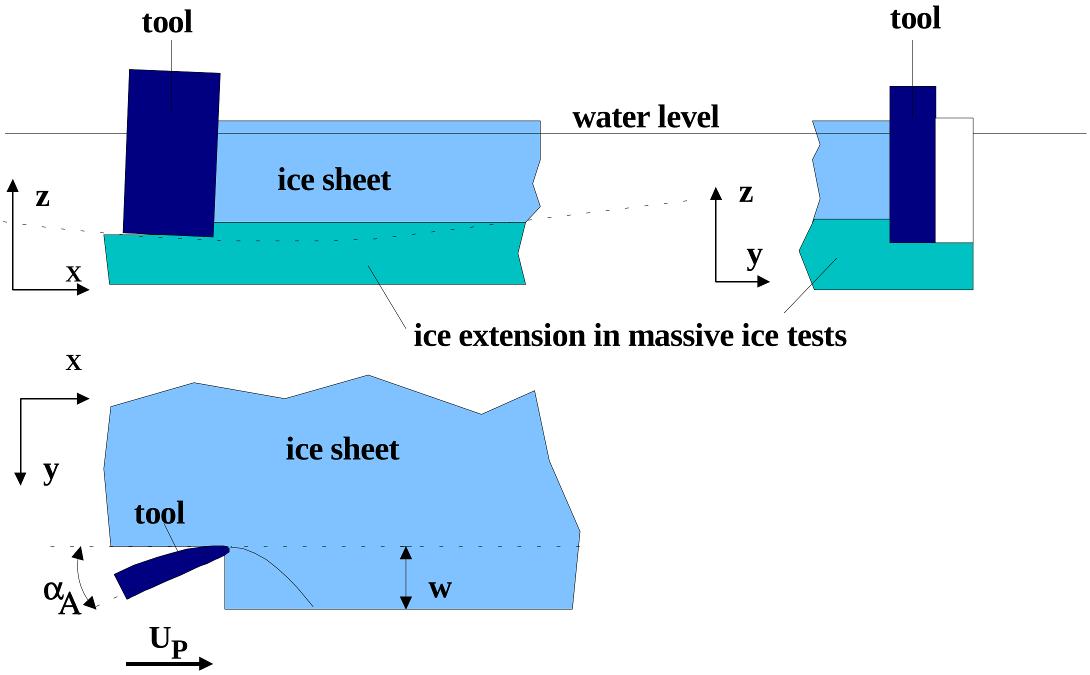

Figure 9. The contact conditions of the tests and the main parameters: α_A is the angle of attack, w is the width of the cut and U_P is the velocity of the blade profile in x-direction (angle of attack direction).

Table 2. The test matrix by test types.

Test type	No of individ. tests	Angle of attack°	Cut width mm	Blade speed target m/s	Ice temp. target °C	Grain dir.	Wet or dry
Basic	9	7	50	8.2	-2.2	Vert.	Wet
4°angle of attack	4	4	50	8.2	-2.2	Vert.	Wet
12°angle of attack	4	12	50	8.2	-2.2	Vert.	Wet
25° angle of attack	3	-25	220	8.2	-2.2	Vert.	Wet
100 mm cut width	5	7	100	8.2	-2.2	Vert.	Wet
0 mm cut width	2	7	0	8.2	-2.2	Vert.	Wet
	1	7	0	8.2	-2.2	Vert.	Dry
Cold tests	2	7	50	8.2	-4.5	Vert.	Wet
	2	7	50	8.2	-4.5	Vert.	Dry
Horizontal grains	2	7	50	8.2	-2.2	Horiz.	Wet
Dry tests	4	7	50	8.2	-2.2	Vert.	Dry
Slow impact speed	2	7	50	2.5	-2.2	Vert.	Wet
Massive ice	2	7	50	8.2	-2.2	Vert.	Wet

2.3 EXPERIMENTAL RESULTS

As explained above most of the tests were performed with impacts within relatively thin ice. Two tests were performed in massive, confined ice conditions. The massive ice is relevant for actual propeller design loads. Results of both test types are given since some results of the thin ice case are applicable also to the massive ice. The observed general process was a cyclic failure by cracking and extrusion of crushed ice. Observations of both basic mechanisms are presented below.

2.3.1 Cracking process of the solid ice

2.3.1.1 FACE SIDE

At the face side the tool hardly experienced any contact. When the tool proceeded, cracks were generated running from the leading edge to the open ice edge (representing the groove formed by the previous blade). The spalled ice was transferred gently aside by the face side. This process can be followed from the high speed film, Figure 10. (The resolution of the film is unfortunately rather poor. A video produced from the original film gives a better understanding of the process.) The face side pressure sensors give only a marginal pressure load, see Figure 11, that represents the average from all basic tests (11 test cases). The fact that the face side does not actually experience any meaningful loads is also found from the tests performed by Veitch (1994 and 1995), where ink is erased from a blade-like tool from the back side but not from the face side.

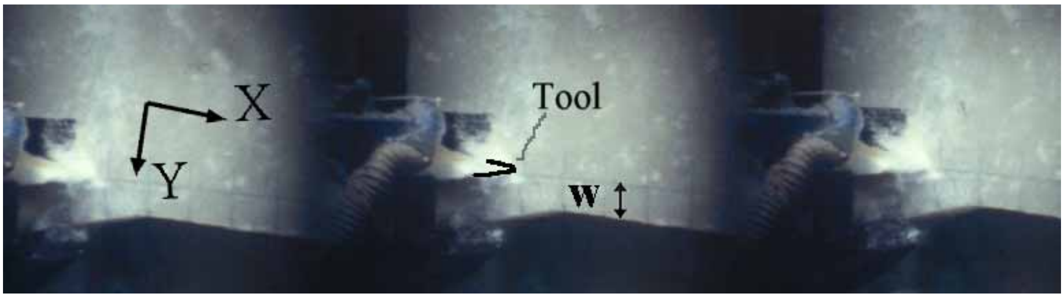

Figure 10. A set of three subsequent frames of the high speed film, test No 37, (dry, 50 mm cut width, 7 ^{o} angle of attack) showing the spalling to the face side and gliding of the spalled ice pieces along the face side. The tool is proceeding from left to right, the back side is upwards in the picture. The white crushed ice at the back side is adjacent to the tool. Interval between the frames is 0.8 ms, or 6.6 mm of blade travel. The dimensions of the rectangles drawn on ice are 100 mm x 50 mm.

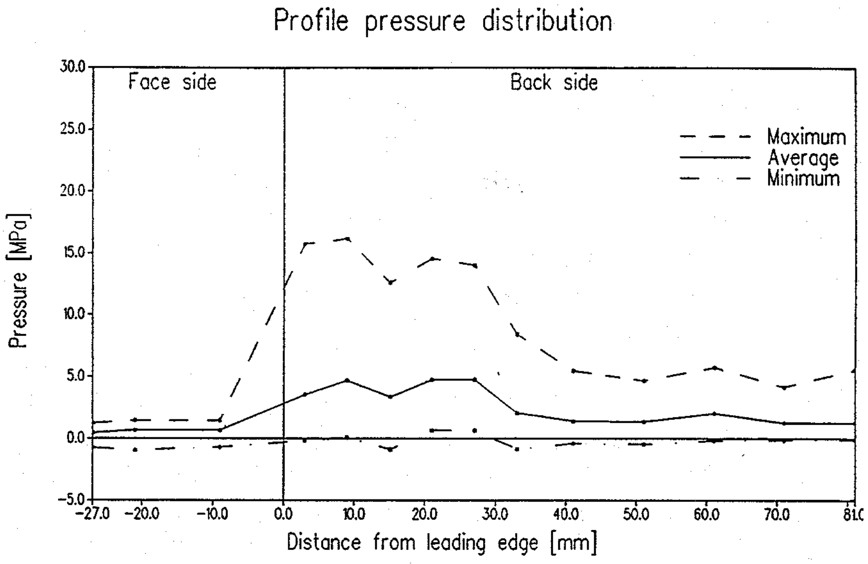

Figure 11. The mean and maximum / minimum envelope of pressure distribution along the tool of all basic tests (angle of attack 7 ° and cut width 50 mm).

2.3.1.2 BACK SIDE

Observations of the cracks on the back side were made from thin section photographs taken from samples of the ice edge that was formed from the pass of the tool. Note that the actual area from which the material has been removed is no more visible in the thin sections.

<u>Thin ice</u>

In the case of thin ice, which is free to fly in the vertical direction, vertical cracks run from about the middle of the ice depth towards the free surfaces (upper level and bottom of the ice sheet) at an angle of some 30 - 45 degrees to the ice edge formed by the tool, see Figure 12. In many test cases a dark horizontal line was visible in the ice after the pass of the tool. It was located some 1/3 of the ice thickness from the upper level of the ice sheet and its thickness was a few millimetres. The line was surrounded by crushed ice. This cracking mechanism is similar to what would be expected by applying the Daley (1991) model to the present geometry, Figure 13. The difference is that the flakes have not been removed as a whole, but some ice has been crushed between the crack and blade surface and mainly remained in place.

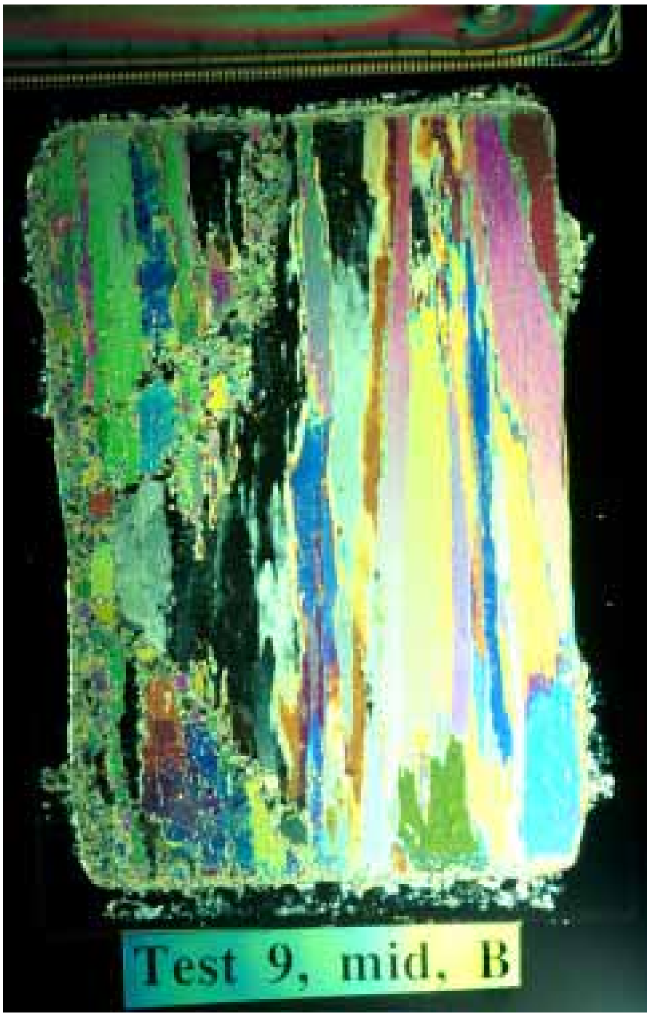

Figure 12. The thin section photograph of a specimen in the vertical direction after test 9 (basic test). The tool has passed the ice specimen at the left side. The contact line is at the mid depth of the ice sheet. Cracks are running towards the top and bottom level of the sheet.

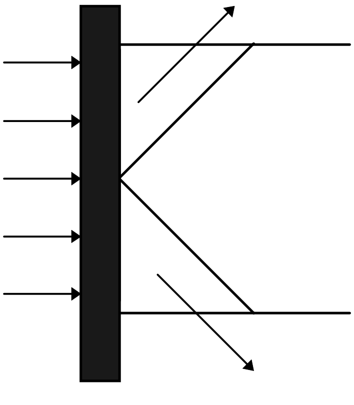

Figure 13. The failure mechanism of the ice, Daley model applied to the present loading geometry.

The pressure measurements gave the following results that are relevant to crack formation. Low pressure and high pressure phases varied cyclically during the time history of a single pressure sensor. The pressure rose to a peak value and then fell to a level varying from close to zero to about 2/3 of the peak value, Figure 14. The high pressure area along the profile is located where the blade has to remove most of the material, Figure 11. The peak pressures can be associated with sudden failure in the surrounding ice. The rate of the pressure increase at the peaks was generally about the same as the rate of decrease. It can be noticed that the nature of the pressure sensor signals closest to the leading edge differed clearly both from the signals of the sensors towards the trailing edge and the leading edge sensors themselves, Figure 14. The peak pressure values, the frequencies and the amplitudes of these “close to leading edge sensors” were all higher. This can be explained as follows. The size of the pressure sensors was 4 mm x 10 mm, with the longer dimension in the vertical direction. In the case of a horizontal high pressure area contact line, the average pressure would be lower than in the case of a vertical contact line. The horizontal contact line was observed to exist where the easiest failure mode forms spalls in the vertical direction. Thus it is natural that the failure mode occurring close to the ice edge that was opened by the leading edge crack was a spall in the horizontal direction, especially because the curvature of the profile here changes a lot. This implies a contact line in the vertical direction and a high pressure along the whole length of the pressure sensor. This mode is also analogous to the extension of the Daley model (1991) with end flaking spalls. This spalling mode is applicable also to the massive ice case. The thin section photographs give no evidence of this process since the ice was removed during the failure process from this area. The resolution of the high speed film does not enable a direct observation of this kind of edge spalling either.

A three dimensional image of the pressure as a function of the location along the blade profile and time during the event shows quite clearly the nature of the process, the cyclic variation of peaks close to the leading edge and the lower pressure further from the leading edge at the areas of tangential contact, Figure 15. A kind of a wave form is visible at the low pressure areas in the same figure. This can be explained to be generated when each sensor proceeds along the circular path governed by the pendulum over the horizontal contact line, where there exists a more or less actual contact with solid ice, causing accordingly a higher pressure.

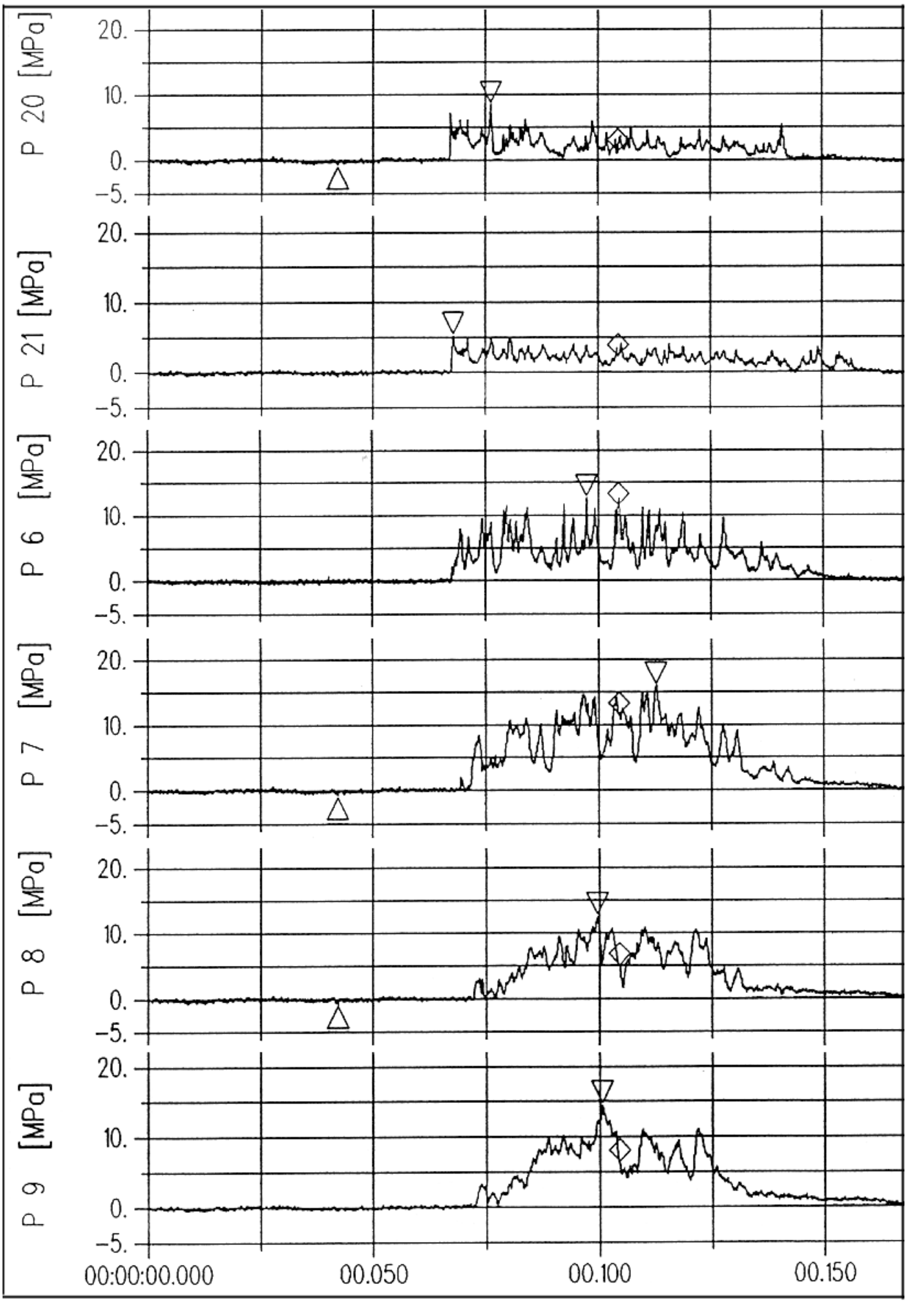

Time [.s]

Figure 14. Pressure time histories of Test No 9 (basic test) showing the cyclic nature of the pressure. Time histories of sensors No 20 and 21 at the leading edge and 6,7,8 and 9 at the back side (No 6 closest to the leading edge) are shown.

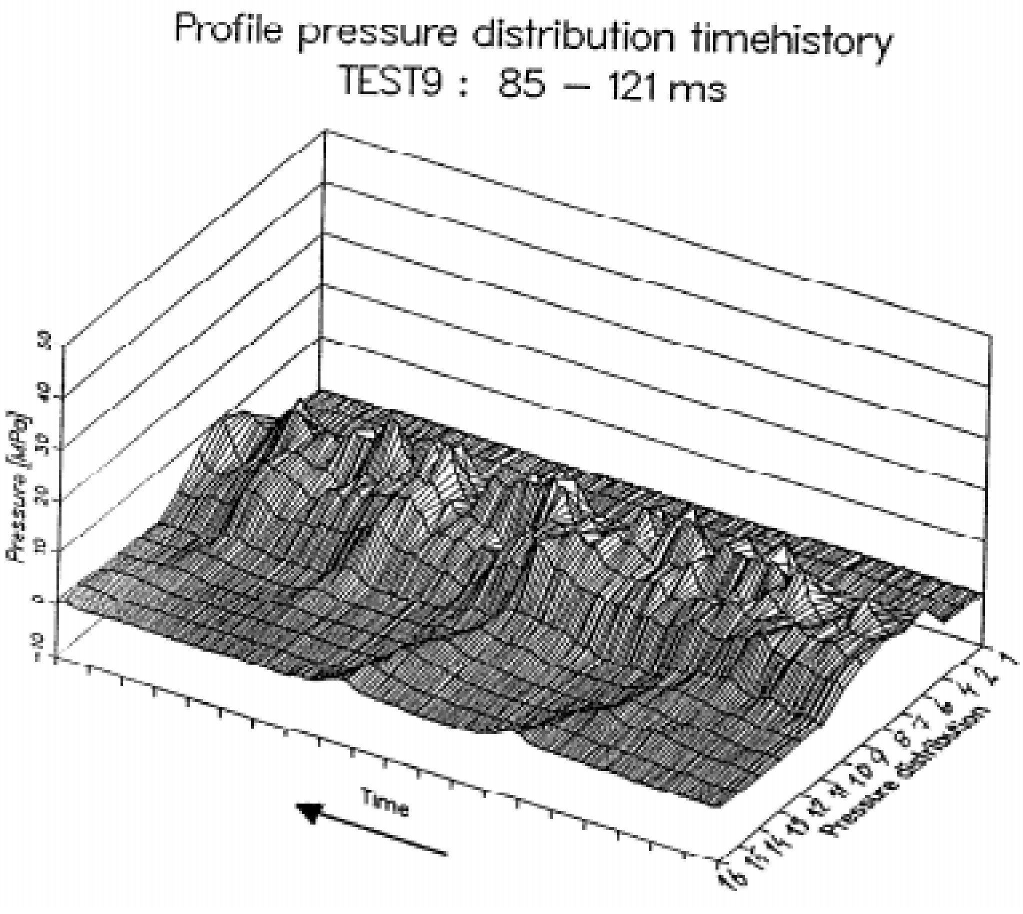

Figure 15. A pressure distribution / time history image of test No 9 (basic test).

Massive ice

Some cracks running very deep within the ice sheet could be observed, but the thin section photographs, Figure 16, do not show any cracks close to the blade surface. Cracks in the vertical direction did not generally appear since a free ice edge could not be found there. In other words there does not exist observed evidence of cracking as the mechanism of failure in any direction at the back side. However, if some macrocracking occurs as a part of the failure mechanism, analogous to the mechanism in the case of thin ice, it must take place in the horizontal direction within the area that is destroyed during the progress of the tool. The time histories of pressure in low pressure areas do not show any peaks, thus supporting the fact that a horizontal contact line and vertical spalling do not exist in contact with massive ice.

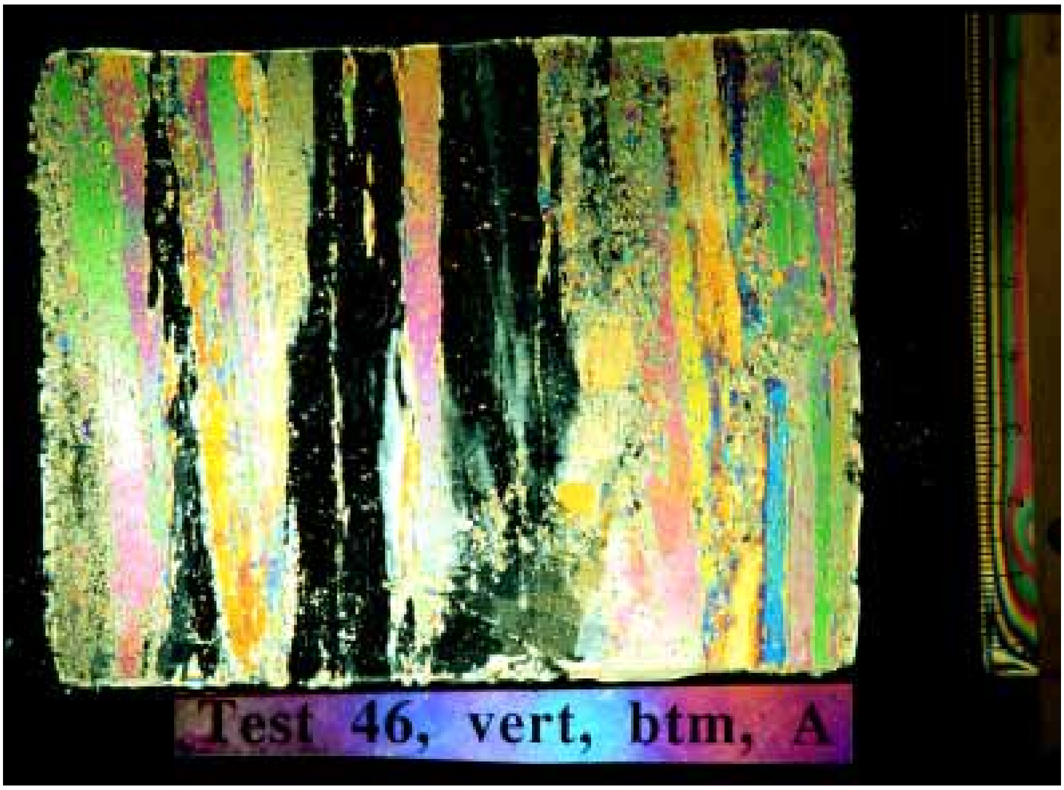

Figure 16. The thin section photograph of a specimen in the vertical direction after test 46, massive ice. The tool has passed the ice specimen at the left side. A very even layer of crushed ice is visible within the first columnar grain adjacent to the tool. No cracks can be observed.

2.3.2 Crushing and removal of crushed ice

When the tool proceeded, ice material had to be removed from its path. At the back side ice was not free to fly away as cracked flakes. Instead the ice was crushed and then extruded.

<u>Thin ice</u>
The crushing phenomenon was cyclic, see Figure 17 a, a series of high speed film frames of the test No 35, 100 mm cut width test. Figure 17 b, a still photograph of the same test, shows the crushing within crack borders. It must be noted, of course that these figures show the phenomena only at the surface of the ice sheet, not within the ice. In case of zero cut width the extrusion was observed to take place horizontally ahead of the leading edge from a pocket of crushed ice and also cyclically, see Figure 18. This result is applicable also to the massive ice case. At a certain distance from the leading edge at the back side the extrusion seemed to take place vertically and without any clear cyclic nature.

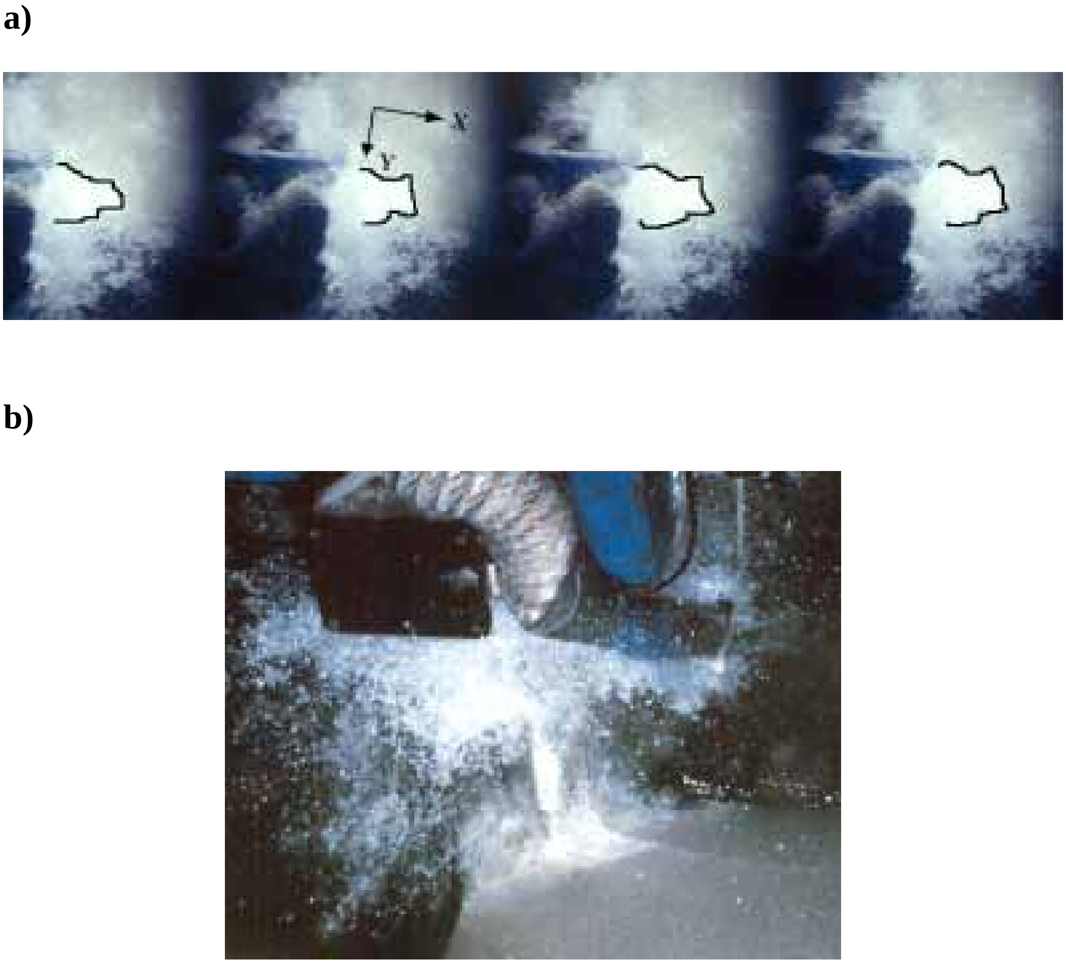

Figure 17. a) The growth of the crushed area (the bright spot in the middle of each frame) ahead of the tool, 0.8 ms time difference between each frame. The crushed area grows gradually. b) Still photograph showing the crushing within the area bordered by cracks. The tool is proceeding towards the camera, face side at left and back side at right (a crack running deep within the ice sheet is not typical in the tests).

Figure 18. The horizontal cyclic extrusion of the crushed ice, 0 mm cut width.

The observations of the ice after impact by the tool showed a white compacted mass with a thickness varying from a few millimetres to a few centimetres, often in a triangular shape on both sides of the horizontal contact line. The thin section photographs, Figure 12 show that the whole layer was not always totally crushed but a triangular flake was formed between the pass of the blade and the crack. In some cases the crushed ice layer was of even thickness within an ice crystal.

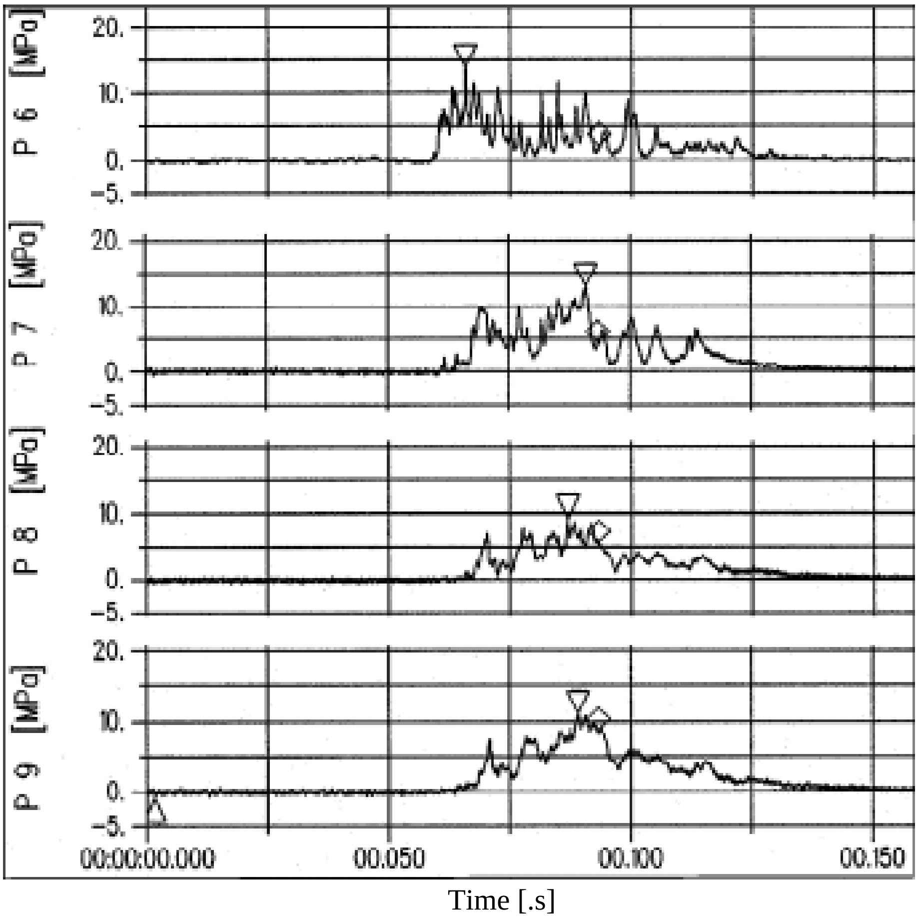

Figure 19. Pressure time histories of sensors 6, 7, 8, and 9 of test No 46, confined ice.

<u>Massive ice</u>

The crushed ice formed a very fine and even one-grain-wide layer, Figure 16. At the upper level of the ice sheet the thickness increased to fill the full clearance between the path of the tool and the confinement plate, some 20 mm. The nature of the pressure time histories, of the sensors close to the leading edge, Figure 19, did not differ from those of the thin ice test cases, revealing that the failure mechanism did not differ from the thin ice case at the path of the sensor belt close to the upper level of the ice sheet. The pressure signals of the sensors closer to the tangential part of the contact, however, as described in section 2.3.1 miss the peaks formed by the pass of the horizontal contact line.

2.3.3 The global load of the tool vs. integrated pressure values

The measured global transversal and longitudinal forces are compared to an integrated value from the pressure distribution during the established test phase. The same distribution is used over the whole vertical range of the tool. As an example the global force time histories are shown in Figure 20 together with some pressure time histories for test 9 (basic test).

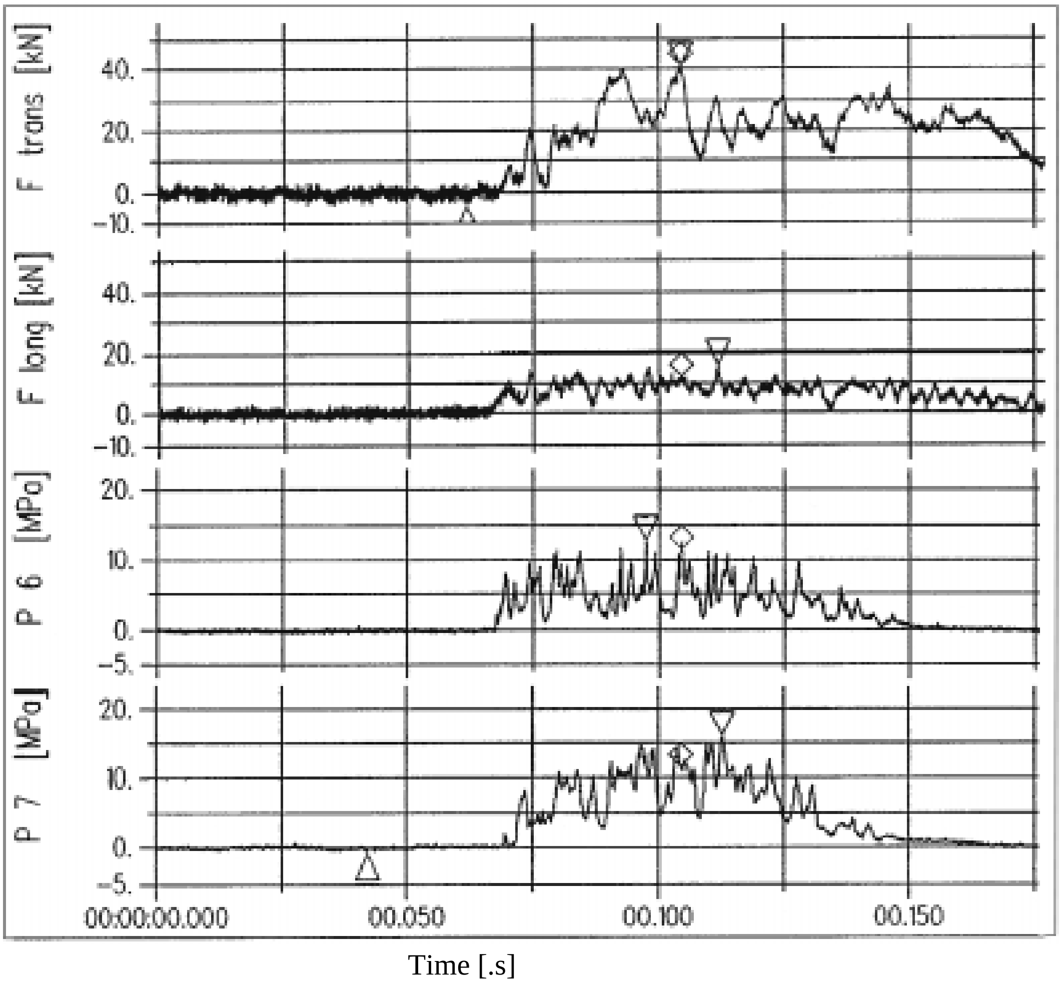

Figure 20. Global transverse and longitudinal loads together with pressure signals from sensors 6 and 7 for test 9 (basic test).

Thin ice

Both the transverse and longitudinal measured global value vs. the integrated value vary from 50 to 60 % for normal angles of attack. An analysis of the pressure as a function of the distance of the pressure sensor to the upper level of the ice sheet gave for 9 test cases the results shown in Figure 21. The vertical distribution is not genuine in the sense that it describes the situation simultaneously in the vertical direction but rather during a certain sensor's progression in the vertical direction. It does show, however, that the extrusion of crushed ice within the flake produces a resistance. If the flakes flew freely in the vertical direction the pressure would concentrate entirely on the region of the contact line.

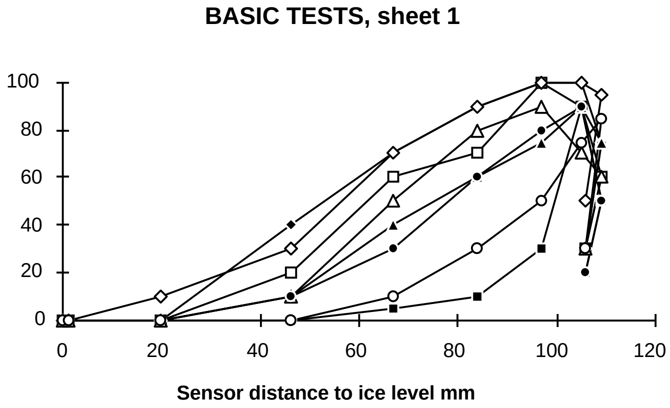

Figure 21. The relative pressure dependence of the sensor location on the top level of the ice sheet in the path of the profile. Pressures have been calculated from sensor No 8 (in some cases sensor No 9) values.

Massive ice

The comparison of measured global forces vs. integrated forces from pressure signals gives in this case on average 89% in the transverse and 114% in the longitudinal direction. However, in these tests the pressure signals drop as functions of the vertical distance towards the upper level of the ice sheet in a manner similar to the thin ice cases. The nature of the pressure time histories is also similar as pointed out earlier. This means that most of the pressure is concentrated at the lower regions of the tool. It is possible to combine the information of the global load, the moment lever of the global load in the vertical direction and the vertical load distribution at the upper range of the ice sheet, based on the pressure measurements. This will result in a vertical load distribution roughly like Figure 22.

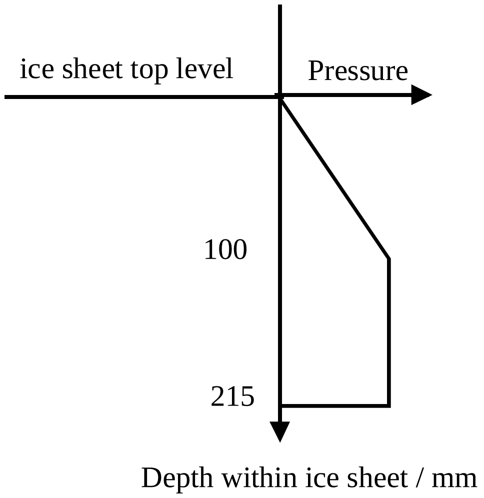

Figure 22. The schematic vertical pressure distribution in the massive ice test cases.

The load increases linearly from the upper level of the ice sheet to some value that remains essentially constant further along the tool. This means that at these areas of deeper penetration the process is two-dimensional along the profile direction. The load level in these areas is for the two test cases on average 1.64 times (test No 45) and 1.19 times (test No 46) higher than the load that is calculated from the measured average pressure value. In test No 45 there is probably some kind of local inhomogeneity in the ice structure and strength since the global load continues to grow up to a point at which the vertical contact length is 73 % compared to the bottom dead centre. Information of the load distribution in the profile direction in these deeper ranges can be obtained from the position of the resultant global force. It appears that the resultant force acts in the profile direction 20 mm from the leading edge versus 30 mm on average for the thin ice test cases. This also reveals that the mechanism was different in the confined case, in which the extrusion and possible cracking was forced to take place two-dimensionally in the profile direction. An estimate of the mean pressure values at the high pressure area behind the leading edge can be made taking into account the result of the shift of the resultant force in the profile direction and comparing the vertical pressure distribution of the tool to the measured ones. This will result in approximately 1.7 - 1.8 times higher mean pressure values as compared to the cold ice test cases. A comparison to the cold ice cases rather than to the warm ice cases is justified because the measured compressive ice strength against the grain direction was actually higher in the massive ice test cases than in the cold ice tests.

2.3.4 Effect of different parameters

Angle of attack
Varying the angle of attack from 4° to 12° did not cause any major change in the nature of pressure signals. The shorter contact length in the 12° case could of course be found. In the case of a 25° angle of attack the face side pressure was concentrated close to the leading edge. No contact at the back side existed.

Velocity
The tests were performed with a quite high impact speed. In principle the process should be the same beyond the transition to the brittle regime. The failure mechanism in the slower tests differed clearly from the higher speed tests. Instead of crushing and extruding the crushed ice, the ice was cracked into relatively big pieces. The measured pressure levels did not, on the other hand, differ from the faster tests. The pressure distribution time history showed somewhat more violent behaviour compared to the faster tests. The mode change to cracking with slower indentation speeds instead of crushing and cracking is in principle against the Saeki and Ozaki (1980) scenario as described in section 1.3.1.

Temperature
The pressures are clearly higher in the low temperature tests than in the tests with higher temperatures. The frequency and amplitude of the peaks are high. Table 3. gives the pressure values along with the average uniaxial compressive strength values, as measured after tests from ice samples adjacent to the test location (compressive test strain rate 2 x 10^{-4} s^{-1}). The average pressure value is defined from the sensors 6, 7, 8 and 9 close to the leading edge, the location giving in general higher pressure values. It is evident that the maximum pressure and average pressure do not follow the same ratio.

Table 3. Ice strengths vs. blade pressures.

	T_{ice}(average) °C	p_{av} MPa	p_{max} MPa	$\sigma_{vert.}$ MPa	$\sigma_{horiz.}$ MPa
Basic tests	-2.0	5	8.1	2	1
Cold tests	-4.5	6	13.8	4	2
Ratio	-4.5/-2	1.20	1.70	2	2

Cut width
A clear pressure dependence on the cut width was found in the tests both for the average and peak leading edge pressures, Figure 23. The global load required for the spall to open at the face side was concentrated in the cases of 0 - 100 mm cut width at the sharp leading edge of the profile where the 4 mm wide pressure sensor is located. Thus most of the load was experienced

in the pressure sensor area and was registered as a dependence of pressure. The leading edge geometry at the face side for the 220 mm ice thickness test case (-25° angle of attack), was different from the rest of the test cases. A less concentrated contact was experienced.

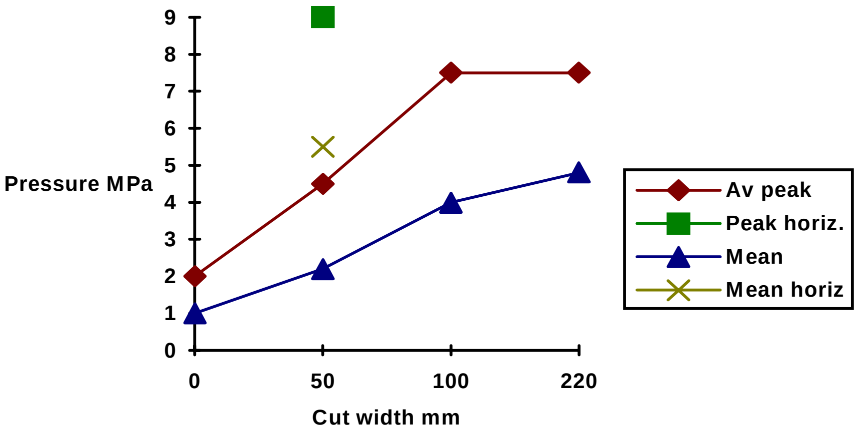

Figure 23. The average leading edge peak and mean pressure in the tests as a function of cut width.

Veitch (1995) has found in the analysis of his tests that the average and maximum pressure depend on the apparent contact area. This dependence is widely accepted from other ice indentor applications. However, the pressure becomes rather insensitive for an apparent contact area greater than 1500 mm^2. Thus Veitch uses a constant pressure in his model at the cinematic leading edge. This pressure is the average maximum pressure in the tests (12 MPa) or twice the reference strength of 6 MPa, representing the measured average uniaxial compressive strength.

<u>Grain direction</u>

The tool impacted against horizontally arranged grains in two tests. The peak pressure was located at the leading edge and at the next sensor on the back side. The leading edge pressure values were higher than in the vertical grain cases, Figure 23. The pressure values of other sensors were very low. The peak frequency was high but the amplitude low. The leading edge had to cut across the grains. The tensile stress at the leading edge acted across the grains, whereas in the vertical grain cases, the tensile stress acted along grain boundaries. The thin sections reveal a somewhat different failure mode compared to the vertical grain case. The horizontal contact line is not very clear. A few cracks run in the vertical direction, some at a depth of a few centimetres, some touching the contact zone. The pressure time history of the sensor next to the leading edge and the thin section photographs, Figure 24 supports an assumption of almost individual buckling and crushing failure of each grain. The rest of the profile geometry just pushes the failed grains somewhat further aside.

Wet/Dry tests

No difference was found in the quality or quantity of pressure signals in the wet versus the dry tests. This is to be expected since in wet tests (and in actual propeller ice contact) the contact within the ice sheet takes place in dry conditions, i.e. the slot is filled with water only after the impact.

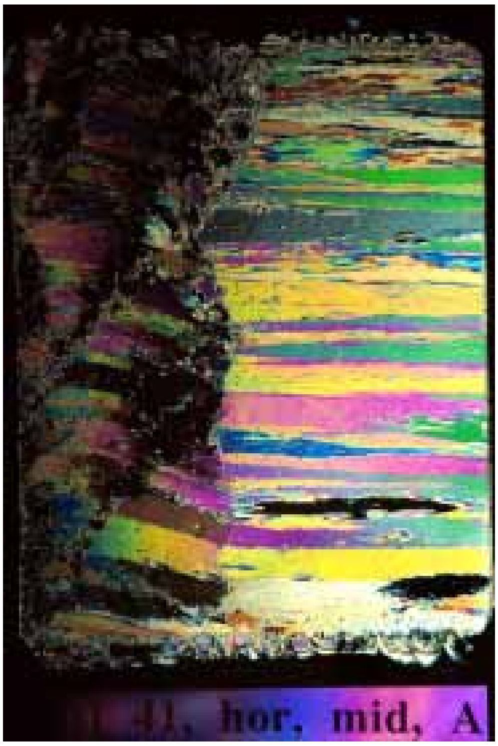

Figure 24. Thin section of a sample after horizontal grain test case. The section is taken in the horizontal direction, and the tool has proceeded from top to bottom in the figure.

2.3.5 Discussion and conclusions from the test results

Cracks were generated at the leading edge and ice spalled at the face side towards the free ice edge that represents the groove formed by the previous blade impact. Actual contact hardly took place and only marginal pressure was generated at the face side. The transverse resultant force bent the blade towards the face side. Extreme angles of attack where there was no contact at the back side changed the transverse resultant and bent the blade towards the back side.

The leading edge pressure was directly proportional to the cut width at the face side, within the range of cut widths tested. This is considered to be based on the growth of uniaxial compressive strength with the growth of confinement.

In the case of thin ice there was a cyclic variation between high and low pressure at the back side. A horizontal contact line was formed at roughly the mid-thickness of the ice and triangular shaped flakes were formed. The flakes did not fly loose but were partially or totally crushed. The high pressure readings are considered to be associated with the pass of the sensor of this contact line whereas the low pressure readings are associated with contact of crushed ice. The pressure decreased gradually along the path of the pressure sensors from mid-ice depth to the upper surface of the ice. This means that the vertical extrusion of crushed ice within the flake formed a pressure distribution. A pressure distribution is considered to exist also in the case of horizontal extrusion.

In the thin ice case the highest pressures took place immediately behind the leading edge. The geometry of the profile just behind the leading edge actually forms a corner where the velocity in the normal direction drops steeply from the leading edge values. The nature of the pressure readings here was different from the others in that the amplitude and frequency of the peaks was higher. This is interpreted as meaning that a spall formed in the horizontal direction from this area opening towards the ice edge ahead of the leading edge. The high speed film resolution was not clear enough to show the crack formation of this spall but did show a sudden cyclic phenomena ahead of the leading edge. The pressure readings at the leading edge sensors were relatively similar regardless of their vertical position meaning that the phenomena were two-dimensional in the horizontal plane. This kind of horizontal spall formation is naturally valid also in the massive ice contact case.

In the case of massive ice cracks in the vertical direction were found only close to the upper level of the ice sheet. The nature of the pressure measurement results in this area was also similar to the case of thin ice. A thin, about one grain wide, crushed layer was left between the blade and the solid ice deeper within the ice sheet. Thus if the failure mechanism requires spalling before crushing the spalls have to be small and the spalling has to take place in the horizontal direction. The increased confinement in the massive ice case may change the mechanism towards smaller spall dimensions compared to the thin ice case. A large confinement may also hinder the formation of cracks and cause local crushing. A natural route for the crack is along the grain boundaries. The test case with a 7 ^{o} angle of attack left the width of some 2 to 4 grains to be removed.

When the leading edge was pre-positioned into the ice edge line, i.e. the cut width was zero, a cyclic extrusion of crushed ice was observed ahead of the leading edge in the horizontal direction towards the open space. This cyclic extrusion is considered to also exist in the case where some cut width exists and the open space is formed by the spalling at the face side. Further it is natural that this type of extrusion is valid also in the massive ice case where the extrusion in the vertical direction is not possible.

The crushed ice produced by the horizontal extrusion bursts was clearly in granular pulverised form. However, the crushed ice that was left between the tool and the solid ice, both in thin and massive ice tests, was consolidated into a sintered mass. Thus any extrusion between the tool and the solid ice towards the trailing edge in the horizontal direction or towards the free levels of the ice sheet in the vertical direction must take place in sintered mass form. According to various extrusion models the pressure is at its highest where the flow of extruded material starts and is lower towards the outlets of the channel. It is thus unlikely that the crushed ice would start its flow in granular form and later, when the pressure is released, be sintered.

Based on the global loads and their directions it was concluded that the pressure distribution in the massive ice case was fairly even in the vertical direction for some distance from the upper level of the ice sheet. This means that the failure phenomena are two-dimensional in the horizontal plane. A vertical extrusion of crushed ice is not possible because the pressure would grow in the vertical direction towards the lower end of the tool. The location of the concentrated pressure in the horizontal direction moves closer by one third of the distance to the leading edge in the massive ice compared to the thin ice case. This supports a different failure mechanism in the massive ice case compared to the thin ice. The following interpretation is made. In the case of thin ice the pressure that is associated with the horizontal contact line is rather even in the whole range of that part of the profile length where the majority of the ice removal has to take place. In the case of massive ice the formation of small horizontal spalls is concentrated closer to the leading edge due to the preferred crack orientation along grain boundaries. If some local crushing took place instead of crack formation due to a large amount of confinement it would also happen in the same area.

The temperature decrease at the sensor zone from some -2 ^{o}C to some -4.5 ^{o}C roughly doubled the uniaxial compressive strength, and increased the transversal global force some 20 %, the average pressure readings some 20 % and the peak pressure some 70 %. This is considered to mean that a majority of the effective load is generated from the extrusion mechanism between the peak loads and a minority is associated with the peak loads themselves and accordingly depending on the strength of the ice. This result is from the thin ice test case and the greater confinement in the massive ice case may further decrease the importance of the actual strength of the parent material.

In the case of horizontal grain orientation some cracking occurs within the ice sheet at the back side. The grains are bent inside the spalls formed by these cracks and crushed at both ends, the contact surface and the end adjacent to the macrocrack.

The original test arrangement was planned for the thin ice cases and accordingly the major part of the tests performed were made for thin ice. Only two individual tests were performed for the massive ice case when it became evident that the failure mode in thin ice did not represent realistically the propeller contact with massive ice. Some of the conclusions made for the massive ice contact are therefore indirect. A repeated test programme planned especially for massive ice contact would therefore throw more light on the associated phenomena. A repeated programme was, however, beyond the available resources of this work.

3 BLADE-ICE CONTACT PROCESS MODEL

The process of a propeller blade in contact with massive ice is modelled in the following based on the test results presented above. The basic assumption is a two-dimensional behaviour within each section. The total contact load is found by integrating the load of each individual section along the blade radius. The two-dimensionality assumption is neither valid at the ice block edge close to the hub, nor at the tip sections of the blade. A correction taking this into account is proposed. As stated earlier the model is based on a first quadrant contact, with the leading edge in contact with ice. The angle of attack is limited to values greater than or equal to zero.

3.1 LEADING EDGE AND FACE SIDE

Tensile stress is generated within the solid ice ahead of the leading edge, transversally to the direction in which the blade is proceeding. A tensile crack opens towards the free ice edge. A flake is formed, Figure 25. The face side of the blade experiences only marginal loads from the limited contact with intact ice at the leading edge. The leading edge load is governed by the load that is needed to form the crack. This is dependent on the grain orientation ahead of the leading edge and the cut width as far as it affects the confinement at the leading edge. The mean pressure at the leading edge depends on both the load needed to form the crack and the pressure created when extruded ice from the back side hits cracked ice flakes.

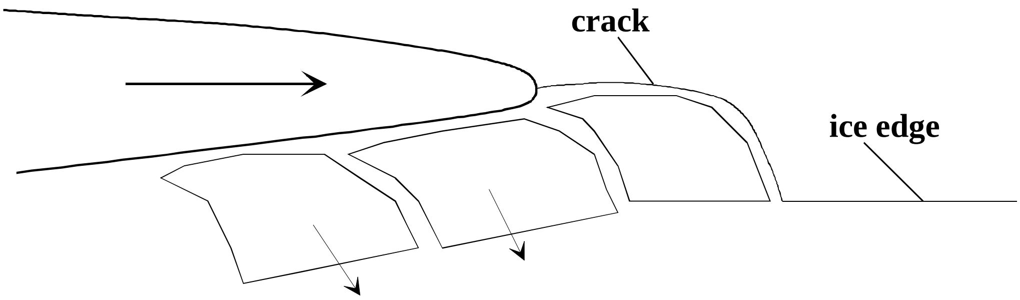

Figure 25. Flaking towards open ice edge at the face side.

3.2 BACK SIDE

The model is developed for the case where the grain orientation of the ice is coincides with the propeller radius. A majority of ice floes that are forced below the water level by a ship hull will meet the propeller in this orientation. A more important justification for this approach is that, based on the test results, this orientation will give more conservative loads against the blade back side.

As mentioned it was not possible to make any direct observations of cracking and subsequent crushing in the present massive profile pressure distribution tests. The different confinement conditions in the thin and massive ice cases can affect the failure mode. The basic assumption for the massive ice case is that when confinement due to extrusion of crushed ice is moderate an analogous failure process to the thin ice case can be expected. The model is thus based on a series of spalls in the profile direction, crushing within the spalls and the extrusion process. It is accordingly further assumed that the geometry of the channel of crushed ice between the blade and solid ice is governed by the geometry of the macrocracks. If considerable confinement takes place because the extrusion is obstructed somewhere due to the geometry of the crushed ice channel the peak pressure will grow high and local crushing will take place. The ice outside the channel is defined as solid. In reality this "solid" ice is somewhat cracked and the border between the crushed ice and solid ice is not quite sharp.

A crack is formed in the profile direction close to the leading edge towards the open ice edge that the leading edge tensile crack has opened. Based on the test observations and FE stress analysis with measured pressure distributions (assuming Mohr-Coulomb macroscopic failure criterion, section 4.2) the origin of the crack is where most of the leading edge curvature has been smoothed. The ice is crushed within this small flake between the crack and the leading edge of the blade. A curved crack running towards the free ice edge formed by the previous crack is formed at the next local peak pressure location along the profile. The crack geometry follows most probably the grain boundaries. The ice is crushed within the spall either partially or fully. The process goes on so that a channel of crushed ice will form between the blade and solid ice. The crushed ice is extruded through this channel to the open space either profilewise towards the leading edge or tangential point of the contact, or radially to the free ice edge. The pressure distribution follows the laws of extrusion mechanisms. An instantaneous "watershed" for the extrusion process is formed in the vicinity of each location where the channel starts to narrow before a new crack is born. The loose crushed ice mass is compacted almost into a solid again when the pressure rises high within the crushed ice, due to local narrowing of the channel. When the blade proceeds a new crack is originated from this stress concentration. If the extrusion is obstructed due to a narrow channel point somewhere other than the actual “watershed” area a confinement will be built up and the crack formation will be hindered. The pressure will grow until local crushing at the peak pressure area takes place. The local crushing will continue until the confinement is released due to opening of the crushed ice channel at the obstruction point.

The process, presented in Figure 26, can be described as follows:

- crack formation in solid ice
- crushing of ice within the spall. Every spall that is crushed is a link of a chain forming the geometry of a channel of crushed ice
- extrusion of crushed ice in the channel, the pressure distribution depending on the channel geometry
- new crack formation at the location of maximum pressure, or local crushing in the case of considerable confinement, that might be followed by crack formation when the confinement is released.

The effective load against the blade is taken as the mean of the instantaneous pressure distributions over a period of time - not the envelope of the instantaneous peaks since the peaks are effective only for a short time just before the local failure of solid ice. Furthermore the process goes on non-simultaneously within each section.

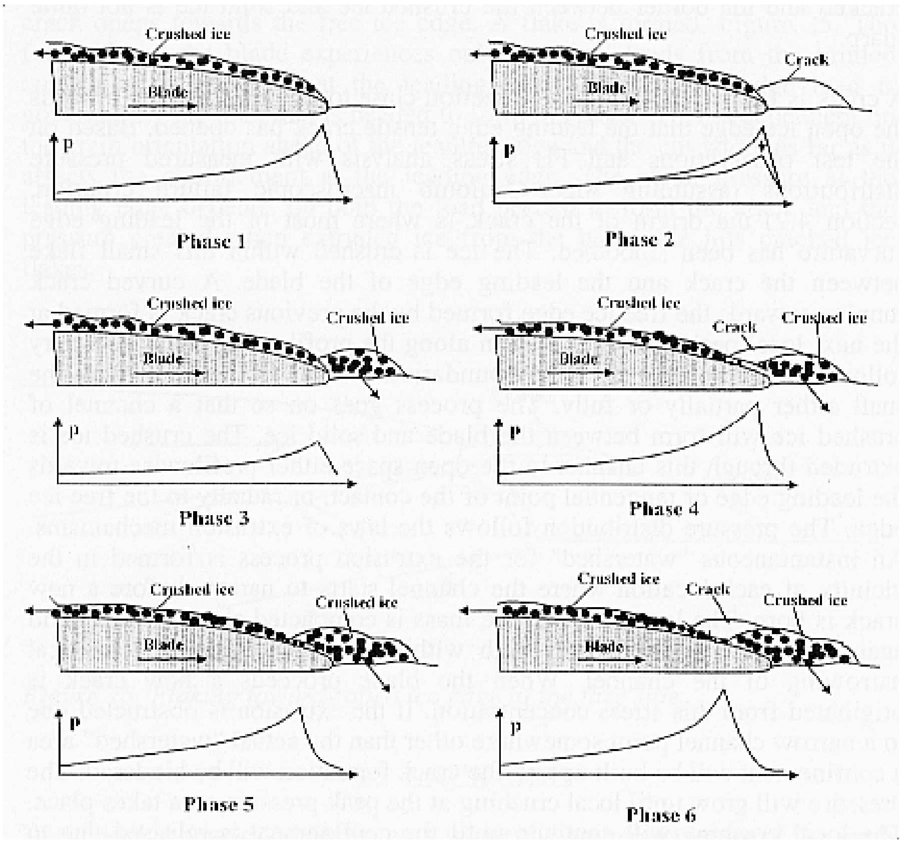

Figure 26. The schematic cracking and extrusion process at the back side of the blade. Most of the proceeding of the blade takes place between the phases 3 to 4 and 5 to 6.

The model is based, as described above, on spalling of small spalls and subsequent crushing and extrusion. Tuhkuri´s (1996) model could also in principle be applied. In the theoretical case that the process would start from full contact along the profile (no crushed ice between the profile and solid ice) the cascade of flakes would start from the leading edge crack. The cascade would run to the contact line that would be formed at a location where there is sufficient depth of crushed ice to allow the blade to proceed. In a case of a small angle of attack the process would probably start from the leading edge again before the process further along the profile is finished. Once a channel of crushed ice forms between the blade and solid ice the process would change nature. The location of the closest contact between the blade and solid ice (either genuine contact or compacted crushed ice between the blade and solid ice) would be the starting point of a new macrocrack that would grow and form the flake. The process to form new narrow flakes would continue from here along the profile towards the trailing edge while the profile is proceeding. The flakes would be crushed and the crushed ice extruded from the channel as described above. Local points of contacts that might be formed while the blade proceeds and the channel of crushed ice is narrowing, would be starting points of new flaking processes regardless of the fact that the flaking would still be going on further towards the trailing edge of the profile.

3.3 THREE-DIMENSIONALITY ADDITIONS TO THE BASIC MODEL

3.3.1 Milling of thin ice and free ice edges

In the case of milling thin ice, Figure 27 a, the back side failure mechanism changes. The first crack in the direction of the profile in the vicinity of the leading edge would take place as described above. According to test observations the failure of ice at the rest of the back side would happen by radial cracks and crushing within these flakes. The removal of ice would be by radial extrusion of crushed ice. Radial cracking and extrusion would occur also analogously in the case of milling massive ice at sections that are close to free ice edges, in practice close to the propeller hub, Figure 27 b.

3.3.2 The blade tip area

The model assumes two-dimensional behaviour, and assumes thus a uniform crack geometry towards the free ice edge at the face side along the whole leading edge. In practice a series of spalls is formed along the leading edge. Close to the tip area the velocity pattern and geometry changes. There is no compression in the solid ice in the rotational direction at the tip. Consequently the formation of a tensile crack, as assumed in the leading edge model, is not possible. Instead, the tip radius sweeps the ice into the previous groove by spalling the ice in a radial direction towards the propeller hub and removing the crushed ice within these spalls. This causes a load at the face side of the blade in cases of positive angles of attack, see Figure 28. The radial blade tip spalling can be considered to be a special case of the radial spalling discussed in the previous section 3.3.1.

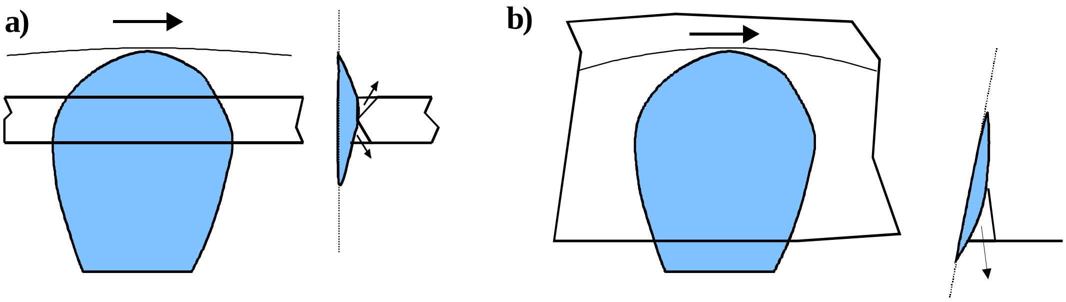

Figure 27. Radial cracking. a) Milling thin ice, b) Milling massive ice close to the hub.

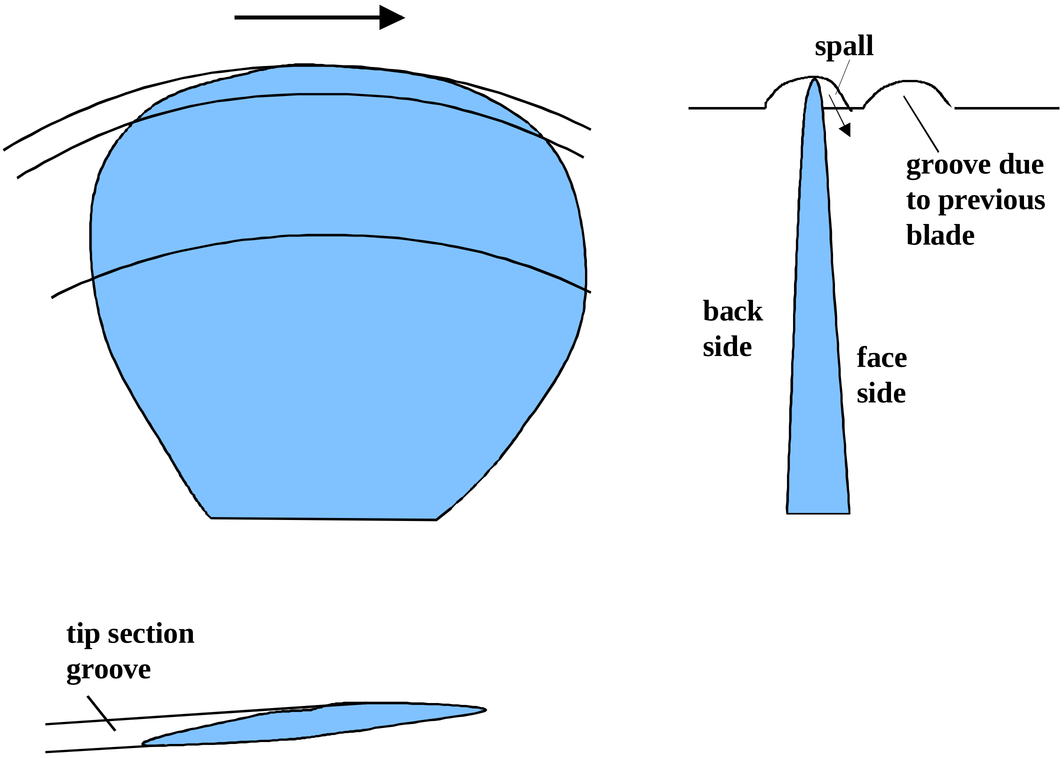

Figure 28. Face side cracking of tip radius area.

4 FAILURE OF SOLID ICE

4.1 GENERAL

The instantaneous maximum pressure against the blade is assumed to depend on the stress needed to create the macrocracks as stated above. Therefore, defining the critical stress state and the geometry of the spalls give the basis for the quantitative data in the model.

Some macroscopic models have been published explaining the flaking failure of ice against an indentor. Daley (1991) has developed a failure process model for ice edge contact. He uses a simple failure criterion based on Hallam´s (1986) model and rearranged into Mohr-Coulomb form. The shear failure is assumed to take place along a straight line by flaking. Kujala (1994 a, b) has applied the slip surface concept that is used in soil mechanics. A macroscopic failure is assumed to take place when the total load is enough for a slip surface to develop from the contact zone to the free ice edge. The material is assumed to be in a failure state along the whole slip surface, and outside the surface it is assumed to be in an elastic state. Using the Mohr-Coulomb criterion and a radially distributed stress field in wedge shaped ice, Kujala ends up with curved slip surfaces along logarithmic spirals. Daley´s straight shearlines are a simple application of slip surfaces. Macrocracking in the blade/ice contact process can also be studied by fracture mechanics as in Tuhkuri´s (1996) model as described in section 1.3.1.

The macroscopic slip surface approach is used in this work. The path of the crack is governed by the stress state. The total failure load is the integral of the loads needed to cause a failure along individual slip surface elements.

The Mohr-Coulomb criterion, used in Daley´s (1991) and Kujala´s (1994 a, 1994 b) macroscopic models is applied in the present analysis as the ice failure criterion. The Mohr-Coulomb criterion states that the critical shear stress τ_C is

$$\tau_c = c + p \tan \phi \tag{1}$$

where c is the cohesion, ϕ the internal friction angle and p the normal pressure. Paul (1968) has presented the failure criterion in principal stress form:

$$\sigma_1 = -S_c + \frac{S_c}{S_t^{'}} \sigma_3 \tag{2}$$

where σ_1 is the major principal stress and σ_3 is the minor principal stress. S_C, the uniaxial compressive strength and the "nominal" uniaxial tensile strength S_t' are

$$S_c = \frac{2c\cos\phi}{1-\sin\phi} \tag{3}$$

$$\frac{S_c}{S_t^{'}} = \frac{1+\sin\phi}{1-\sin\phi} \tag{4}$$

The trajectory of the macrocrack can be found by defining the failure plane direction at each material point. The direction of the principal stresses must for this purpose be calculated at each material point. According to the definitions of the Mohr-Coulomb criterion, the direction ψ of the fractured plane against the load - the major principal stress - direction is

$$\psi = \pi / 4 - \phi / 2 \tag{5}$$

where ϕ is the internal friction angle.

If the principal stress direction is known exactly in some special loading case the path of the crack can be solved analytically. For a parallel stress distribution Equation 5 gives directly the crack track. Kujala´s (1994 a, b) model can be applied for the radial distribution. In case of a complicated loading geometry the calculation of the principal stresses and their direction at each material point is a typical FE-method task. The process of slip surface formation is illustrated in Figure 26. The cracks that are presented in the figure are interpreted as slip surfaces from here onwards.

4.2 THE SPALLING SEQUENCE AND GEOMETRY OF SOLID ICE

The Mohr-Coulomb model assumes a constant angle between the failure surface and the direction of the principal stress according to Equation 5. Spalling of solid ice thus creates in general curved surfaces since the loading geometry of the solid blade does not usually result in a stress distribution of parallel principal stress directions. The actual grain size will affect the slip surface geometry - it will most likely take place along grain boundaries.

In the analysis of this work the curved ice surfaces of solid ice are simplified as straight wedges, Figure 29. This simplification does not affect the general appearance of the principal stress directions or the magnitude of critical loads. The small wedge forming the actual wedge tip in Figure 29 is called a secondary wedge in the text from here onwards.

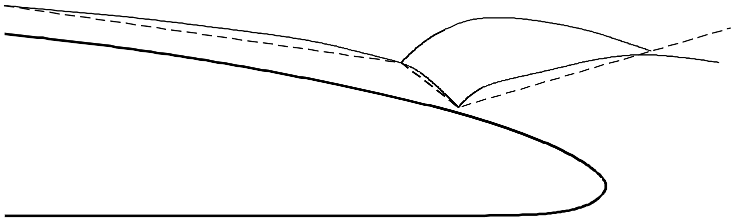

Figure 29. Ice wedge geometry. Curved lines are created by spalling. Straight lines (dashed lines) are used in the calculations.

The rationale of the shape of the pressure distribution is discussed in Section 5 “Crushed ice“ later. The model assumes that the pressure usually rises rather sharply towards the wedge tip. The pressure distribution is somewhat more even towards the trailing edge direction from the tip of the ice wedge and decreases steeply towards the leading edge direction. Typical pressure distributions are shown in Figure 30. The symmetrical case in Figure 30 a develops when the channel of crushed ice towards the leading edge from the wedge contracts. The pressure rises steeply. The unsymmetrical case in Figure 30 b, leading to most slip surfaces, is developed when the channel of crushed ice towards the leading edge from the wedge diverges. The pressure rises very sharply from some even level that is governed by the pressure at the outlet of the channel to the peak value at the wedge. Sometimes a case may also occur where the blade approaches more or less simultaneously two wedges of the solid ice. This will result in a confinement situation where the pressure distribution is fairly even between both wedge tips.

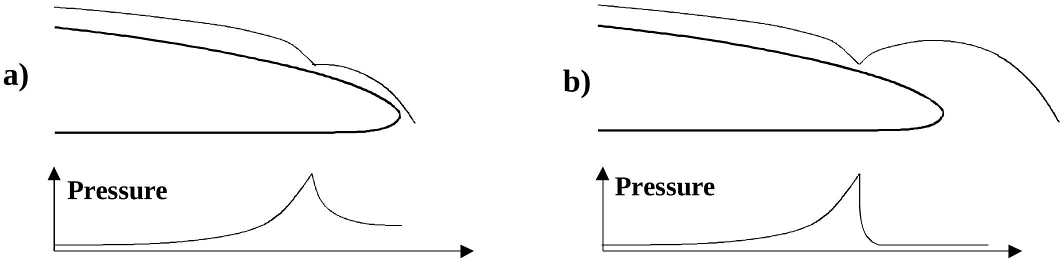

Figure 30. Schematic examples of pressure distributions against the wedge of solid ice; a) contracting channel towards leading edge, b) diverging channel towards leading edge.

4.3 FAILURE LOADS

Failure loads for typical pressure distribution / solid ice wedge geometry combinations are developed. An accurate solution for each case would require a FE-calculation to define the principal stress direction and magnitude combination in each material point. It is not considered viable since the Mohr-Coulomb criterion is just one model describing the failure process and the exact data of numerical values of the parameters can certainly be argued.

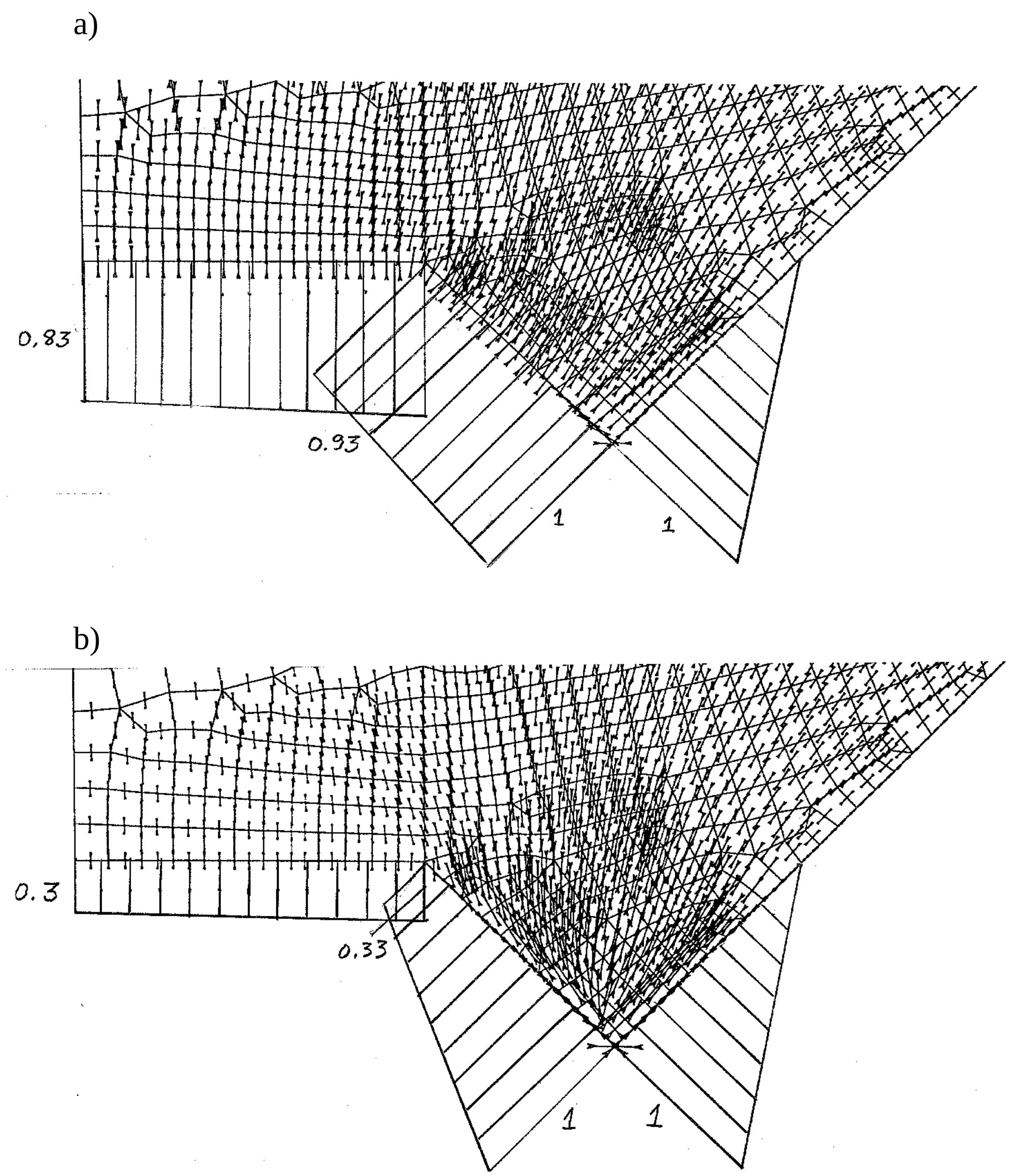

Figure 31. Minor principal stress directions and the relative load distribution; a) unsymmetrical loading, b) symmetrical loading.

Therefore the case is illustrated with two typical examples, Figure 31, based on the pressure distributions discussed in section 4.2: a wedge loaded unsymmetrically, mostly from the trailing edge side of the wedge and another wedge loaded more or less symmetrically from both sides of the wedge, either by a peaky or more even load distribution. Analysis performed by FE-calculations also show that the distinction between these two cases is a basic one. Examples of minor principal stress distribution obtained by FE-calculations (performed by the IDEAS program) for these two cases are shown in Figure 31.

4.3.1 Symmetrically loaded wedge

The major principal stress direction trajectories in the case of a symmetrically loaded wedge are more or less radially distributed resembling the tip loaded wedge case of Kujala´s model. This would call for a logarithmic spiral shaped slip line starting from the tip of the wedge. On the other hand, the analysis of the critical failure location according to the Mohr-Coulomb criterion shows the critical location to be at the leading edge side surface of the secondary wedge, where the pressure lowers to zero. This would mean a slip surface running deep into the solid ice. The integrated load required to split the wedge starting from the tip is, however, smaller than the load required to run the slip surface to infinity within the ice. After the splitting of the wedge the load will decrease radically at the leading edge side, the distribution will change to the case where the wedge is unsymmetrically loaded and accordingly the wedge will be torn off (Section 4.3.2).

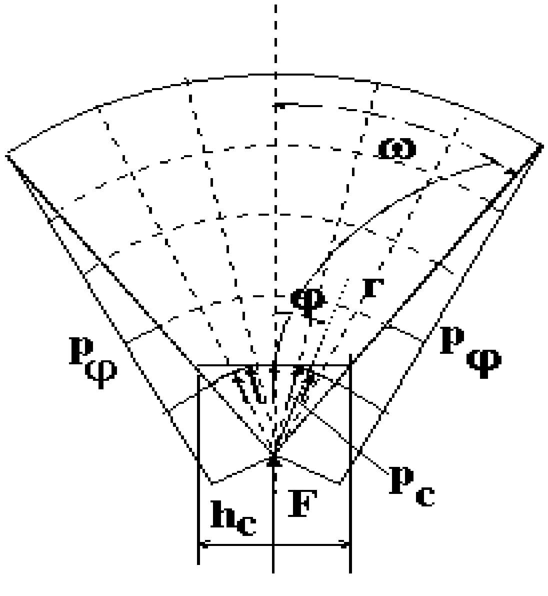

Figure 32. Kujala wedge geometry. F is the total load against the theoretical wedge tip, p_c is the critical pressure against the crushed wedge tip required to cause the slip surface, $p_φ$ the confining pressure and $φ$ and r are the polar coordinates of the slip surface.

A calculation of the load required to split the wedge is performed adding to Kujala´s model the effect of minor principal stresses. The original model was developed for a spherical surface loading an ice wedge. For this geometry the trajectories of principal stresses are radial, the other principal stress normal to this direction being zero. The slip surface will originate from the intersection of the load surface and the symmetry axis, Figure 32. The equation for the slip surface geometry is in polar coordinate form:

$$r = C_1 e^{C_2 \varphi} \tag{6}$$

where C_1 and C_2 are

$$C_1 = \frac{h_C}{2 \tan \omega} \tag{7}$$

$$C_2 = \tan \phi + \sqrt{1 + \tan^2 \phi} \tag{8}$$

where ω is the half angle of the wedge and ϕ is the Mohr-Coulomb internal friction angle. The critical pressure p_c at the loading area is

$$p_C h_C = \frac{2\omega + \sin 2\omega}{2\omega} C_1 S_C \int_0^{\omega} \frac{e^{C_2 \varphi}}{\cos \varphi} d\varphi \tag{9}$$

Equation 9 is modified from the original one presented by Kujala to include the term S_c. If a pressure p_φ along the edges of the wedge exist, there will also exist a minor principal stress σ_φ. If the pressure is even it will increase the required critical pressure at the tip of the wedge so that the term S_C in Equation 9 will be replaced with the term :

$$S_C + \frac{S_C}{S_t^{'}} \sigma_\varphi \tag{10}$$

and the critical pressure is thus

$$p_C h_C = \frac{2\omega + \sin 2\omega}{2\omega} C_1 (S_C + \frac{S_C}{S_t^{'}} \sigma_\varphi) \int_0^{\omega} \frac{e^{C_2 \varphi}}{\cos \varphi} d\varphi \tag{11}$$

In case of an uneven pressure p_φ along the wedge sides the critical pressure is

$$p_C h_C = \frac{2\omega + \sin 2\omega}{2\omega} C_1 S_C (\int_0^{\omega} \frac{e^{C_2 \varphi}}{\cos \varphi} d\varphi + \frac{1}{S_t^{'}} \int_0^{\omega} \frac{p_\varphi(\varphi) e^{C_2 \varphi}}{\cos \varphi} d\varphi) \tag{12}$$

A parametric study of Equation 9 was performed giving the ratio p_c/c as a function of wedge angle ω and having two values for the internal friction angle ϕ as parameter. Some of the numerical values are given in Table 4, section 4.3.4. Kujala has performed the same study (1994 a) and found that the minimum value for p_c/c is reached using for C_2 the equation

$$C_2 = \tan(\phi - \omega / 3.1) + \sqrt{1 + \tan(\phi - \omega / 3.1)^2} \tag{13}$$

instead of Equation 8. Somewhat lower values for p_c/c especially at the upper range of ω values are reached compared to the values in Table 4.

The length of the spall along the wedge side from the loaded level h_c can be calculated with Equation 6, Figure 33. The ratio of spall length to loaded plane length is relatively constant.

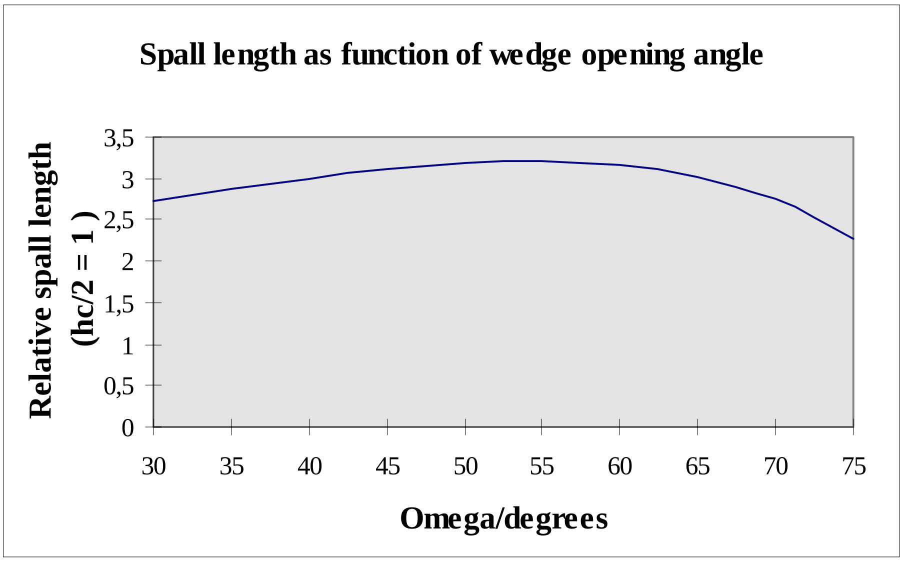

Figure 33. The spall length along the wedge side as a function of wedge opening angle.

The effect of the secondary wedge angle has been studied by using the same loading geometry but varying the wedge angle. The nature of the principal stress direction trajectories does not change. If the secondary wedge angle decreases to zero the minimum principal stress direction is normal to the load surface at the surface itself but soon develops a radial nature. In essence removing the secondary wedge means that the load that was originally experienced by the main body through the secondary wedge is now directly loading the main body.

4.3.2 Unsymmetrically loaded wedge

The critical location, where the Mohr-Coulomb criterion is first met is at the corner of the trailing edge side of the wedge. This has been found from the FE-calculations. The slip surface will start from here and the wedge will more or less be torn away. The path of the slip surface and the load required to create it can in this case also be approximated with the radial principal stress direction distribution. The loaded surface is now one of the wedge sides instead of the wedge tip, Figure 34. If δ is now the angle of the secondary wedge, the angle ζ between the symmetry axis and the wedge surface is

$$\varsigma = (3\pi - \delta) / 4 \tag{14}$$

and the angle between the symmetry axis and the other wedge surface ω is

$$\omega = (3\delta - \pi) / 4 \tag{15}$$

The load against the theoretical load plane $h_c/2$ is actually somewhat inclined from the direction against the wedge side. This results in a factor k:

$$k = 1 / \cos\left(\frac{\pi - \delta}{4}\right) \tag{16}$$

in the critical load. The value for this correction factor is close to 1 for reasonable angle combinations and is accordingly omitted in the subsequent numerical calculations.

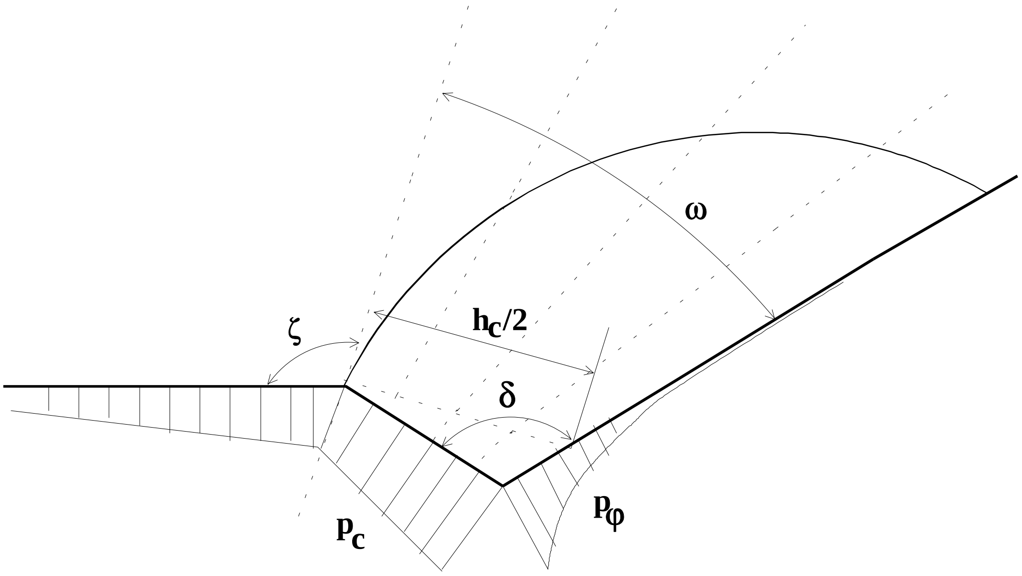

Figure 34. The idealisation of radial principal stress distribution in the case of an unsymmetrically loaded wedge.

The effect of the secondary wedge angle is similar to the case of a symmetrically loaded wedge. The nature of the principal stress direction trajectories does not change if the angle is varied. If the secondary wedge is removed the minimum principal stress direction is normal to the loaded surface but it turns fairly soon to follow the ice edge. The difference is that the load plane $h_c/2$ reaches now from the wedge corner to the peak of the pressure distribution.

4.3.3 Ice strength

The effect of ice strength on the maximum pressure that the solid ice can sustain and accordingly on the actual numerical values of Mohr-Coulomb parameters is of interest. Fransson et al. (1991) discuss the critical ice strength in a failure scenario of contact line and flaking, resembling the symmetrically loaded unconfined wedge case. The pressure at the contact zone creates the load needed for the flaking failure. The maximum pressure is limited to the melting pressure. Hallam and Nadreau (1987) have given the following formula for estimating it:

$$p_c = 11|T|^{0.95} \tag{17 }$$

where p_c is in MPa and T in ^oC . For pressures below the melting pressure Fransson et al. use a strain rate dependent power law equation of Sanderson (1988), based on data from creep tests. It is questionable how well it describes the brittle behaviour. Regardless, the pressures are limited to the melting pressure in the range of strain rates of 0.1 to 1 which were actually reached in the profile pressure distribution tests (section 4.3.5). For the test case of -2 ^oC Equation 17 would give a p_c value of 22 MPa and for the case of -4.5 ^oC 46 MPa respectively. In particular the lower peak value might be realistic. Measurements of the profile pressure distribution tests gave for thin ice cases a typical peak pressure value of 8.1 MPa for the -2 ^oC ice and 13.8 MPa for the -4.5 ^oC ice. The maximum measured peaks were 15 MPa and 20 MPa respectively.

Daley (1991) has combined the Mohr-Coulomb model and Hallam´s (1986) wing crack model for compressive cracking in ice to derive values for the Mohr-Coulomb parameters:

$$\sin\phi = 0.47059\mu + 0.52941 \tag{18}$$

$$c = 1.0625\sigma_{pc}\sqrt{\frac{1-\mu}{\mu + 3.25}} \tag{19}$$

where μ is the ice-ice inner friction factor in Hallam´s model for compressive cracking of ice and σ_{pc} the crack propagation stress of ice under uniaxial compression. Based on the assumption that μ is zero when the ice temperature T = 0 ^oC, Hallam´s model gives for μ:

$$\mu = \frac{-0.39T}{3.18 - 0.39T} \tag{20}$$

It can be seen that the minimum possible value for ϕ would be 32^o.

An attempt to combine these Mohr-Coulomb parameter values with the results of the profile pressure distribution tests was made. The tests were performed in temperatures of -2 ^oC and -4.5 ^oC. This would give μ values of 0.197 and 0.355 and respectively ϕ values of 38^o and 44^o. σ_{pc} of the tests can be based on the uniaxial compression test results. For temperatures of -2 ^oC and -4.5 ^oC the strength values were across the grain direction 1 MPa and 2 MPa respectively. The compression tests were performed with a strain rate of 2×10^{-4} s^{-1}. The true brittle strengths are considered to be 0.65 times these values in the transition region, Schulson (1990). σ_{pc} is thus 0.65 MPa and 1.3 MPa for these two temperatures. c will get the values from $0.51\sigma_{pc}$ to $0.45\sigma_{pc}$ for μ values from 0.197 to 0.355. 0.5 σ_{pc} is selected and gives c = 0.325 MPa and c = 0.650 MPa for both temperatures.

The μ values and accordingly ϕ values are considered to be fairly high. Daley uses $\mu = 0.1$ and $\phi = 35^o$ for ice at -6 ^oC. The proper value for ϕ for both ice strengths is estimated from the profile pressure distribution test results (assuming that the values for c as developed above are correct). The pressure distribution against the ice sheet is triangular in the vertical thin ice spalling cases, see Figure 35. According to the de Saint-Venant principle the stress in the y-direction is constant at some distance from the loaded surface where y = 0. The slip line is considered to start from the intersection of the ice edge and the symmetry axis. In this area there is a compressive stress $\sigma_z = \sigma_y$ according to the principles of contact mechanics. This stress in the minor principal stress direction z is fairly local. A constant stress $\sigma_z = \sigma_y$ is applied in this estimate in the z -direction in the range of z = 0 to z = 0.1 h, where h is the thickness of the ice sheet.

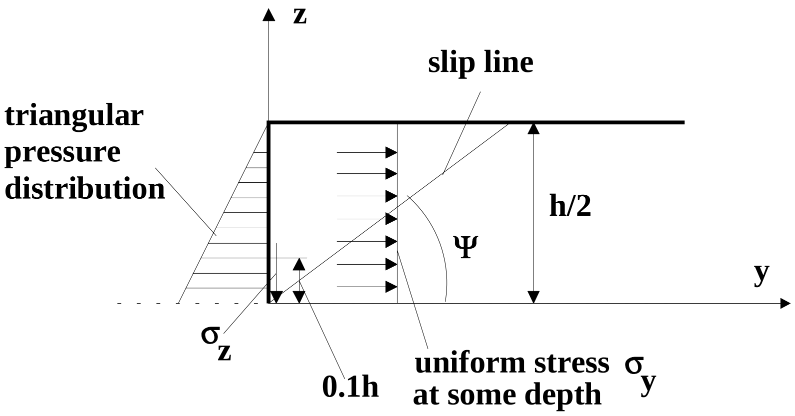

Figure 35. The loading geometry of thin ice.

The measured typical maximum pressure values are used in the following as such - no correction is made due to the orientation of the contact line against the pressure sensors. In the case of $\phi = 35^o$, c = 0.65 MPa, σ_y = 13.8 MPa the average pressure required for the slip line to occur would be 7.6 MPa according to Equation 2 (taking σ_1 and σ_3 directly in the y- and z-axis directions) and the peak of a triangular pressure distribution accordingly

12.7 MPa against the measured 13.8 MPa. Applying $\phi = 45^o$ and c = 0.65 MPa would lead to a 19.2 MPa peak. In the case of $\phi = 35^o$, c = 0.325 MPa, $\sigma_y = 8$ MPa the average pressure would be 4.2 MPa, the peak being 8.4 MPa.

The result of this exercise means that the variation in c would be enough to explain the strength differences in these unconfined cases and ϕ would be more or less constant and in the vicinity of 35^o. The observations of angle ψ of the thin section photographs, however, give values of 45^o to 60^o. This means that ϕ would be zero or negative. This can partially be explained by the vertical grain orientation that tends to turn the slip line in the grain direction.

4.3.4 Confinement, local crushing

The pressure required to cause a failure in the solid ice is compared in Table 4 for both basic loading cases applying the radial stress distribution for both an unconfined and a confined situation. The result for the triangular confining pressure situation is determined by applying Equation 12 and performing a numerical integration. It is evident that the confinement has a radical effect on the load that is required to cause the slip surface to occur.

Table 4. The effect of confinement on p_c / c, the critical pressure / cohesion ratio.

Wedge half angle ω [^{o}]	ϕ [^{o}]	p_c / c No p_φ	p_c / c Confining even p_φ	p_c / c Triangular p_φ distribution p_φ is the maximum pressure value in φ direction at r = 0
45	35 10	6.76 2.93	$6.76[1+0.960\ (p_\varphi /c)\ ]$ $2.92[1+0.596\ (p_\varphi /c)\ ]$	$6.76[1+0.960\ (p_\varphi /c)x0.388]$ $2.92[1+0.596\ (p_\varphi /c)x0.323]$
60	35 10	7.44 2.74	$7.44[1+0.960\ (p_\varphi /c)\ ]$ $2.74[1+0.596\ (p_\varphi /c)\ ]$	$7.44[1+0.960\ (p_\varphi /c)x0.405]$ $2.77[1+0.596\ (p_\varphi /c)x0.358]$
75	35 10	7.26 2.19	$7.26[1+0.960\ (p_\varphi /c)\ ]$ $2.19[1+0.596\ (p_\varphi /c)\ ]$	$7.26[1+0.960\ (p_\varphi /c)x0.378]$ $2.19[1+0.596\ (p_\varphi /c)x0.348]$

As a typical example the case of a 60^o wedge half angle was studied using the c values proposed above. The required failure pressure for the unconfined situation and for a triangularly shaped confinement load situation are presented in Table 5. The maximum values of p_φ at the wedge tip are given as 15 MPa and 30 MPa. Both symmetrical and unsymmetrical loading cases are presented. It is evident that the higher internal angle of

35^o, considered realistic in section 4.3.3, leads to unrealistically high critical pressure values in the case of a fully triangularly shaped confining pressure. For a meaningful pressure distribution the critical pressure p_r in the major principal stress direction must be equal to the highest pressure p_φ at r = 0 in the minor principal stress direction.

The condition for the maximum confining pressure in a triangularly shaped distribution along the wedge sides is also given in Table 5 for both critical r-direction pressure values of 15 and 30 MPa. This means that for failure to occur the peak pressure in the r-direction for a ϕ value of 35^o is in practice higher than the highest pressure along the wedge sides and the confining pressure distribution must be curved. In the unsymmetrical case it is assumed that the pressure in the r-direction along the trailing edge side of the secondary wedge is uniform. This means that the pressure that rises towards the wedge tip from the corner of the wedge is actually an additional load. It is not required for failure. The pressure at the corner of the wedge is decisive for the failure to occur.

Table 5. p_r *critical pressure for various loading cases.*

	Symmetrical loading, wedge angle 120^o				Unsymmetrical loading, wedge angle 120^o			
ϕ [^{o}]	35		10		35		10	
c [MPa]	0.325	0.65	0.325	0.65	0.325	0.65	0.325	0.65
Unconfined critical pressure p_r [MPa]	2.42	4.84	0.89	1.78	2.20	4.39	0.95	1.90
Critical pressure p_r [MPa], triangular distribution of σ_φ								
max σ_φ = 15 MPa	46	50	9.8	10.7	40	42	9.4	10.3
max σ_φ= 30 MPa	89	92	18.6	19.5	78	80	17.8	18.8
Maximum confining pressure [MPa] within triangular load distribution for failure to occur								
p_r = 15 MPa	4.35	3.51	23.84	22.34	5.08	4.21	24.00	23.31
p_r= 30 MPa	9.54	8.70	49.20	47.73	11.04	10.17	51.68	50.00

It can be seen that the c-value does not have a big influence in the confined loading cases. The internal friction angle ϕ is a more important parameter which is rational since it affects the term that takes the confining load into account in Equation 2. The importance of the confining load to the failure of ice is a well known fact. In the present slip surface approach a high degree of confinement effectively hinders the formation of slip surfaces. The result is that the peak pressure at the wedge tip will start to rise. A failure will take place as local crushing and coalescence of micro-cracks. This is one of the failure scenarios discussed in section 1.3.1. Another possibility is that the confinement will be released due to some geometrical change of the crushed ice channel elsewhere. Failure by formation of a slip surface will result. The numerical pressure peak values both for a moderate confinement resulting in a spalling failure and for a high confinement producing local crushing are difficult to assess.

The unconfined critical pressure values are clearly too low to be realistically used in the model. This means that some confinement is always present. Even the very local confining pressure in the vicinity of the loading plane in the vertical spalling case is enough to produce the required failure pressure as shown in section 4.3.3. The general shape of the pressure distribution, generated by the extrusion of crushed ice, and accordingly the confinement pressure will be dealt within section 5. However, an accurate estimate of the maximum confining pressure is not possible because it also depends on the peak pressure required to create the failure in the solid ice. The peak pressure values therefore have to be based on the test measurement results. As discussed in the previous section the typical peak pressure values for the vertical spalling cases are approximately 8 MPa and 14 MPa for the test temperatures -2 ^{o}C and -4.5 ^{o}C, respectively. The mean pressure in the high pressure area along the tool in the massive ice test case is, on the other hand, as shown in section 2.3.3 about 1.7 - 1.8 times the corresponding cold thin ice pressure, in other words some 10 MPa. The same ratio between the mean pressure and the peak pressure values as in the thin ice case is assumed in spite of the fact that the conditions of extrusion differ. Peak pressures of 23 MPa are thus realistic. The dependence of ice strength is more difficult to establish. For the vertical, less confined spalling case the ratio between the maximum pressures is 1.7 for a uniaxial compressive strength ratio of 2. For the more confined massive ice case this ratio would probably be somewhat less, as ϕ, the internal friction angle, was in section 4.3.3 considered to be rather insensitive to ice strength. A ratio of about 1.5 leads to the following proposed formula for critical peak pressure p_r:

$$p_r = 15\sigma^{0.6} \tag{21}$$

where σ is the brittle uniaxial compressive strength.

Extremely high pressure values were not registered in the profile pressure distribution tests. However, some very local peaks that did not affect the global loads could have taken place in the massive ice case in areas of the tool without pressure sensors. The absolute maximum pressure is the melting pressure for the actual temperature, Equation 17 .

Some triaxial ice strength test results are available. According to Jones (1982) data for granular ice the required deviatoric stress $\sigma_1 - \sigma_3$ is 25 MPa higher than the confining pressure $\sigma_2 = \sigma_3$ in the brittle regime. This would require for a confining pressure of 15 MPa a failure pressure of 40 MPa.

According to Gratz and Schulson's (1994) data for columnar grain ice, the increase in the uniaxial compressive strength σ_1 in the across grain direction due to biaxial confinement (σ_2 varies from 0.25 x σ_1 to 1 x σ_1, $\sigma_3 = 0$) is by a factor of 3 - 4. An increase of a moderate triaxial confinement along the columns (stress in σ_3 direction) increased the critical stress for σ_1 some 50 % from the biaxial case. A greater confining load in this direction did not change the critical stress. These tests were performed for ice at -10 ^{o}C temperature using a strain rate of 10^{-2} s^{-1}. The biaxial case corresponds with the thin ice case of the profile pressure distribution tests. The actual load occurs mostly in the y-direction in Figure 9 and the confinement in the x-direction. Thus additional confinement in the z-direction in the massive ice case would increse the critical load in the y-direction some 50 %. This agrees with the 67 % increase in peak pressures between the cold thin ice tests and massive ice tests assumed above.

4.3.5 Friction and strain rate

A FE-analysis with the IDEAS-program was performed to study the effect of frictional forces. A tangential force along the wedge surface was applied varying the friction coefficient from 0.01 to 0.5. The effect of friction was found to be limited quite close to the wedge surface where the principal stress direction is angled somewhat from the normal against the surface. Deeper within the material the principal stress directions are not affected. The material flow at the wedge side towards the trailing edge makes the stress direction closer to the radially distributed idealisation in the unsymmetrical loading case.

The effect of strain rate can be studied based on the test results of the two impact speeds of the profile pressure distribution tests. The two strain rates can be estimated as follows. For the faster tests the average stress rate from the measured signals is 6 - 8 MPa/ms. Using the value 7 GPa for the modulus of elasticity, the strain rate 1 s^{-1} is obtained. Accordingly for the slower tests the stress rate is some 0.8 - 1.8 MPa/ms, giving a strain rate of 1 - 2.6 x 10^{-1} s^{-1}. Both values are clearly within the brittle failure mode. As described in section 2.3.4 the failure mechanism clearly differed, however, in the slower tests. The ice was cracked into fairly large spalls instead of being crushed and extruded. On the other hand, the measured pressure levels did not differ from the faster tests. The pressure distribution time history showed somewhat more violent behaviour compared to the faster tests. It can be concluded that the failure mechanism is different for slower speeds but there is not enough data to make estimates of numerical differences in the effective pressure levels.

4.3.6 Discussion

There is not a major difference between the critical wedge pressures for the symmetrical or unsymmetrical loading cases. The strength of ice has a smaller effect on the critical wedge pressure than the degree of confinement in the minor principal stress direction. The internal friction angle ϕ is realistically in the order of magnitude of 35^o.

Realistic critical pressure levels for the unsymmetrical loading case can be predicted with the method. The absolute pressure levels are, however, strongly dependent on the confinement and accordingly the proper value of the pressure variation at the leading edge of the profile (as shown in Section 5) The average peak pressure values of the profile pressure distribution tests must be used as a guideline. The peak pressure is in the range of 15 - 30 MPa, depending on the ice strength, as described above and the measured average leading edge pressure is 2 MPa. These values are in line with the data in Table 5. If the channel of crushed ice towards the leading edge converges a symmetrical loading case will occur. The model predicts that the maximum pressure at the wedge tip grows to a level at which the ice starts to be crushed. Extremely high pressures were, however, not measured in the tests. These pressure spikes are considered to be so sharp that they can be omitted in the overall effective load prediction.

5 CRUSHED ICE

5.1 GENERAL

Once the ice has been crushed it must be removed to enable the blade to proceed. Two basic approaches have been proposed in modelling the flow of crushed ice. The continuum behaviour of solid ice is viscoelastic. A viscous theory has accordingly been proposed for crushed ice. The theory was suggested for the first time by Kurdyumov and Kheisin (1976) for an indenting ball, assuming the crushed ice to behave as a Newtonian fluid. Since then, several viscous models have been presented for extrusion between parallel plates, Hallam and Pickering (1988), Jordaan and Timco (1988) and Singh et al. (1993). The other approach is to assume the crushed ice to be granular and to apply the Mohr-Coulomb failure criterion in accordance with soil mechanics flow models. There exist a few models based on a simple Mohr-Coulomb approach by Hallam and Pickering (1988), Finn et al. (1989). Savage et al. (1992) have presented a more rigorous analysis for a general case of extrusion between curved plates. Daley et al. (1996) have developed a combined flaking and crushing model based on a simplified approach of the Savage model.

A great number of analyses have been performed to verify the various models with test data. The granular Mohr-Coulomb theory has usually been considered to better explain the results, Tuhkuri and Riska (1990), Savage et al. (1992). Especially at a lower pressure range (less than 7 MPa), Finn et al. (1989), the pressures follow the general shape of the granular models. Recent interpretations, Singh et al. (1993) and Tuhkuri (1994), seem to support the following process. In the beginning, at low pressure levels, the granular Mohr-Coulomb theory, leading to exponent-shape curves with a sharp spike at the maximum pressure location will be correct. At a later stage, when the channel width decreases, the ice is sintered in the high pressure areas of the channel, furthest from the outlets, and no longer behaves like a granular material. The behaviour may be elastic, viscous, viscoelastic or viscoplastic. The observed pressure distributions follow a roughly parabolic pressure distribution as do the viscous models. The material in the areas close to the channel outlets still behaves in a granular way.

The difference between the published tests performed with the crushed ice and the propeller blade case is that the blade constantly glides along the channel of crushed ice. The “watershed” area, the area of maximum pressure, moves along with the location of the solid ice wedge tip. An important observation from the profile pressure distribution tests is that the crushed ice mass layer that is left on the ice / blade contact surface after the blade has passed is compacted. This means that once the crushed ice has been compacted in the high pressure area it no longer has a granular pulver like form in the flow towards the trailing edge but occurs as a sintered mass, as pointed out in section 2.3.5.

The physical nature of the compacted crushed ice is of interest. It may be argued that the compacted crushed ice is observed after the tests in “post mortem” condition. The mass may be more loose during the flow and then freeze together after the pressure is released. However, when crushed ice sinters, the bonds between grains grow, while the applied pressure and duration of the loading are increased, Maeno and Ebinuma (1983). Cocks (1994) has developed constitutive models for sintering of fine grained materials. The densification procedure during which individual particles bond together can be divided into two stages. In the first, early stage, the porosity is connected and discrete necks exist between the particles. In the second stage when the relative density is greater than 0.9 the porosity closes leaving isolated pores between the grains. The sintering process is also related to pressure melting. The local pressure between the grain bonds may be large enough for melting.

The crushed ice that is extruded towards the leading edge is clearly found from the profile pressure distribution tests with zero cut width to be blown out as bursts of fine grain pulver. The approach for this work is thus to combine a granular model at the leading edge extrusion and a viscous model for the compacted crushed ice extrusion towards the trailing edge. When crushed ice is formed from solid ice its density must collapse to give room for the pores. The required density decrease is produced after formation of a new spall by extrusion of granular material towards the leading edge. The compaction of the crushed ice in the vicinity of the previous wedge tip is released and it might also be extruded in granular form towards the leading edge, Figure 36.

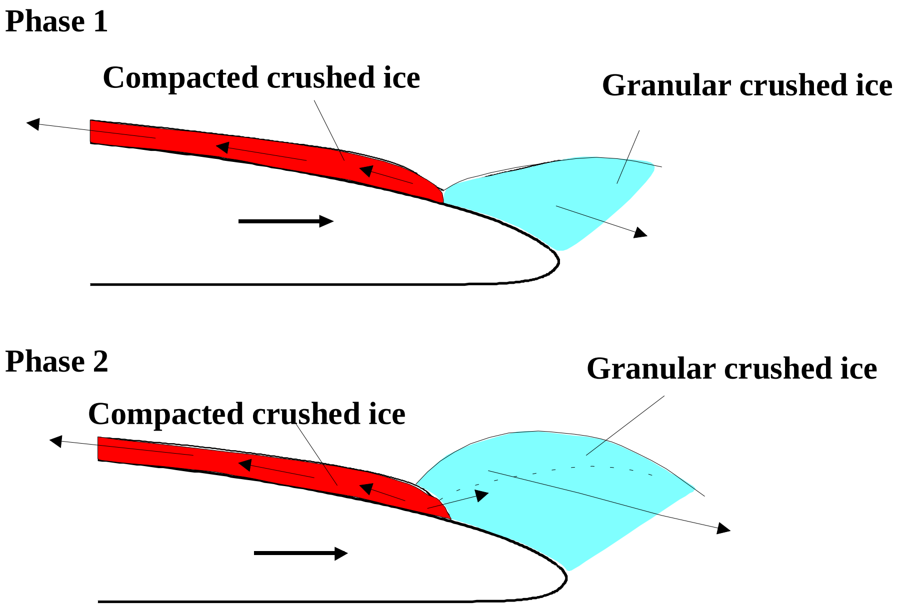

Figure 36. The two regimes of crushed ice.

If the compacted mass is assumed to be more or less incompressible a scenario is possible in which most of the crushed ice mass behind the new wedge tip area is extruded towards the trailing edge while the blade proceeds. The material (V_1 in Figure 37) that is removed by the blade towards the trailing edge must flow through the channel between the blade and the solid ice and end up at the tangential point of contact, to the point where the profile surface and solid ice border are parallel. The proceeding of the blade leaves space for the extruded mass. Depending on the ratios between the channel width h at the tangential point of contact and the projection H in the y-direction of the distance between the actual wedge tip and the tangential point of contact, this space (V_2 in Figure 37) may or may not be enough for the mass flow of sintered ice. Some of the ice mass may diverge at the tangential point of contact to the slot left by the blade. This creates a back-pressure. The net mass flow Q_{net} out of the channel and the velocity u for the flow out of the channel during the actual extrusion phase are

$$Q_{net} = U_P(H - h) \tag{22}$$

$$u = U_p(H / h - 1) \tag{23}$$

where U_P is the profile speed in the angle of attack direction.

The other scenario is that the already compacted mass is further compacted when the blade proceeds, but not extruded from the channel between the blade and the solid ice. The whole volume V_1 in Figure 37 would move only in the y-direction and be compacted within the channel of thickness h. Values of 550 to 600 kg/m^3 for crushed ice density are often used. This means that the maximum volumetric strain for the crushed ice in the compaction process is some 0.3. At that stage the ice is solid again. The strain would clearly be much too big if a movement in the profile direction does not take place. The conclusion is that after an initial compaction the ice mass can be considered as incompressible in the calculations of extrusion towards the trailing edge. The observations of Singh et al. (1993) from their extrusion tests and FE-simulation with the viscoelastic model are that extrusion, not just densification, goes on also in the sintered condition.

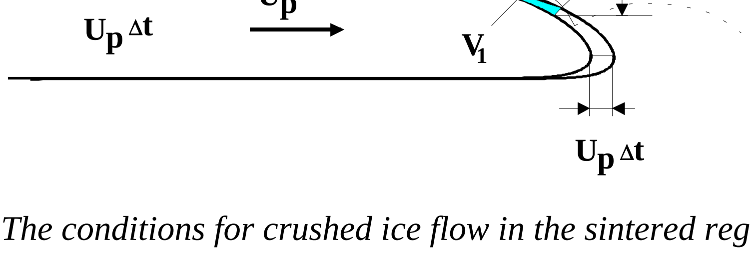

Figure 37. The conditions for crushed ice flow in the sintered regime.

Simple straight wall channels are assumed in the calculations. A more realistic curved wall geometry would not change the overall pattern of the pressure distribution. There are in any case unknown parameters, such as the channel thickness and viscosity, that affect the absolute pressure values. Therefore the extrusion models must be considered in this context more as possible qualitative explanations for the phenomena than rigorous models giving exact quantitative data.

Calculations have been performed for this work based on the momentum and impulse theory plus the observed velocity of crushed ice bursts at the leading edge in the tests. Any meaningful pressure rise will not occur due to the sharp 90^{o} turn of the mass flow from the profilewise direction at the leading edge. The acceleration of the mass flow from one burst to another also causes only a negligible pressure increase.

5.2 THE VISCOUS EXTRUSION MODEL

5.2.1 General

One way to explain the behaviour of the sintered ice mass under high pressure would be to apply an elastic model since the compacted ice mass that is observed after the extrusion tests does not appear as a fluid. It is, however, known from some dispersions (Pierce and Schoff, 1982) that if the dispersion particles are attracted to each other, they tend to aggregate and form a structure. The structure may be so pronounced that the mixture behaves like a solid when it is at rest. Shearing breaks up the structure and the viscosity decreases. Crushed ice particles may well behave like this. When the extrusion phase comes to an end the particles may again freeze together. A combination of viscous and elastic or plastic is probably more correct than a pure viscous model. Singh et al. (1993) have discussed the elastic modelling in their paper. Based on the pressure rise (stress increase) as a function of the decrease in the channel thickness (i.e. strain) at the steep pressure rise stage, the modulus of elasticity can be calculated. A value of some 40 - 45 MPa is reached. Based on the stress rate and corresponding strain analysed from the profile pressure distribution tests, a value of 40 - 80 MPa is reached for modulus of elasticity. This is a few orders of magnitude less than the modulus of elasticity for intact ice. Thus it may be argued that other mechanisms than elastic are dominant. Tuhkuri (1996) has shown in his model that the pressure increase at the ice structure contact after the pressure drop due to a cascade of flakes is elastic. In Tuhkuri´s test arrangement, however, there existed a direct contact between ice and the structure.

There exist two basic models with a mechanical analogy for viscoelastic behaviour, Malvern (1969). In the Kelvin-Voigt model the total force is the sum of the elastic force and the viscous force, the displacment being the same for both elements, which are described with a spring and dashpot connected in parallel

$$F = E\varepsilon + \mu \dot{\varepsilon} \tag{24}$$

where E is the modulus of elasticity and μ viscosity. In the Maxwell model, the force is the same for both elements, a spring and a dashpot connected in series, but the displacements are added:

$$\dot{\varepsilon} = \frac{\dot{F}}{E} + \frac{F}{\mu} \tag{25}$$

In general, the Kelvin-Voigt model can be considered to explain delayed elasticity and the Maxwell model steady creep. Singh (1993) has developed viscoelastic models for solid crack-containing ice starting from Sinha´s (1979) model of ice as a continuum:

$$\varepsilon(t) = \frac{\sigma}{E} + \frac{c_1}{a}\left(\frac{\sigma}{E}\right)\left(1 - e^{-(a_T t)^b}\right) + \dot{\varepsilon}_0\left(\sigma / \sigma_0\right)^n t \tag{26}$$

where the strain components are the elastic, the delayed elastic and the secondary creep; σ is the uniaxial creep stress, E is the modulus of elasticity, a the grain size, a_T and $\dot{\varepsilon}_0$ are functions of temperature, and c_1, b, σ_0 and n are constants. Singh has combined the Kelvin-Voigt and Maxwell models in series to describe the model of Equation 26, as presented also for example in Sanderson (1988). The model is extended to crushed ice idealising the crushed ice to be a continuum where uniformly distributed pores and grain boundaries are embedded in an isotropic matrix. The model explains some triaxial compression tests performed for crushed ice well. It must be noted, however, that the model contains a lot of parameters, the correct value of which are not necessarily known. Singh states that if the long term response is the main concern, better performance from the model can be obtained by sacrificing the elasticity of the material. Singh (1993) has also applied the material model to a FE-model and simulated some extrusion tests. The results are logical when compared to the test results - the pressure distribution is of the correct shape and the densification similar to that measured in some test cases.

The strains are large for the scenario of material extrusion towards the trailing edge. The elastic term should accordingly be omitted in the viscoelastic model. A viscoplastic model is one possibility that gives a better explanation than a pure viscous model for the extrusion phenomena of crushed ice. A viscoplastic material differs from a fluid in the sense that it can sustain a shear stress in rest, but when the stress intensity reaches a critical value (yield condition) the material flows with viscous stresses proportional to the excess of the stress intensity over the yield-stress intensity.

If the compacted ice is loose, a suspension model can be considered and a two phase flow takes place - the ice grains are surrounded by water. After the flow the grains freeze together. The nature of a sintered ice mass does not, however, support such a scenario. The maximum possible increase of plain water viscosity is also a few orders of magnitude too small.

5.2.2 Viscous component

There exist at least three models for the simple case of crushed ice between two parallel walls that come together at a constant velocity. Hallam and Pickering (1988) presented a simple solution treating crushed ice as a Newtonian fluid. Jordaan and Timco (1988) also presented a model for a Newtonian fluid. Singh et al. (1993) have presented the solution for a flow following power law. If linearity is applied to this model, it yields the same solution as the two previous models. Comparative calculations by Singh et al. (1993) show that linearity vs. nonlinearity does not have a great effect on the shape of the pressure distribution. For this work the linear, Newtonian fluid, is assumed and a model developed for channels with inclined walls with one wall gliding with respect to the other wall.

The flow is assumed to take place between the blade and the solid ice. These two surfaces are inclined at an angle α to each other, Figure 38. The slight curvatures of the surfaces are not taken into account. The x - axis is defined along the blade surface, with zero at the location of the ice wedge tip. The angle α is assumed to be relatively small:

$$h = h_1 + \alpha x \tag{27}$$

where h_1 is the thickness of the channel h at x = 0. α is positive when the channel diverges in the flow direction. The blade moves with a velocity V against the solid ice:

$$V = U_P \sin\beta \tag{28}$$

where U_P is the velocity of the profile in angle of attack direction and β the angle between the angle of attack direction and the x-axis, i.e. the surface of the profile. U, the gliding speed of the blade surface is

$$U = U_P \cos\beta \tag{29}$$

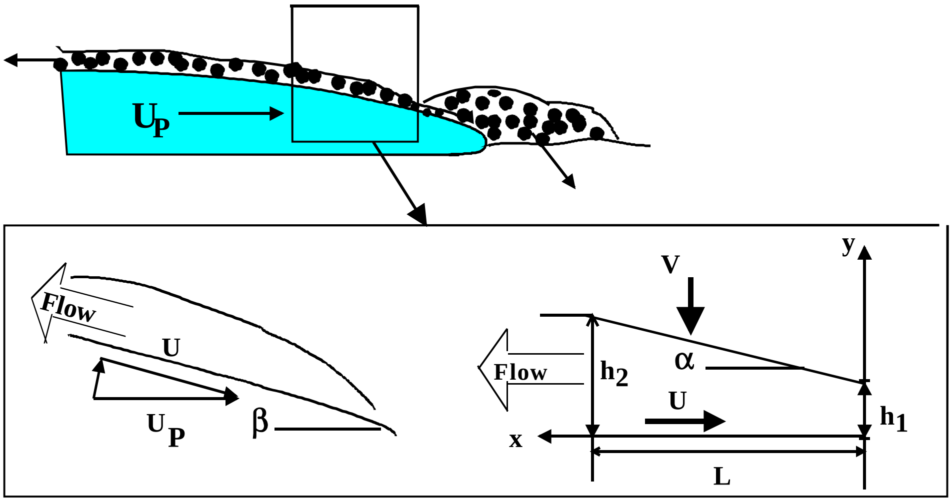

Figure 38 . The definition of the channel coordinates.

The crushed ice is assumed to follow Newton´s law of fluid friction:

$$\tau = \mu \frac{\partial u}{\partial y} \tag{30}$$

where μ is the dynamic viscosity and u the flow velocity in the x direction. Navier-Stokes equations are applied and simplified as follows, according to the hydrodynamic theory of film lubrication, presented for example in Kaufmann (1963): the inertia terms are negligible in comparison with the friction terms, the body forces are disregarded and the flow assumed to be steady. The velocity component in the y direction can be neglected in comparison with the velocity u in the x direction. The reduced Navier-Stokes equations are

$$\frac{\partial p}{\partial x} = \mu \Delta u \qquad\qquad \frac{\partial p}{\partial y} = 0 \tag{31}$$

where Δ is the Laplacian. The term $\partial^2 u / \partial x^2$ can be neglected when compared to $\partial^2 u / \partial y^2$ since the curvature of the velocity profile u in the y direction is far greater than in the x direction. Since p = p(x) is a function of x only, $\partial p / \partial x = dp / dx$. Thus

$$\frac{dp}{dx} = \mu \frac{d^2 u}{dy^2} \tag{32}$$

Integrating twice with respect to y gives

$$u = \frac{1}{\mu} \frac{dp}{dx} \frac{y^2}{2} + C_1 y + C_2 \tag{33}$$

The boundary conditions are u = -U, when y = 0, and u = 0, when y = h. Hence

$$u = U(\frac{y}{h} - 1) + \frac{dp}{dx}\frac{(y^2 - yh)}{2\mu} \tag{34}$$

Here the U-term is due to the movement of the wall at y = 0, i.e. the couette flow. The second term is identical to the velocity u of the Singh et al. model in the case of linear constitutive behaviour of flow, i.e. Newtonian. The continuity condition of the flow gives

$$Q_{net} = Vx = \int_0^{h(x)} u dy \tag{35}$$

where Q_{net} is the net mass flow. It is assumed that the "watershed", at the tip of the wedge hinders the mass flow towards the leading edge. That is why the net flow consists only of the component of removal of mass due to the approaching channel walls regardless of the couette flow to the opposite direction. At x = 0, the wedge tip, there is thus a point where the couette u-component is zero. This approach gives somewhat higher pressure values than just combining the slider behaviour, Kaufmann (1963), and the behaviour due to the approaching walls. The flow would not be hindered at x = 0 and the pressure would be atmospheric at both ends of the channel. The shape of the distribution is not affected much by either approach. Thus integrating Equation 34 with respect to y gives

$$\frac{dp}{dx} = -\frac{12\mu Vx}{(h_1 + \alpha x)^3} - \frac{6\mu U}{(h_1 + \alpha x)^2} \tag{36}$$

Integrating with respect to x gives finally

$$p = p_L + \frac{12\mu V}{\alpha^2}\left[\frac{1}{h_1 + \alpha x} - \frac{1}{h_2} - \frac{h_1}{2(h_1 + \alpha x)^2} + \frac{h_1}{2h_2^2}\right] + \frac{6\mu U}{\alpha}\left(\frac{1}{h_1 + \alpha x} - \frac{1}{h_2}\right) \tag{37}$$

when boundary condition $p = p_L$ at x = L is taken into account and using notation $h_2 = h_1 + \alpha L$. It would be possible also to define $p = p_0$ at x = 0, but this could easily lead to negative pressures close to x = L depending on the selected combinations of p_0 and other parameters. The proper value for p_L may be argued; is it 0, the atmospheric pressure plus the hydrostatic pressure at the depth of the propeller blade or something more? 1 MPa was measured from the profile pressure distribution tests. Regardless, selected value just adds to the other components of the pressure. The effect on the maximum pressure at x = 0 is thus minor.

If Equation 36 is used to find the velocity profile from Equation 34 in the y-direction the general behaviour is as shown in Figure 39.

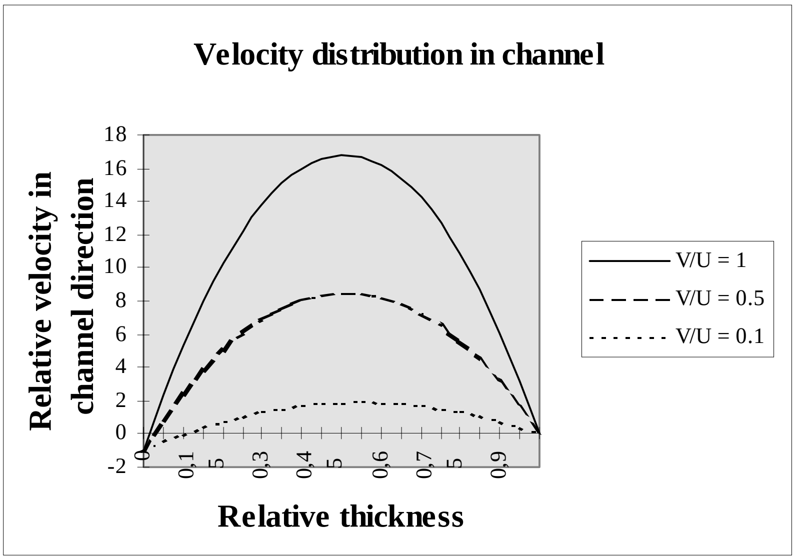

Figure 39. Typical velocity distributions in the channel at the outlet h = h_2. μ is constant, h/L = 0.1 and V/U is varied as parameter. (Note: the flow direction is along the vertical axis and channel thickness along the horizontal axis!)

A study of the relative importance of the inertia terms was performed for the present work, based on the acceleration of the crushed ice in the channel (as obtained from the equation of continuity). The result was found to give pressure values a few orders of magnitude smaller than the viscous forces, depending on the value of viscosity applied.

The absolute pressure values depend on the viscosity and profile velocity values to the first power and on the inverse of the channel thickness to the second and third power. The maximum pressure is in any case governed by the solid ice strength, and the combination of viscosity and channel thickness will always lead up to this range at the moment of failure. The absolute values for both the channel thickness and viscosity are thus of minor importance for the shape of the pressure distribution. An example of numerical calculations to show the effect of channel slope is given in Figure 40. (Note that Equation 37 can also be used for calculation of the pressure distribution in a converging channel).

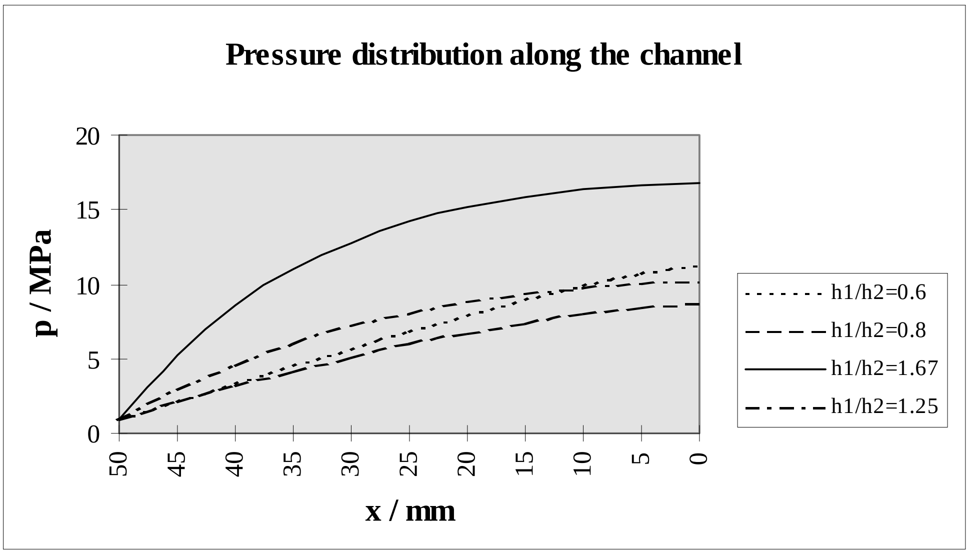

Figure 40. The effect of channel slope on the pressures according to Equation 37. Gliding speed U =9.1 m/s, approaching speed of the walls V=4.2 m/s, viscosity μ =0.00001 MPa s, pressure at the outlet p_L=1 MPa, channel length L =50 mm and channel thickness at the outlet h_2 = 5 mm for the diverging channel and thickness at the inlet h_1 = 5 mm for the converging channel.

The channel of crushed ice may have an approximately parallel walled portion beyond the diverging part from x = L onwards. The walls do not approach each other here, i.e. V = 0 and $h_1 = h_2$ in Equation 37. Thus p depends only on the speed of net mass flow in the channel according to the well known equation for flow between parallel walls:

$$p = p_L + \frac{12\mu u_a}{h^2}(L - x) \tag{38}$$

where u_a is the average velocity in the x-direction.

The net mass flow velocity depends on the actual position of the wedge tip in the y-direction according to Equation 23. This means that for thick profiles at the moment when the wedge tip is close to the leading edge there may be a flow through the parallel part of the channel. When the wedge tip is closer to the beginning of the parallel walled part of the channel a flow does not exist, and accordingly neither a pressure drop, within this part of the channel. To study the effect of flow velocity in a parallel walled channel the parameters used in the Figure 40 calculations are applied in Equation 38 (h= 5mm, L = 50 mm, μ =0.00001 MPa s, p_L=1 MPa). This results in p = 1.2 - 2.2 MPa where u_a varies between 1 and 5 m/s.

It is obvious that for larger values of u_a the pressure rise in the channel should be taken into account in p_L for calculations with Equation 37, raising the level of the curves in Figure 40 accordingly. Here again, however, the argument of the absolute level of the maximum pressures depending on the solid ice strength will balance the combination of channel thickness and viscosity. The shape of the pressure distribution along the whole channel is dependent on the actual u_a within the parallel part of the channel - varying within the phases of the extrusion process of the same section. The pressure along the whole parallel part of the channel may be constant and in some instances rise towards the diverging part of the channel.

There are many opinions on the correct range of viscosity for crushed ice. Jordaan and Timco (1988) recommend 0.1 MPa s, which would, according to the measured pressures in the profile pressure distribution tests, lead to far too high pressure values for realistic channel thicknesses. Finn et al. (1989) report a rate dependence for viscosity. Extrusion test results were analyzed and a best fit for viscosity gave the values of Table 6. In a log - log plot the viscosity velocity dependence becomes quite linear. Tuhkuri (1994) has presented the results of some crushed ice extrusion experiments. The pressure increase as a function of channel width decrease can be followed from test case 21 in those tests. Solving Equation 36 for a geometry of parallel walls without couette flow, and applying the channel and the pressure values of the test case, a viscosity of some 0.03 MPa s is reached for the platen's velocity of 10.2 mm/s. This viscosity value fits the series of Table 6. The absolute platen velocity is here used as a measure of the shear rate. It depends on, besides the platen velocity relative to each other, the distance from the "watershed" of the crushed ice and also varies inversely to the second power on the channel thickness. If the normal velocity against the blade profile at the back side close to the leading edge is considered in the profile pressure distribution tests the extension of the Table 6 series would give a viscosity value of some 0.000 05 - 0.000 5 MPa s, which, when applied to realistic channel thicknesses as observed from the tests, give realistic pressure values.

Table 6. Viscosity versus channel closing speed from the Finn et al. (1989) tests.

Approaching velocity of the platens mm/s	Viscosity Mpa s
2.5 - 5	0.2 - 1.1
25	0.03 - 0.15
125	0.003 - 0.02
160	0.0009

This rate dependence as such is contrary to the assumption of a Newtonian fluid. The decrease in viscosity with increasing velocity tends to keep the shear stress constant, not rate dependent. This means that the crushed ice cannot be considered as a Newtonian fluid. Similar behaviour is noticed for example for some concentrated polymer solutions, where viscosity against shear rate decreases and the flow is shear thinning, (Pierce and Schoff, 1982). The behaviour may be Newtonian for these solutions at shear rates lower than 10^3 s^{-1}, but when the shear rate increases to 10^5 s^{-1} the viscosity decreases from some 10^4 to 10^2 mPa s. Thus the viscosity has to be understood as an apparent viscosity for each shear rate range. A power law model, such as used by Singh et al. (1993), is in principle able to follow the shape of the shear against shear rate in the shear thinning case:

$$\tau = k\left(\frac{du}{dy}\right)^n \tag{39}$$

However, the uncertainties of the correct power of shear rate and coefficient k (= viscosity if the power n = 1) remain, especially when extended over a broad range of shear rate. Thus it is considered accurate to use the Newtonian model and an apparent viscosity in each shear rate range.

It may also be argued that the viscosity depends also on the absolute pressure value of the sintered ice mass. The more the pressure rises, the closer the recrystallized ice is to solid ice. However, as discussed in section 5.1 the compacted ice mass can be considered to be incompressible after the initial compaction process close to the wedge tip. A viscosity pressure dependence is familiar in mineral lubrication oils where an exponential viscosity pressure relation is often applied:

$$\mu_p = \mu_0 e^{kp} \tag{40}$$

where μ_0 is the viscosity in atmospheric pressue and μ_p the viscosity at pressure p. k is a constant.

The pressure increase associated with the mode change of a granular extrusion model to the failure of the solid ice is within one order of magnitude and probably does not cause a major change in viscosity. An attempt to re-analyze the results of the Finn et al. (1989) test series did not give any pressure dependence on the viscosity.

5.2.3 Plastic component

The total resistance to motion for a viscoplastic Bingham material is

$$\tau = \tau_y + \mu\frac{du}{dy} \tag{41}$$

where the shear stress τ_y is a material property equivalent to the cohesion term of the Mohr-Coulomb model. Finn et al. (1989) present the equation for a Bingham material in the case of parallel walls coming together at velocity V, using the same symbols as in Equation 37:

$$p = p_L + \frac{6\mu V}{h^3}\left(L^2 - x^2\right) + \frac{6\tau_y}{h}\left(L - x\right) \tag{42}$$

where the first term is the viscous term and the second the plastic term. L is the length of the channel.

When numerical comparisons are performed it is found that the order of magnitude of 0.01 MPa for τ leads to reasonable results, If a value of some 0.5 MPa is chosen, which might be the shear strength value for intact ice, it leads to maximum pressure values of some 50 MPa in conditions comparable to the profile pressure distribution tests. The maximum pressure value is governed by the strength of the solid ice. Since the absolute values of the viscosity and the shear strength of the crushed ice mass are not known it is not of great importance if the pure viscous or the viscoplastic model is used. A mix of a shear strength value and a lower viscosity in the viscoplastic model or a higher viscosity in the pure viscous model lead to the same result as can be seen from Figure 41. The shape of the pressure distribution is fairly similar. If the rate independent shear rate dominates the distribution naturally becomes more linear.

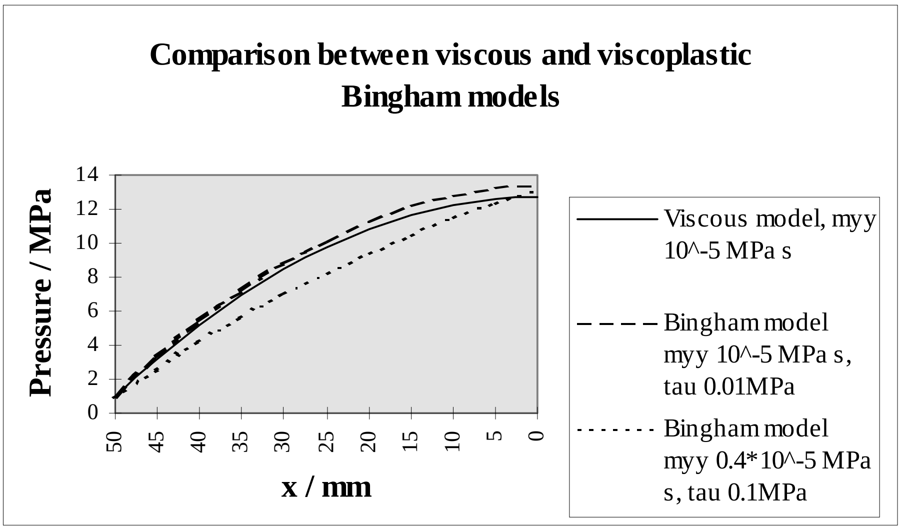

Figure 41. Comparison between the viscous and viscoplastic models in the parallel walled channel case. Channel thickness 5 mm, channel length 50 mm, approaching velocity of the walls 5 m/s.

5.3 GRANULAR EXTRUSION

5.3.1 Applicable models

Savage et al. (1992) have presented a solution for the general case of flow between two plates that may be curved. The solution is based on the equations for conservation of mass and linear momentum assuming the granular ice as an incompressible continuum with constant density. The friction for each wall may be different and a pressure acting on the boundary is possible. The solution in closed form is extremely lengthy and a numerical solution is more practical. A simpler closed form solution is possible when the plates are parallel and the wall friction is equal, Savage et al. (1992). Daley et al. (1996) discuss the Savage model and have developed a correction factor for the closed form parallel wall model to take into account diverging walls. They have also developed a simpler model omitting the cohesion, i.e. the material model is not Mohr-Coulomb. Numerical comparisons with the Savage model show good results. The straight wall model has then been extended to a model with inclined walls either vertical or horizontal. The basic solution for the straight wall case is basically similar to the Hallam and Pickering (1988) and Finn et al. (1989) models, with a simpler ratio between the wall pressure and the pressure in the flow direction. In these models a two-dimensional flow of the crushed ice mass is assumed in a channel that is formed of two parallel walls. A narrow channel is assumed. The mass forces are not taken into account in these models. The Mohr-Coulomb criterion is applied in the Hallam-Pickering and Finn models in the principal stress form. The limitation used in the models is that the principal stresses are assumed to act along and across the channel. This means that the friction forces must not be large enough to be able to rotate the principal stresses. The solution is quasistatic and gives, thus, only the limit analysis. The force balance according to Figure 42, from Finn et al. (1989), is

$$h d\sigma_3 = 2\mu p dx \tag{43}$$

where h is the distance between the channel walls and μ the friction coefficient between the wall and the crushed ice.

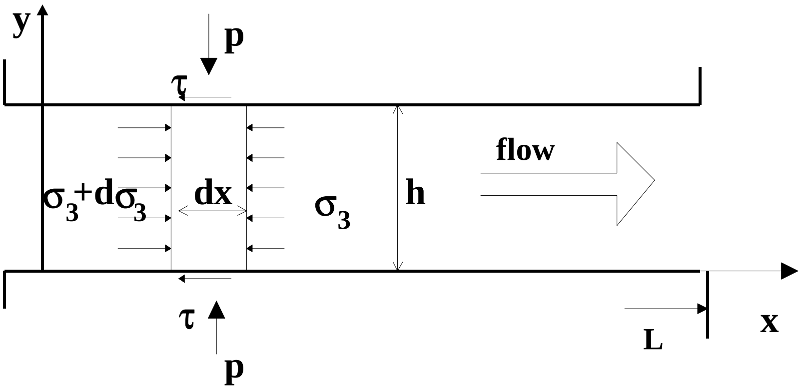

Figure 42 . The element of crushed ice (Finn et al. 1989).

Applying the Mohr-Columb material model for the crushed ice, Equation 2,

$$p = S_C + k\sigma_3 \tag{44}$$

where k = S_C / S_t´. Differentiating Equation 44 with respect to x and taking into account Equation 43 it can be shown that

$$p = S_C e^{\frac{2\mu k}{h}(L-x)} \qquad (45)$$

The Equation 45 is valid in the case where p = 0 at the outlet of the channel, x = L. If, instead of a half space, there is some constraint, e.g. a back-pressure, at the open end of the channel that causes a wall pressure p_L at the outlet of the channel, S_c has to be replaced with p_L in Equation 45. The Daley et al. model ends up with

$$p = \frac{pox}{k} e^{\left(\frac{Kx}{ho}\right)} \qquad (46)$$

where

K:	extrusion pressure coefficient $K = (\mu_i+\mu_s)/k$
μ_s:	ice-structure friction coefficient
μ_i:	ice-ice friction coefficient
k:	lateral pressure coefficient, $p= p_x/k$. The pressure on the side walls, p is pressure in flow direction p_x (σ_3 in Equation 44) divided by k.
ho:	the channel thickness at x = 0. The x- coordinate is defined differently than in Figure 42. x = 0 at the outlet of the channel.
pox:	ice pressure in x-direction at x = 0.

The Daley et al. model for horizontal sloping walls is

$$p = \frac{pox}{k}\left(1-\alpha\frac{x}{ho}\right)^{\left(-\frac{Ka}{\alpha}\right)} \qquad (47)$$

where

$$Ka = \frac{\mu_i + \dfrac{\mu_s\cos\alpha - \sin\alpha}{\cos\alpha + \mu_s\sin\alpha}}{k},$$ where α is the slope angle.

By selecting the ratio L/k in Equation 46 the same as $k = S_C / S_t'$ in Equation 45 and pox/k the same as p_L in Equation 45 both models give the same result. The models are quite sensitive to the width / length ratio of the channel, the external friction coefficient and internal friction coefficient or the pressure coefficient in Equation 46. Pressure at the outlet of the channel affects the pressure in direct proportion. Some parameter variations have been calculated to show the sensitivity, in Figure 43. The basic parameter values used are 0.05 for the friction coefficient between the crushed ice and the blade (the same value is used for the friction against the solid ice), and 24° for the internal friction angle (leading to the value k = 0.422 in Equation 46). These values are in line with the values used in the work of Savage et al. (1992). If h/L is set to 0.1, doubling the external friction coefficient to

0.1 or doubling k in Equation 46 (meaning internal friction angle 40.67°) will give the same result as h/L = 0.05 with the original μ and ϕ values.

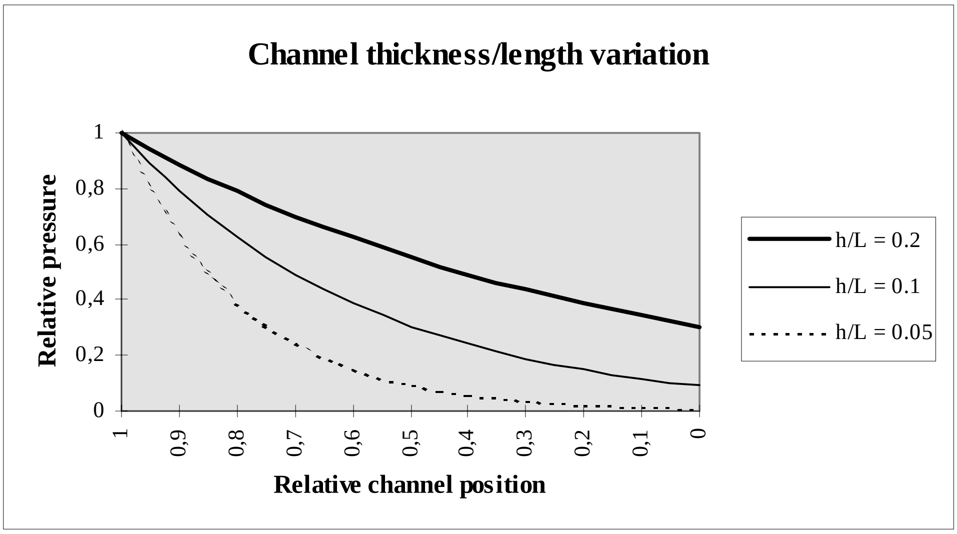

Figure 43. Relative pressure as a function of relative position in the channel, 0 is the outlet.

Numerical comparisons to find the effect of the slope angle are given in Figure 44. Combinations of channel length / thickness ratio and coefficient k are selected to give meaningful pressure values. It is found that a small slope angle has a very clear effect. When the angle grows larger, the pressure has already dropped to a low level regardless of the value of the slope angle.

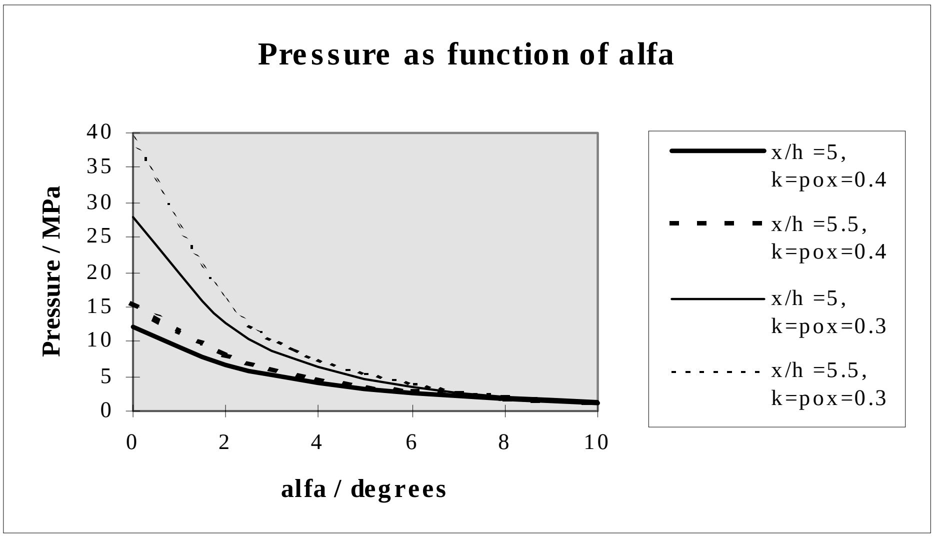

Figure 44. Pressure at x = L (Equation 47) as a function of slope angle α, channel length / thickness ratio and coefficient k as parameters.

An analysis performed for the present work has shown that inertia forces would have negligible importance for the pressure distribution in the case where parallel walls approach each other. This can be expected based on the similar result in the viscous model.

5.3.2 Discussion

As mentioned, the Savage et al. (1992) model makes it possible also to handle curved planes and it would as such thus be better suited to solving the propeller case, rather than the simpler models. The distance from the leading edge to the peak pressure location is rather short. The granular models all give an exponential form of pressure distribution. The peak pressure is governed by the strength of the solid ice and the pressure at the leading edge caused by the confinement due to the ice flakes at the face side of the blade. It is thus actually of minor importance how accurately the performance of the crushed ice at the leading edge is modelled. Regardless, the channel length width proportions in the beginning of each burst phase would in most cases be far from the basic assumption of a long and narrow channel. The channel opens with a rather big angle from the wedge tip towards the leading edge. At that phase the pressure will drop immediately after the peak value at the wedge tip as shown in Figure 44. On the other hand, the pressures start to rise to meaningful values when the channel is narrowing. According to the profile pressure distribution tests the pressure rises from the leading edge towards the peak pressure location close behind the leading edge so steeply that the actual shape of the distribution is not important. An estimate based on the Daley et al. model is therefore considered to roughly model the pressure distribution at the back side towards the leading edge and is applied in subsequent analysis. In the beginning of the extrusion phase when the channel is wide the leading edge pressure is applied for the whole channel between the leading edge and the wedge tip. At the wedge tip the pressure rises very steeply to the value governed by the solid ice strength. The pressure at the outlet of the channel, i.e. the leading edge, is discussed in section 6.2.2 below. At the end of the extrusion phase when the channel narrows and the pressure starts to rise to a critical value at the new wedge tip the parallel wall Equation 45 or 46 is applied.

6 EFFECTIVE LOAD

The elements of the process model, failure of solid ice and extrusion of the crushed ice are used in developing the effective load that is caused by the contact. Some engineering type assumptions are necessary to be able to perform numerical calculations. The effective load is based mainly on the back side pressure distribution. The pressures at the leading edge and the tangential point of contact are defined separately. A small load component at the face side exists. The pressure here is estimated as a linear distribution from the leading edge value to zero at a point where the contact is lost at the face side. This point in turn, is defined from the leading edge load required to create a spall at the face side. When the whole blade load is integrated from individual section loads some three-dimensionality corrections must be made at the blade tip and the sections in contact with the ice block edge, as discussed in section 3.3.

6.1 BACK SIDE PRESSURE DISTRIBUTION

The available results from the massive ice cases of the profile pressure distribution tests do not give a clear indication of the size of the spalls and accordingly wedge geometry. The length of the first back side spall that opens to the ice edge created by the leading edge crack can be determined from the peak pressure frequency of the first sensor behind the leading edge. However, the remaining spalls that are required to open the channel between the first spall and the solid ice that is left over after the blade pass may be a few small ones or just one or two bigger ones, Figure 45. The actual geometry will depend on the grain borders and the steepness of the pressure peak. The length to width ratio of a spall is, however, quite constant, Figure 33. This supports the scenario of rather small spalls, similar in size to the first spall, and having widths of one or two grain diameters. The geometry of the solid ice wall in the direction in which the profile is proceeding is also somewhat speculative. In the slip surface approach that is applied, the angle between the channel wall that is against solid ice and the angle of attack line, Figure 45, is the angle ψ defined by the Mohr-Coulomb condition, Equation 5. The rest of the channel wall can be idealised as maintaining the same direction up to the wall in the angle of attack direction or as following the profile geometry fairly tightly.

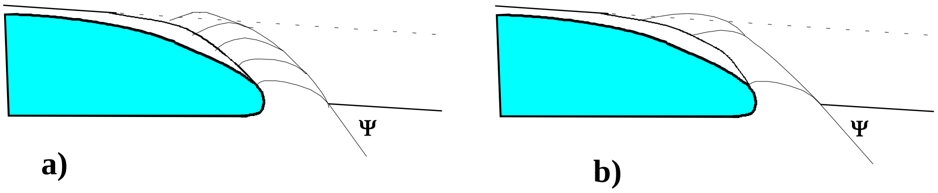

Figure 45. A scenario of many small spalls a) and a few big ones b).

The viscous model according to Equation 37 is applied for the flow towards trailing edge from the instantaneous watershed at the narrowest point of the channel. The granular model is applied for the flow from the watershed towards the leading edge. Two phases of the granular model are distinguished as discussed in section 5.3 - a diverging channel with very low pressure along the channel and a channel with more or less parallel walls (Equation 47 or 46) just before the formation of a new spall. The definitions of various parts of the channel are given in Figure 46.

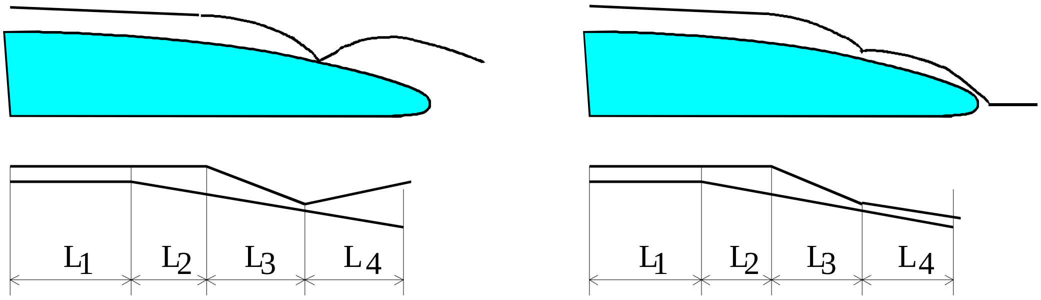

Figure 46. The definitions of channel parts: L_1 the parallel walled section, L_2 the converging section, L_3 the diverging section and L_4 the section of extrusion towards leading edge.

Examples of relative pressure distributions along the channel are given in Figure 47 for different phases of the process, i.e. different relative lengths of channel parts. The relative channel thickness / total length ratio and the geometry of the converging and diverging channel parts in the example are roughly based on observations of the massive ice test cases in the profile pressure distribution tests. The shape of the pressure distribution on the viscous part of the channel is somewhat less peaky if the channel thickness / length ratio is larger and the value of the apparent viscosity accordingly larger in order to reach the same maximum pressure value. The numerical values that are used in the example are $\mu = 1 \times 10^{-4}$ MPa s, U = 8 m/s, V = 1 m/s, $\beta = 8°$, a channel total length of 80 mm, a channel thickness at the tangential point of the contact of 5 mm and the pressure peak heights of 15 MPa. An uniform pressure for the parallel walled section L_1 is applied for all phases in this example. If the contact (i.e. channel) length is 450 mm, with the same relative blade geometry and the same apparent viscosity, the same peak pressure would require a channel thickness of 10 mm at the tangential point of contact.

a)

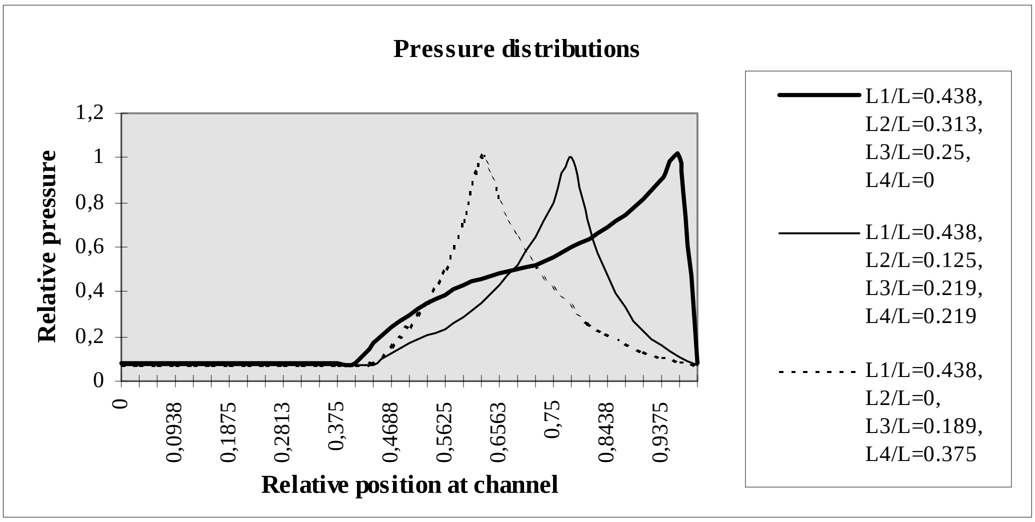

b)

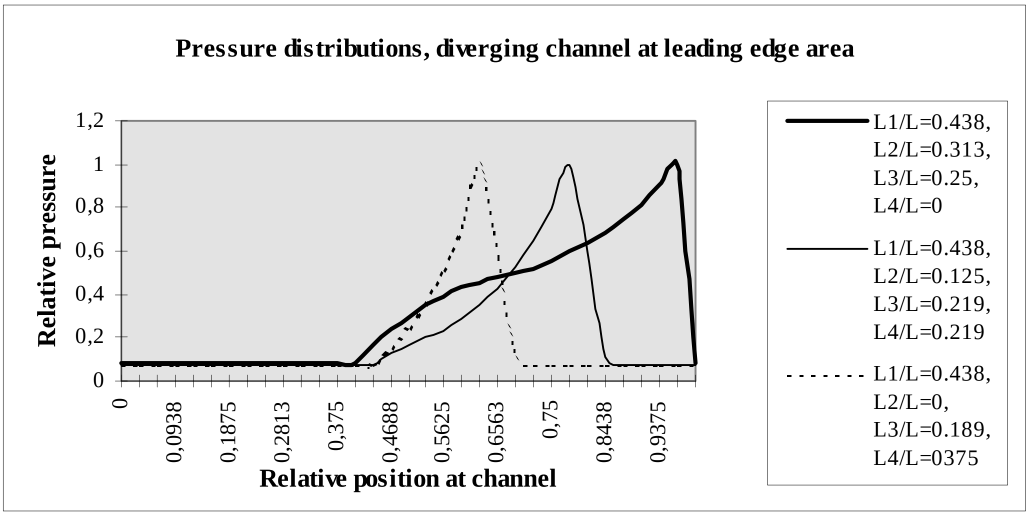

Figure 47. Schematic instantaneous pressure distribution for three different positions of the watershed along the channel; a) parallel walls at the leading edge, b) diverging walls at the leading edge. The relative pressure at the outlet is at both channel ends 0.07.

6.2 CHANNEL OUTLETS AND FACE SIDE

6.2.1 Pressure at the tangential point of contact

The pressure at the trailing edge outlet of the channel was discussed in section 5.2.2. The physical reasoning for it differing from 0 can be explained using the following three scenarios. Probably all of them affect the result.

1) It is possible that there is a net mass flow at the tangential contact point, depending on the conditions close to the wedge tip, regardless of the fact that the blade proceeds and makes room for the extruded crushed ice, as discussed in section 5.1. The “extra” mass of crushed ice must be extruded through the narrow slot between the blade and the channel instead of a free half space. Applying impulse and momentum theory gives quite low pressures.
2) There is a small angle between the angle of attack and the profile tangential direction even close to the outlet point. This angle causes the viscous pressure to rise slightly from the actual outlet value to some higher value towards the leading edge. A pressure distribution can be calculated by applying Equation 37.
3) The small angle close to the outlet causes some additional compaction of the sintered ice. Applying an elastic modulus 45 MPa for the crushed ice, according to Singh et al. (1993) would result in a pressure in the order of 1 MPa.

As stated already in section 5.2.2 the absolute value of the back pressure is of minor importance to the result of the pressure distribution. 1 MPa is selected for the effective load calculations.

6.2.2 Pressure at the face side and leading edge

It may be argued that the leading edge geometry has some effect on the leading edge pressure. This can be studied qualitatively using the Hertz theory of elastic contact. The profile-wise force required to produce pressure of a certain level at the leading edge is proportional to the radius of the leading edge. However, the critical stress state needed for a failure with this contact geometry depends only on the ice parameters and the contact pressure. It does not depend on the actual radius of the cylinder. Thus the critical leading edge pressure is independent of the leading edge radius provided that the radius is not smaller than a typical grain diameter. In that case the load is of a point load nature. When the critical stress state is exceeded the leading edge can proceed into the ice, form a tensile stress distribution and open a tensile crack.

The loading geometry of the leading edge can be approximated with a circle which penetrates into the material, see Figure 48. The geometry is either the actual profile geometry or a "virtual" geometry taking into account the crushed and partially consolidated layer of ice around the leading edge. Replacing the distributed load around the leading edge with the resultant force and applying de Saint-Venant theory gives the schematic principal stress direction trajectories of Figure 48. Some distance away from the load point, (corresponding to 0.5 - 1.0 w, cut width, Figure 48) setting the stress direction parallel to the ice edge is a good approximation. If a later stage of the process is considered, when the leading edge meets the solid ice at an edge formed by the previous spall, a radial distribution of the principal stress directions is a better approximation. Close to the leading edge, if the actual load distribution is taken into account, there is a zone of tensile stresses normal to the direction of the profile. The depth of this zone varies according to the penetration depth and radius of the leading edge.

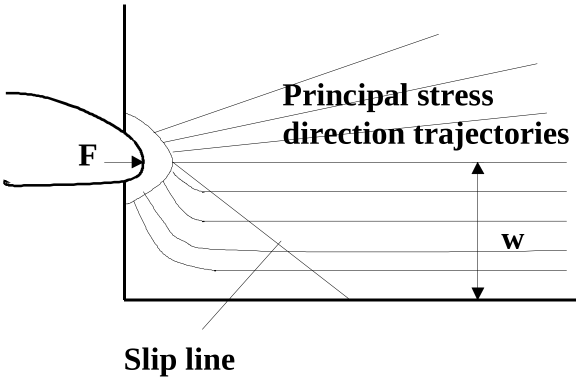

Figure 48. The schematic principal stress distribution when the leading edge penetrates into ice.

The global load required for a spall to open at the face side is clearly directly proportional to the cut width at the zone of parallel principal stress directions when slip surface theory is applied to the load. Increasing confinement due to increasing cut width also affects the critical load required to cause the failure. A load dependence (registered as pressure dependence) on the cut width was found in the profile pressure distribution tests, as described in section 2.3.4.

The global load is transformed to a leading edge and face side pressure by means of the actual contact length. A uniform stress distribution is assumed in the beginning of the process and the constraining stress due to the plane strain condition is neglected. If the cut width is large the contact length must grow beyond the actual leading edge since the local pressure at the leading edge cannot exceed some value that causes local spalling and crushing. In the case of a small angle of attack the contact length would, however, have to grow unproportionally in order to produce the required load in the profile direction. Therefore, it is logical to assume that once the crack has opened, the additional contact length along the actual face side produces a load component mainly normal to the profile direction that continues opening the crack by bending stresses.

The contact length is calibrated with the measured test results, with the pressure as a function of the cut width and the geometry of the leading edge. The required contact length b_1 along the arc of the leading edge (producing the load component in the profile direction) is

$$b_1 = 0.055w \tag{48}$$

where w is the cut width in mm. If a longer contact is required to produce the critical load (the load component normal to the angle of attack direction) the additional contact length b_2 along the face side to be added to the arc length is

$$b_2 = 0.094(w - w_{b1}) / \sin\gamma \tag{49}$$

where w_{b1} corresponds to the maximum cut width thickness based on the load in the profile direction and the angle γ is the angle between the normal of the face side and the angle of attack direction. The minimum value of γ is 45°. These contact length formulas are developed from the maximum load case but they are applied also to the mean load. The pressure is assumed to be linearly distributed from the leading edge value to the point of loss of contact.

The mean pressure at the leading edge was found from the time histories of the profile pressure distribution tests to be formed from the peak values and a constant level of pressure between the peaks. Also the mean pressure had a clear dependence on the cut width, see Figure 23. The cut width dependence on the mean pressure, and specifically on the uniform pressure value between the peaks, can be explained by the constraint due to ice flakes that have been cracked loose at the pressure side. However, applying the momentum and impulse theory leads, for the extruded crushed ice, to velocity requirements that are about twice those observed to be able to produce the observed pressure levels.

Based directly on the test results for the vertical grain direction the mean pressure at the leading edge follows the formula

$$p_{LE} = 1 + 26w \tag{50}$$

where w is the cut width (m) and p_{LE} the mean pressure (MPa).

The effect of grain direction on the leading edge pressure was clear in the tests, section 2.3.4. The tensile stress acted along the grains in the horizontal grain orientation case, whereas in the vertical grain orientation case, the tensile stress acted across grain boundaries. The pressure value did not drop between the peaks in the horizontal grain tests as much as in the case of vertical grains. It is possible that after the leading edge has cut the grains loose, some kind of gliding of individual grains against each other takes place. The measurements were performed only with one cut width. The same cut width dependence as for vertical grains is applied, however, and the mean pressure is given the value

$$p_{LE} = 4.5 + 26w \tag{51}$$

where w is the cut width (m) and p_{LE} the mean pressure (MPa).

Since the grain orientation can vary in natural propeller ice conditions, the higher value for the leading edge load, Equation 51, is used as a conservative approach in the effective load calculations. The pressure value is limited to the highest average pressure value on the back side. In practice it means that the leading edge pressure stays constant beyond some 0.3 m cut width.

6.3 THE COMBINED LOAD

The effective load on each section is the time average of instantaneous pressure distributions during the process. A simplified method to calculate the effective pressure distribution of the process along the section is developed. The simplified method is needed as input in the overall simulation model, section 1, that is used in verifying the method with some full-scale observations. A full simulation of the process along each section, as developed above, would be too tedious a task for each time increment in the overall simulation model. The full process simulation along the section would of course be a more correct way to find out the effect of various geometric parameters of the crushed ice channel compared to the simplified method. However, as described above, the viscosity and maximum pressure are not known very accurately. Therefore it is considered best to also use a simplified method in some parameter studies.

The length of each spall is roughly the same, as the width of the loaded surface is assumed to be the same amount of grain diameters. The critical peak pressure does not vary a lot as a function of the wedge opening angle, section 4.3.4. As the blade glides in respect to the solid ice the location of a peak pressure that is associated with a wedge tip moves along the blade towards the trailing edge until the failure pressure is reached, Figure 49. The x-axis in the figure is fixed to the blade, x = 0 being at the leading edge. When spall 2 is formed the location of the peak pressure jumps from x_1 to x_2. The blade glides further and the pressure rises when the clearance at the blade tip decreases. When the pressure peak has reached the location x_3 a new spall, 3, will form.

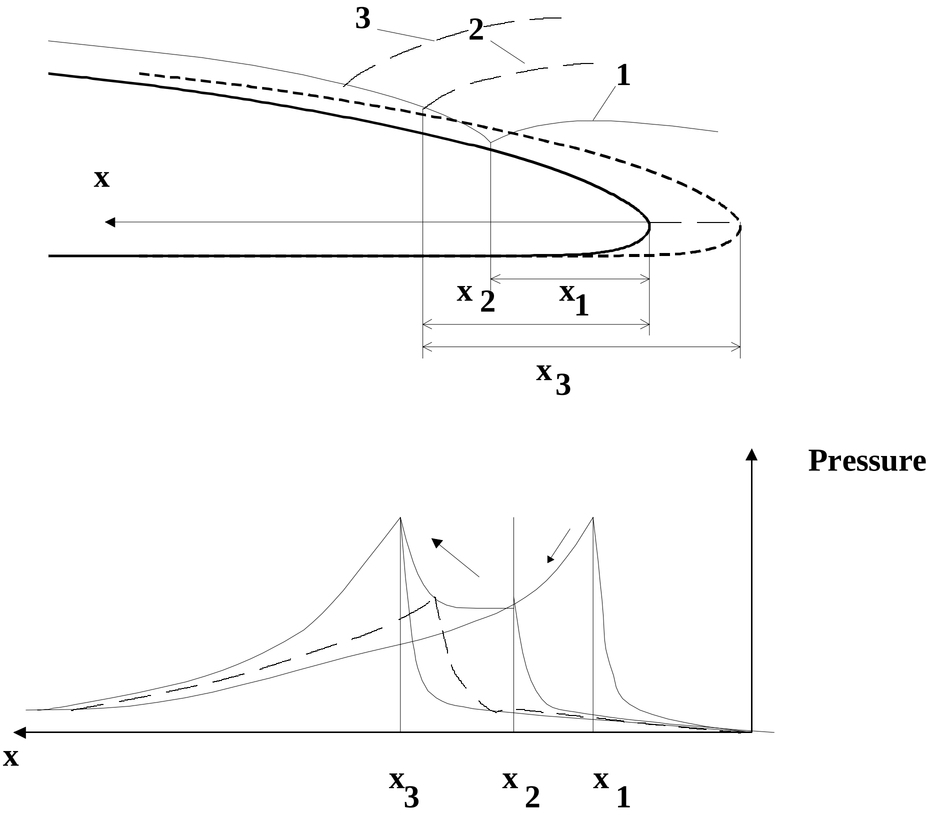

Figure 49. The location of the peak pressure along the blade when the blade glides aside a wedge tip.

The number of wedge tips, and instantaneous pressure peaks, during one cycle of the process is defined as the channel wall length L´, Figure 50 (within the channel part L_3 in Figure 45) divided by the grain diameter (two grain diameters could also be selected). This is considered to be valid for both vertical and horizontal grain orientations. The total average pressure distribution along the blade is the sum of the average pressure distribution associated with each wedge tip during its existence divided by the number of wedge tips. The average pressure at a wedge tip during its existence is defined based on the test results. The average pressure ratio was found to be 1.2 when the strength ratio was 2. This ratio for thin ice is applied for the massive ice as well, although the extrusion and spalling phenomena are different in massive ice and thin ice cases. The maximum value p_{MA} of the average pressure distribution is defined as

$$p_{MA} = 10\sigma^{0.3} \tag{52}$$

where σ is the uniaxial compressive strength of the solid ice. Equation 52 is in agreement with the observations of the massive ice case. The measured compressive strength in the across grain direction was 3.1 MPa. Applying the factor 0.65 as discussed in section 4.3.3 gives a value of 2.0 MPa for σ. p_{MA} is thus 12.3 MPa. The average value along the blade for the whole area of high pressure is assumed to be 10 MPa as discussed in section 4.3.4. p_{MA}

represents the maximum value of the average pressure distribution and is thus of the right level when compared with the 10 MPa.

p_{MA} is defined to be 0.9 times the average pressure at a wedge tip p_{WA} during its existence. This will give for p_{WA}:

$$p_{WA} = 11.1\sigma^{0.3} \tag{53}$$

Taking into account Equation 21, the average pressure will be

$$p_{WA} = 2.866(p_{\max})^{1/2} \tag{54}$$

The distance along the blade between the peaks, representing the average pressure associated at each wedge tip will be (Figure 50)

$$l_1 + l_2 = \frac{d\sin\psi}{\tan\beta} \tag{55}$$

where

l_1	is the distance between wedge tips in fixed coordinates
l_2	is the distance that the blade has to proceed after the formation of a wedge tip in order to be in the same relative position to the new wedge tip as it was to the previous tip during the previous phase
d	is the grain diameter
ψ	is the angle between the angle of attack line and the solid ice wall
β	is the angle between the angle of attack line and the profile tangent direction.

The calculation of the total average pressure is valid if the angle between the solid ice wall and the profile is assumed to be constant, Figure 50. In fact, the angle $\psi - \beta$ increases when moving from the leading edge area towards the trailing edge, at locations within L_2 close to L_1 in Figure 45. This can be compensated for by assigning a weight factor for the pressure distributions that are associated with wedges in this area. The pressure between the peak pressures and the channel end pressures is represented with a linear distribution in this simplified approach. The pressure in the whole parallel walled channel portion is simplified as constant. In reality the pressure rise here would vary as discussed in section 5.2.2 and affect the height of the pressures used here as a channel end pressure for individual pressure lines associated with each wedge tip. This would happen especially if the contact length is great. In this situation, however, the channel thickness h would also grow because otherwise the peak pressures at wedge tips would grow higher than what is required for the solid ice to fail. This would balance somewhat the effect of long channels. The end result of the shape of the total average pressure might be influenced slightly, but taking into account all the other uncertainties the simplification of uniform pressure within the parallel walled part of the channel is considered to be justified. All average wedge tip pressures are given the same value. The length l of a spall is assumed to be 3d according to Figure 33. When the blade has proceeded the distance l and reached the line II in Figure 50, a wedge tip is again formed at the leading edge and the pressure here again rises to the average wedge tip pressure. This high pressure from line II is now extended to the wedge tip at the intersection of the blade profile and line I. When the process continues, this high pressure zone shifts one wedge tip distance by the wedge tip towards the trailing edge. If the contact is long and $\psi - \beta$ relatively large, the high pressure zone shifts once more to the leading edge. This approach of an even high pressure zone is of course theoretical and may overestimate somewhat the actual average distribution.

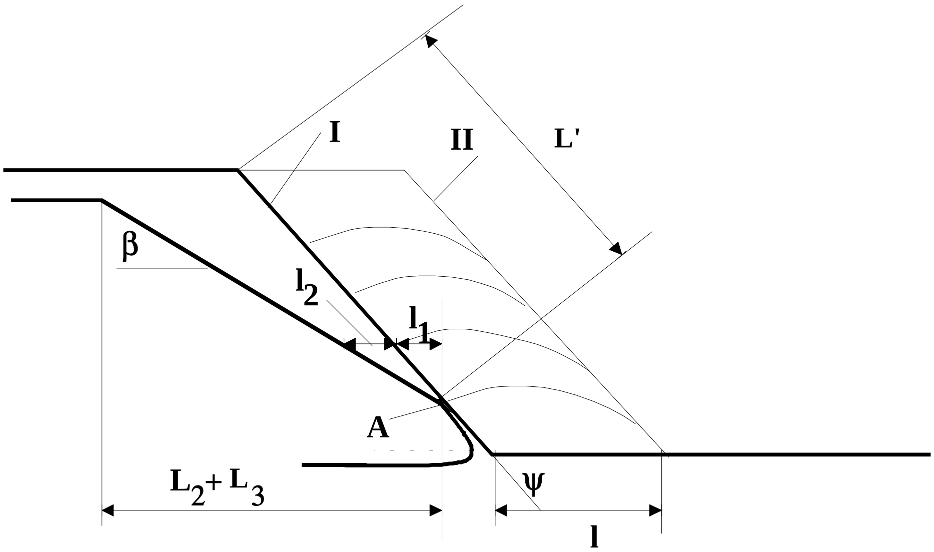

Figure 50. Definitions of the channel geometry that are used in the simplified effective pressure distribution calculation.

An example of a pressure distribution calculation is given in Figure 51. The example is for a case of $\psi = 27.5\ ^o$, $\beta = 15\ ^o$, L_2+L_3 = 100 mm, d = 5mm, p_{WA} for each wedge tip = 15 MPa and p_A = 5 MPa (after the formation of the first spall at point A when also P_A is 15 MPa).

A parametric study of the effects of various geometric assumptions on the pressure distribution shape was performed. The proportions of the pressure distribution are best defined, as shown in Figure 52, by the maximum value of the average pressure p_{MA}, the location of this maximum along the blade X, the pressure value p_0 at the first point of calculation A (Figure 50) and the pressure value p_L at the end of $L_2 + L_3$ = AD. An even pressure value is used as an approximation in the whole parallel walled channel portion, L_4 = ED.

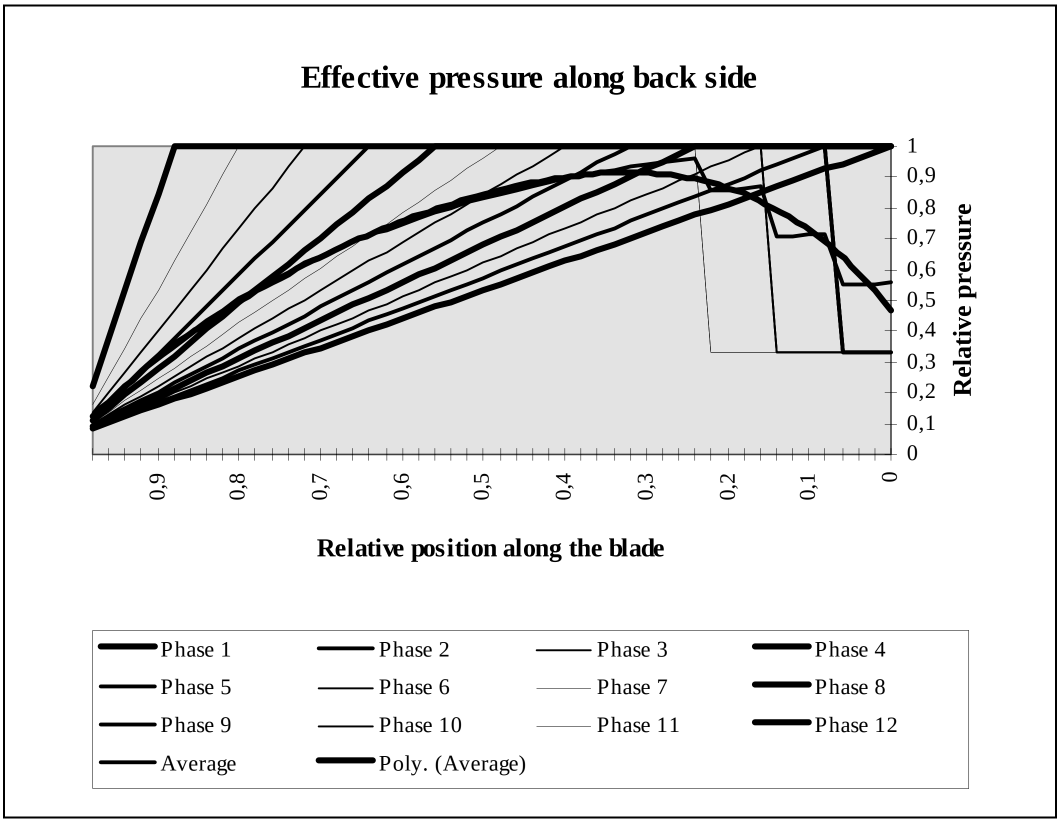

Figure 51. An example of the effective pressure distribution calculation. (The average pressure is smoothed by a 4th order polynom).

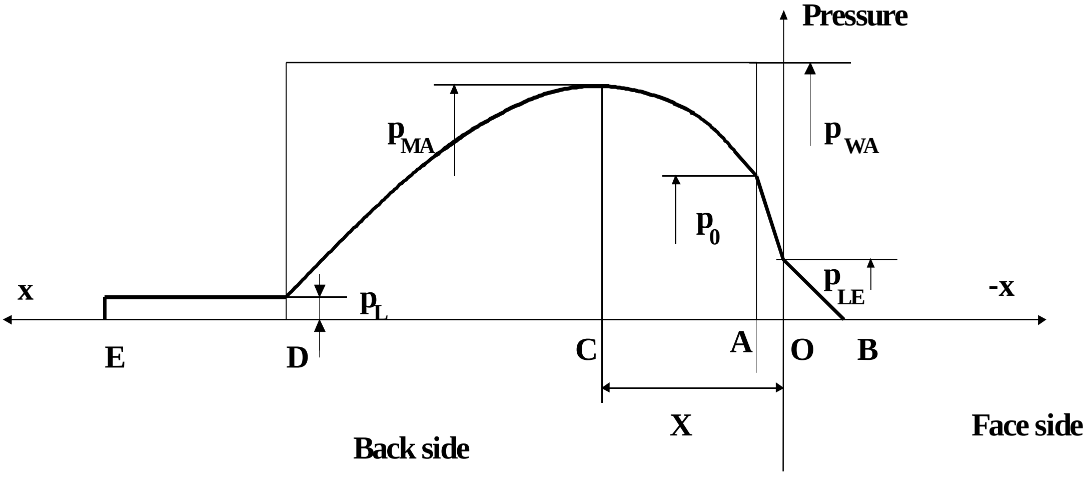

Figure 52. The definition points of the pressure distribution shape.

It appears that the relevant parameters for the values of the definition points are the angle $\psi - \beta$ (Figure 50), the length of the contact, made dimensionless by dividing it with the grain diameter, L/d and the ratio of mean leading edge pressure to the average wedge tip pressure p_{LE} / p_{WA}. The dependencies all are linear enough for application of linear correlations.

p_{MA} / p_{WA} varies in the range of 0.8 to 1.0 with variation of relevant parameters. Bearing in mind the uncertanties in defining the proper value for p_{WA}, a fixed value of 0.9 for p_{MA} / p_{WA} is used as already defined for Equation 53.

The position of the maximum p_{MA} of the average pressure distribution depends relatively strongly on the ratio p_{LE} / p_{WA} and somewhat on the length of the contact. The following formula is applied:

$$AC / AD = (1.18 - 0.018\frac{d}{AD}) \times (0.55 - 0.41\frac{p_{LE}}{p_{WA}}) \qquad (56)$$

p_0/p_{WA} depends mostly on the ratio p_{LE} / p_{WA} and to some degree on $\psi - \beta$. A formula in the $\psi - \beta$ range 15^o - 20^o, is applied:

$$p_0 / p_{WA} = 0.54 + 0.33\frac{p_{LE}}{p_{WA}} \qquad (57)$$

The effective load at the back side between the definition points is given as a second order curve:

$$p = p_{MA} - \left(\frac{p_{MA} - p_0}{(X - AO)^2}\right)(X - x)^2 \qquad (58)$$

in the range from A to C, and

$$p = p_{MA} - \left(\frac{p_{MA} - p_L}{(AD + AO - X)^2}\right)(x - X)^2 \qquad (59)$$

in the range from C to D. An even value of 1 MPa for the pressure between point D and E, where the contact is lost, is used according to section 6.2.1. Point D is defined to be at a location where the angle between the local tangent along the profile and the angle of attack direction is 3^o. Point A is defined to be at a location where the angle between the local tangent along the profile and the angle of attack direction is 25^o. Equation 51 is used to calculate the pressure p_{LE} at the leading edge and Equations 48 and 49 used to define the point B. A linear distribution is applied between points A, O and B.

6.4 DISCONTINUITY ZONES

An engineering type of approach is used for the three-dimensionality corrections at the discontinuity zones.

6.4.1 Tip radius area

The radial cracking model of the back side was considered to be applicable also for the face side tip area cracking in section 3.3.2.

For practical use of the tip radius pressure, a linear dependence on the angle of attack is applied between 0 - 5°, while for bigger angles a constant pressure is applied. The model is used for radia between 0.97R - 1.0R. The pressure distribution is applied as uniform pressure for this tip section. The pressure that is required for a spall to form is calculated directly from Equation 2, assuming no stress in the minor principal stress direction. The effective mean value of the pressure is taken into account using a factor of 0.6:

$$p = 0.6\frac{\alpha_A}{5}\left(\frac{2c\cos\phi}{1-\sin\phi}\right), \quad \text{when } \alpha_A < 5^{\text{o}} \qquad (60)$$

$$p = 0.6\left(\frac{2c\cos\phi}{1-\sin\phi}\right), \quad \text{when } \alpha_A > 5^{\text{o}} \qquad (61)$$

where α_A, the angle of attack is given in degrees, ϕ is the internal friction angle and c is the cohesion.

If the cut width is so small that part of the section does not face any ice at the face side, the pressure naturally has to be applied only to the part that is in contact with ice.

6.4.2 Ice edge areas

The criterion for the change of extrusion mode, i.e. of profile-wise to radial, at the hub radia is defined as follows. The distance from the middle of the contact along the profile to the free ice edge in the radial direction h must be shorter than the distance along the profile to the tangential point of contact, for the extrusion to take place in the radial direction. A simplification of the radial pressure distribution, compared to the observations from the profile pressure distribution tests, is applied in the effective load model, Figure 53. The same reduction is applied for the leading edge pressure.

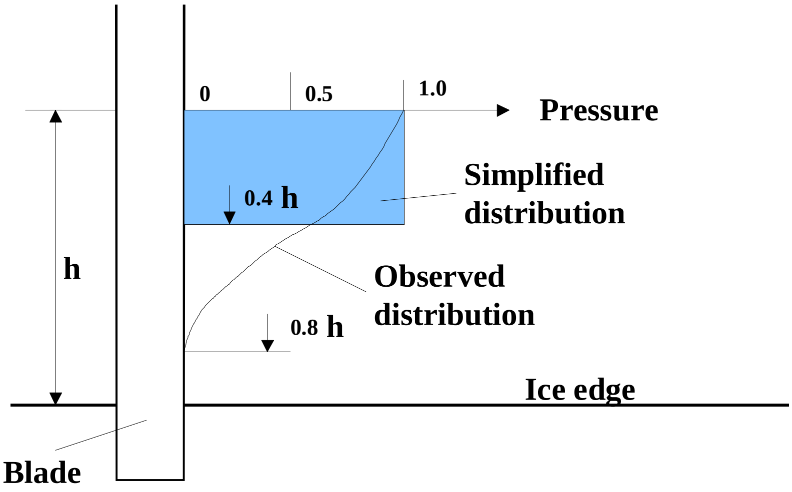

Figure 53. *The radial pressure distribution in the case of radial extrusion towards the free ice edge. Pressure 1 is the profilewise pressure.*

7 VALIDATION

7.1 THE PROFILE PRESSURE DISTRIBUTION EXPERIMENTS

The massive ice test case was studied. The situation is illustrated in Figure 54. The grain layers are shown schematically. The channel thickness h at the tangential point of contact, (5 mm), the first spall length, (15 mm) and the grain diameters, (5 mm) are based on the test observations. The spall length / width ratio is based on the model developed in section 4. The total contact length is 80 mm, but the length of the high pressure area AD ($=L_2 + L_3$) is 30 mm. The applied β-angle is 10^o, ϕ-angle is 35^o and ψ-angle is accordingly 27.5^o. The approximation of zero pressure rise in the parallel walled portion of the channel is based on the fact that the maximum H value, as defined in Figure 37, is roughly the same as h.

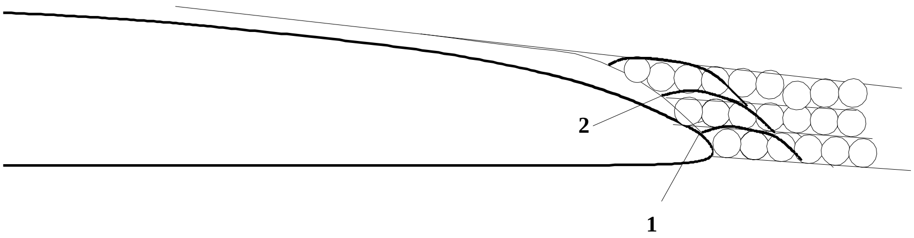

Figure 54. The schematic spalling sequence of the massive ice case in the profile pressure distribution test.

The result of a direct calculation of the failure process is shown in Figure 55 for the high pressure area on the back side. Equation 37 is applied for pressures from the wedge tip towards the trailing edge and a uniform pressure having the value of the leading edge pressure is used for pressures towards the leading edge according to section 5.3.2. The blade proceeds 2 mm between each phase. The uniaxial compressive strength is taken as 2.0 MPa as according to section 4.3.3. The experimental result of 10 MPa for the peak pressure and 5 MPa for the average pressure is used at the wedge tip 1 in Figure 54, corresponding to point A in Figure 52. 22.7 MPa, as determined by Equation 21, is used as the peak pressure at wedge tip 2 in Figure 54. The apparent viscosity is given the value 0.0003 MPa s.

The approximate effective load calculation method that is developed in section 6 (Equations 50 - 59) gives for the high pressure area on the back side the result shown in Figure 56. This distribution is used for the whole effective load of the blade shown in Figure 57.

The loads of Figure 55 and 56 result in an effective load that is 1.45 - 1.62 times the load achieved by directly using the pressure measurements of the massive ice test cases for the whole tool area that is in contact with ice. This is in agreement with the average coefficient 1.39 of the two test cases, section 2.3.3. The resultant force of the transverse load occurs at a distance of 23 mm from the leading edge, compared to the measured value of 20 mm, section 2.3.3.

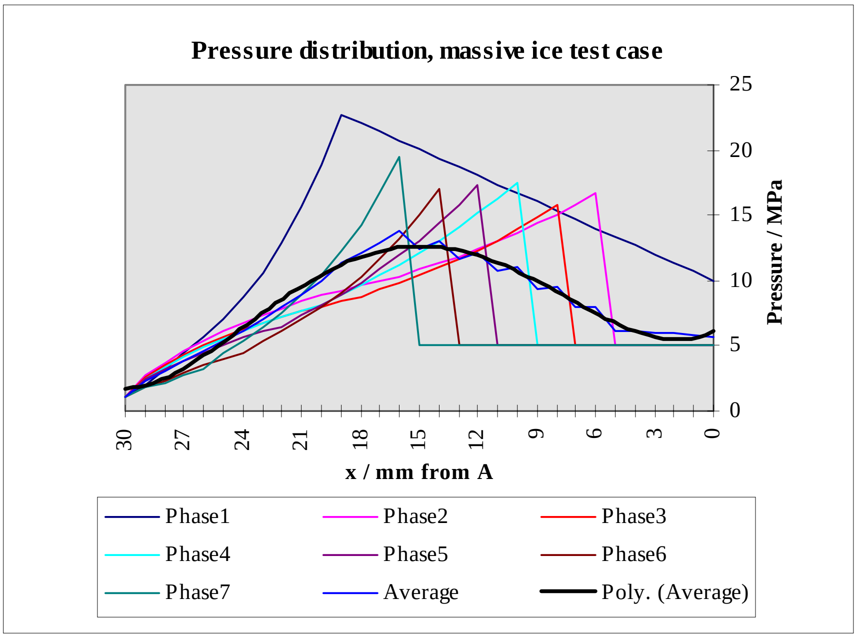

Figure 55. Effective pressure distribution at the high pressure area of the back side of the test tool, (direct calculations of the process). The average distribution is smoothed with a 4th order polynomial.

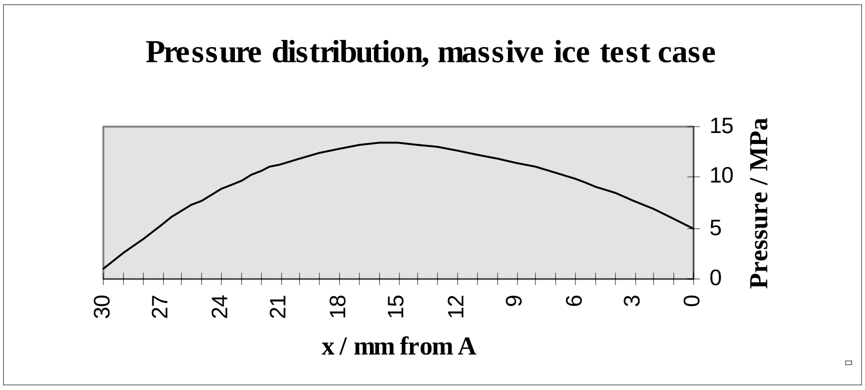

Figure 56. Effective pressure distribution at the high pressure area of the back side of the test tool, (approximate method).

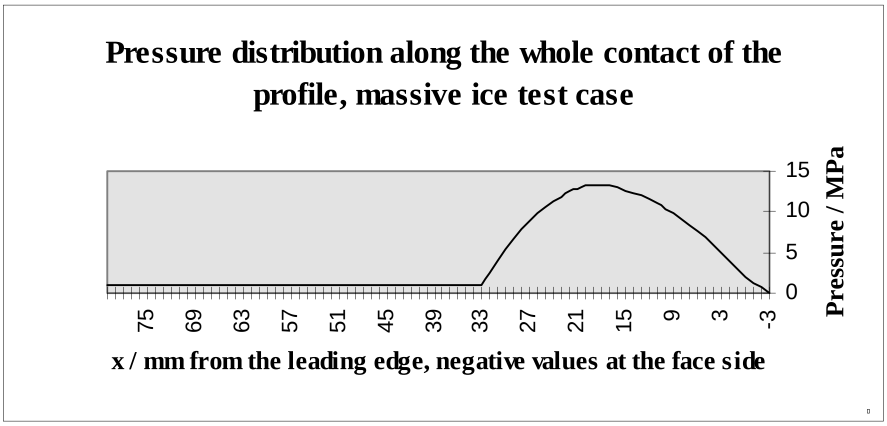

Figure 57. The effective pressure distribution along the tool (using the Figure 56 distribution).

7.2 THE M/S GUDINGEN FULL-SCALE TESTS

7.2.1 Integrated load from section-wise effective loads

The validity of the model is checked against blade moments as functions of the angle of attack as observed from full-scale measurements performed with M/S Gudingen, Koskinen and Jussila (1991). The total effective load is calculated as the sum of the section loads with a 0.05R distribution. The full scale data includes the effects of dynamics between the blade and ice block and the hydrodynamic disturbance loads. These have not been considered in the integrated load calculations. The calculation corresponds to an ice block with infinite mass. The comparison to the full-scale results is thus only indicative. The input parameters for the calculations are

- propeller diameter 2 m, hub diameter 0.72 m, profile geometry according to M/S Gudingen
- propeller speed 6.3 RPS
- propeller pitch 12.5° at 0.7 R radius
- apparent angle of attack adjusted with ship speed
- profile speed calculated for each section
- full ice immersion from tip to hub sections
- ice strength 2.6 MPa.

The leading edge and face side pressure for each propeller section as well as the tip load and reduction at the ice edge are included according to section 6. The full-scale data points are the maximum backwards bending blade moments observed during each measurement period (i.e. each trip lasting a few hours) during the whole season. The manoeuvring situations and negative angles of attack are removed from the data. The results are shown in Figure 58. The calculated points fall within the majority of the measured points for the larger angles of attack whereas at very small angles of attack the calculation corresponds better to the measured extreme values. The effect of ice strength on the calculated values would be small especially for larger angles of attack. The discrepancy between the calculated and highest full-scale data points can rise either from the model or the interpretation of the full-scale data. At larger angles of attack the contact length of each section is quite short and clearly larger calculated bending moments would require a considerably higher pressure, the actual shape of the distribution being of minor importance. The tip load that bends the blade forward is not yet fully effective while the maximum contact area bending the blade backwards is developed in a fairly early stage of the milling process. The concept of an apparent angle of attack may be misleading for the interpretation of exceptionally large measured blade bending moments, forming the envelope. The ship is known to have had a big rudder angle when the envelope data points of 3° and 6° were registered. The ice block may have been in rotational movement during some of the contact events. During the calibrations of the measurement system before the full-scale tests the blade was clearly observed to bend and change pitch slightly. All this could easily affect the actual angle of attack by a few degrees and increase the contact length at back side sections accordingly. The calculated bending moment at zero angle of attack is higher than the measured maximum. The angles of attack may be the same for both calculated and measured points but the actual ice block size in the measured point is, on the other hand, not known.

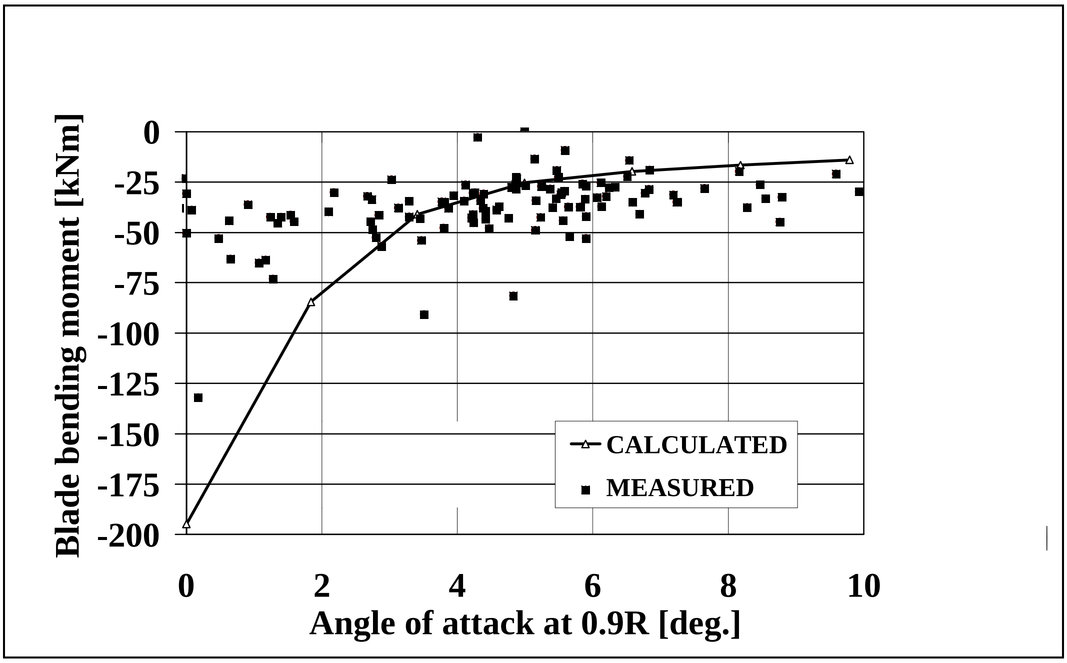

Figure 58. The M/S Gudingen blade moment as a function of the angle of attack.

7.2.2 The effective load applied in the overall dynamic simulation model

A Gudingen full-scale event that is known to have occurred for a massive ice block was studied. The dynamic effects are thus minimised. An overall simulation model as described in Section 1, was used to validate the effective load distribution developed in section 6. Jussila’s simulation model is used here and presented briefly by Koskinen et al. (1996). The model handles the loads on a time scale. The calculations proceed step by step with a time increment. The contact area and accordingly contact load and the velocity conditions of the ice block are developed within each time step. The physical model is based on the equilibrium of the forces that are acting on the system. The principal laws of mechanics, the law of motion and the law of action and reaction are used. The non-contact load that is used in the simulation model is also presented by Koskinen et al. (1996). It is based on model tests performed at IMD in the context of the JRPA # 6 project. The pressure drop at the leading edge on the back side depends on the blockage percentage, propeller advance and rotational speed, diameter, angle of attack of the section and radius of the section. The pressure distribution is assumed to drop linearly from the leading edge to the point at 0.5 of the chord length where the trailing edge value is applied. The trailing edge value is taken as one fifth of the leading edge value.

The combined effective load as developed in section 6.3 is used in the simulation model. The effects of the tip load, and the load reduction at the ice edge are included according to section 6.4.

The simulated case corresponds to the Gudingen propeller (D = 2.0 m, d_{hub} = 0.72 m, Z = 4, EAR = 0.686). The propeller speed during the observed event was 6.3 rps, ship speed 5.5 m/s, and pitch angle at 0.7R 12.5°. The apparent angle of attack is thus 2.5° at 0.7R radius. The ice compressive strength was 2.6 MPa. This situation corresponds with the maximum measured event of backwards blade bending load. The mass of the ice block is varied in the calculations from 1000 kg to 4000 kg, with shape proportions 1:2:3. The resulting maximum bending load at the impact of the first blade is given in Table 7 as a function of the ice mass.

Table 7. Blade force as function of ice block mass.

Ice block mass	1000 kg	2000 kg	3000 kg	4000 kg
Max. blade bending force	270 kN	350 kN	400 kN	440 kN

The results mean that a contact with a relatively small ice block, 0.7 x 1.4 x 2.1 m^3, is enough to cause a high load. The measured maximum force was 325 kN (note that there are certain indications that the limits of the measurement range was reached and the measured force might actually be somewhat higher). The simulation model also gives the values of spindle

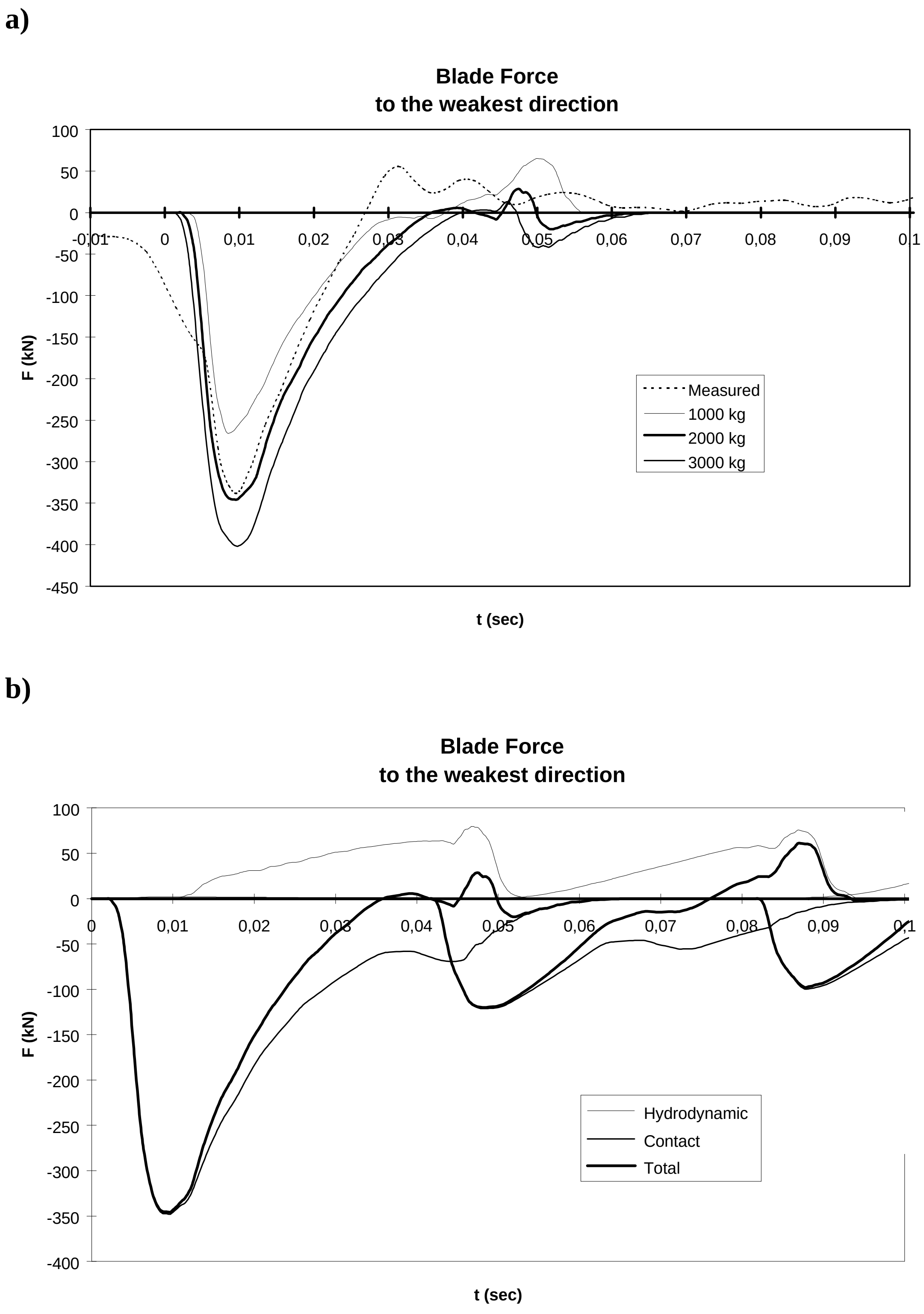

Figure 59. a) Simulated time histories of MS Gudingen blade ice forces (ice block mass as parameter) together with the measured time history of the same event (Koskinen et al. 1996). b) The 2000 kg simulation of the same case showing the various load components.

torque and shaft torque but these are not compared to the measured ones because the blade bending load in the weakest direction is the primary load that is caused by the effective load of section 6.3. The time histories of the simulated blade bending force for various ice block masses are shown in Figure 59 a together with the measured bending force. The simulations and the measured bending force are presented for just one blade in contact with ice. The components of the simulated load are shown for the 2000 kg block mass case in Figure 59 b. The curves here also show the loads of the second and third blade coming into contact with the ice block.

8 CONCLUSIONS

A process model of the contact phenomena of a propeller blade penetrating an ice block has been developed in this work. The model describes the formation of actual contact loads. The hydrodynamic disturbance loads, i.e. the non-contact loads, due to the presence of an ice block are left outside the scope of the work. The contact loads are based on the quasistatic contact geometry between the blade and an ice block. Thus also the dynamic effects between the blade and the ice block are left out of the model. Their effect can be taken into account by changing the contact geometry input values for the present model. The model is limited to a milling type of contact, in which the leading edge is in contact with ice. The model is developed for a contact with a massive ice block.

The process model is based mainly on the results of a laboratory test series performed for a propeller blade profile. The global loads and pressure along the profile in a chain of pressure transducers was measured. The conclusions for the contact process are:

> The ice failure and removal as the blade penetrates into the ice is a process including various repeatable phases.
>
> The blade leading edge opens a tensile crack that runs towards the free ice edge at the face side. This limits the contact loads that the face side experiences.
>
> Ice material has to be removed from the back side for the blade to be able to proceed.
>
> In the case of penetration into a massive ice block an even crushed ice layer is left between the blade back side and the solid ice. The solid ice fails by formation of small spalls in the direction of the profile and subsequent crushing within the spall. Some, relatively moderate, confinement due to the pressure of the extrusion of crushed ice can hinder the formation of the spalls and result in the failure taking place as local crushing at pressure peaks. If the ice sheet where the blade penetrates is relatively thin, cracks run from the middle of the contact towards the free ice edges of the sheet. The formed ice flakes are crushed either partially or fully.
>
> The proceeding of the blade extrudes crushed ice from the slot between the blade and the solid ice towards either the leading or trailing edge. Crushed ice that is left over after the pass of the blade is in sintered form. The crushed ice that is extruded ahead of the leading edge to the free space on the face side is in granular powder-like form. The flow from a peak pressure location thus takes place in a granular form towards the leading edge and in a more or less sintered form towards the trailing edge in the regime where the blade

> glides over the locations of previous pressure peaks. In the case of penetration into a thin ice sheet with cracking towards the free ice edges extrusion also takes place in the direction of cracking.
>
> Some distance from the ice edge the pressure distribution is fairly even in the radial direction. In the profile direction the highest pressure is concentrated in the area where most of the removal of material has to take place.

The basic elements of the process model, the failure of solid ice and removal of crushed ice are further studied using some relatively simple spalling and extrusion models giving possible explanations of the physical relationships of the phenomena. The failure of solid ice is modelled with spalling in the profile direction. The stress state to form slip-surfaces and the geometry of the spall created by the slip-surface are described with a macroscopic model using the Mohr-Coulomb failure criterion. In the case of some confinement the failure is assumed to take place by local crushing. The extrusion of crushed ice is modelled with a combination of a granular Mohr-Coulomb model and a viscous model. A viscous model is applied for the extrusion towards the trailing edge from an instantaneous peak pressure located at the wedge tip of solid ice where the clearance between the blade and the solid ice is at its minimum. A granular model is applied for the extrusion towards the leading edge.

The pressure distribution along a profile is developed for a series of time steps in a quasistatic manner. The effective load along a profile is taken as the mean load during the process. The effective load of the whole blade is found by integrating the loads of individual sections along the radius. In order to perform numerical calculations various engineering type assumptions, some of them rather rough, have been necessary. The stress state causing the spall to form at a wedge tip of solid ice is strongly dependent on the confinement around the wedge. A high pressure peak due to local crushing of solid ice is not considered to affect the effective load. The effective load level is indirectly calibrated with the experimental results of the massive ice test case of the laboratory tests. The effective pressure dependence of ice strength is based on the tests using thin ice sheets in which the failure process differs from the massive ice block case. The material constants of the extrusion models are not well known. Some assumptions have been made for the leading edge pressure and tip load. Verification against some full-scale tests show that the blade load is qualitatively correctly modelled as a function of the apparent angle of attack that describes the contact length at the back side. The simulated time history of a blade load event shows relatively good similarity to the measured one, although there are such relatively free parameters as ice strength and ice block size.

The aim of the work as set out in the Introduction was to develop a model that describes the contact process. The model was to be based on accepted physical phenomena and was to be able to give the correct average load level and distribution. It is considered that the aim was reached well qualitatively and relatively well quantitatively. A deeper understanding of the contact process has been reached. The contact process model that was developed for the case of milling contact is the core result of the work. The developed solid ice spalling models and crushed ice extrusion models are simplified descriptions of the physics of the phenomena in the process model. The effective load model is able to give the correct shape of pressure distribution and guidelines for the correct load level. The main shortcoming with the process model is that it has not been possible to clearly distinguish the transition from spalling failure mode to local crushing mode. The pressure distribution along the blade in the case of contact with a massive ice block is indirectly formed from the experimental results using the global load measurements. At large angles of attack, some big loads bending the blade towards the back side have been observed in full-scale. These loads are not modelled well with the present model. There are other effective elements in addition to contact loads - for example hydrodynamic disturbance loads or impact loads on the face side.

It is obvious from the results of this work that there are areas that require further research in order to better understand the propeller-ice contact process. The mechanisms of spall formation versus local ice crushing clearly require more research. The effective load dependence on the ice strength and other ice properties need deeper understanding. The effect of various blade geometries should be studied. The formation of large forward bending loads associated with large angles of attack and / or large cut widths should be studied further.

REFERENCES

Airaksinen, K. 1970. Kokeellinen tutkimus jään säätösiipipotkuriin aiheuttamista kuormituksista mallimittakaavassa (An experimental investigation of ice loads on controllable pitch propeller in model scale.) M.Sc.Thesis. Espoo: Helsinki University of Technology. 35 p. (In Finnish.)

Belyashov, V. A. and Shpakov V.S. 1983. On mechanics of ice crushing by propeller blades. In: Ice mechanics and physics. Moscow: Nauka, Academy of Sciences of the USSR, 1983. Pp. 21 - 29. (Translation.)

Belyashov, V. A. 1993. Method for calculating ice loads encountered by propeller blades. Proceedings, The 12th International Conference on Port and Ocean Engineering under Arctic Conditions (POAC), Hamburg 17 - 20 August 1993. Hamburg: Hamburg Ship Model Basin.Vol. 1. Pp. 359 - 367.

Browne, R.P., Keinonen, A. and Semery, P. 1991. Ice loading on open and ducted propellers. Proceedings, The 1st ISOPE, Edinburgh. Colorado: International Society of Offshore and Polar Engineering. Pp. 562 - 570.

Browne, R.P. and Keinonen, A. 1991. Icebreaker propulsion systems propulsive performance and ice loading for design. Proceedings, The 1st Marine Dynamics Conference, St. John’s, NF, Canada, August 5 - 6, 1991. St. John’s: Institute for Marine Dynamics. Pp. 51 - 57.

Bulat, V., Majid, L. and Goosens, L. 1985. Experimental determination of factors affecting loads imposed on propellers in ice. Transport Canada Publication TP 6812E. 224 p.

Chernuka, M.W., Jategaongar, R.P., Norwood, M.E. and Warner, J.L. 1989. Development of a procedure for predicting propeller-ice interaction forces. Transport Canada Publication TP 9850E. 263 p.

Cocks, A.C.F. 1994. The structure of constitutive laws for the sintering of fine grained materials. Acta Metall. Mater., Vol. 42, No. 7, pp. 2191 - 2210.

Daley C. 1991. Ice edge contact, a brittle failure process model. Thesis for the degree of Doctor in Technology. Helsinki: Acta Polytechnica Scandinavica. Me 100. 92 p.

Daley, C., Tukuri, J. and Riska, K. 1996. Discrete chaotic ice failure model incorporating extrusion effects. Report to National Energy Board, Calgary, Alberta by Daley R&E and Helsinki University of Technology. 44 p. + app.

Edwards, R.Y. 1976. Methods for predicting forces encountered by propellers during interaction with ice. International Shipbuilding Progress, Vol. 23, No 268, pp. 406 - 419.

Enkvist, E. and Johansson, B.M. 1968. On icebreaker screw design. European Shipbuilding, Vol. 16, No 1, pp. 2 - 14.

Finn, D., Jordaan, I.J., Singh, S.K. and Spencer. P. 1989. Flow of crushed ice: Physical and mechanical properties and behaviour, Volume 1: Data collection phase. Volume 2: Analysis of the data. Memorial University of Newfoundland, a report prepared for Canadian Coast Guard, British Petroleum, Esso Resources Ltd., Gulf Canada Resources Ltd., Mineral Management Service, Mobil Research and Development Corporation, National Research Council of Canada and Petro Canada.

Fransson, L., Olofsson, T. and Sandkvist, J. 1991. Observations of the failure process in ice blocks crushed by a flat indentor. Proceedings, The 11th International Conference on Port and Ocean Engineering under Arctic Conditions (POAC), St. John´s, Canada, 24 - 28 September 1991. St. John’s, Canada: Memorial University of Newfoundland. Vol. 1. Pp. 501 - 514.

Gratz, E.T. and Schulson E.M. 1994. Preliminary observations of brittle compressive failure of columnar saline ice under triaxial loading. Annals of Glaciology, vol. 19, pp. 33 - 48.

Hallam, S. 1986. The role of fracture in limiting ice forces. Proceedings, The 8th International Symposium on Ice, IAHR (International Association for Hydraulic Research), Iowa City, Iowa, USA, August 18 - 22, 1986. Vol. II. Pp. 287 - 319.

Hallam, S. and Nadreau J.P. 1987. Failure maps for ice. Proceedings, The 9th International Conference on Port and Ocean Engineering Under Arctic Conditions (POAC), Fairbanks, Alaska, USA, August 17 - 22, 1987. Fairbanks, Alaska: The Geophysical Institute, University of Alaska. Vol. III. Pp. 45 - 55.

Hallam, S. and Pickering, J.G. 1988. Modelling of dynamic ice loading of offshore structures. Proceedings, The International Conference on Technology for Polar Areas (POLARTECH 88), Trondheim. Trondheim: Tapir Publishers. Vol. I. Pp. 235 - 248.

Ignatiev, M.A. 1964. Strength calculations for propeller blades of icebreakers and ice-going vessels. Sudostroenie, January 1964. Pp. 5 - 7. (In Russian.)

Jagodkin, V.J. 1963. Analytical determination of the resistance moment of a propeller during its interaction with ice. Leningrad: Problemy Arktikii i Antarktikii (Problems of the Arctic and Antarctic), vol. 13, pp. 79 - 81. (Translation.)

Joensuu, A. 1988. Ice pressure measurements using PVDF-film. Proceedings, The International Conference on Offshore Mechanics and Arctic Engineering, Houston, USA, February 7 - 12, 1988. New York: ASME. Vol. IV. Pp. 153 - 158.

Joensuu, A. and Riska, K. 1989. Jään ja rakenteen välinen kosketus (Ice structure Contact). Espoo: Laboratory of Naval Architecture and Marine Engineering, Helsinki University of Technology. Report M-88. 57 p. + app. (In Finnish.)

Jones, S.J. 1982. The confined compressive strength of polycrystalline ice. Journal of Glaciology, Vol. 28, No 98, pp. 171 - 177.

Jordaan, I.J. and Timco, G.W. 1988. Dynamics of the ice-crushing process. Journal of Glaciology, Vol. 34, No. 118, pp. 318 - 326.

Jussila, M. 1983. Ice loads on the propulsion system of an ice breaking tug. Proceedings, The 7th International Conference on Port and Ocean Engineering Under Arctic Conditions (POAC). Helsinki, Finland, February 1983. Espoo: Technical Research Centre of Finland, 1983. Pp. 575 - 590. (VTT Symposium 28.)

Jussila, M. and Koskinen, P. 1989 a. Ice loads on CP-propeller shaft of small ferry and their statistical distributions during winter 87. Proceedings, The 8th International Conference on Offshore Mechanics and Arctic Engineering (OMAE 89), The Hague, the Netherlands, March 19 - 23, 1989. New York: ASME. Pp. 351 - 358.

Jussila, M. and Koskinen, P. 1989 b. Ice loads on propeller blades of small car ferry. Proceedings, The 10th International Conference on Port and Ocean Engineering under Arctic Conditions (POAC), Luleå, Sweden, June 12 - 16, 1989. Luleå: Department of Civil Engineering, Luleå University of Technology. Pp. 862 - 872.

Jussila, M. 1991. Jäänleikkuukokeet (Ice cutting tests). Espoo: Technical Research Centre of Finland, VTT Tutkimuksia - Forskningsrapporter - Research Reports 745. 85 p. + app. 12 p. (In Finnish.)

Jussila, M. and Soininen, H. 1991. Interaction between ice and propeller. Espoo: Technical Research Centre of Finland, VTT Tiedotteita - Meddelanden - Research Notes 1281. 80 p.

Juurmaa, K. and Segercrantz, H. 1981. On propulsion and its efficiency in ice. Proceedings SNAME STAR Symposium, Ottawa. SNAME. Pp. 229 - 237.

Kannari, P. 1988. Full scale and model tests performed with nozzle and open propeller simultaneously. Proceedings, The 9th International Symposium on Ice, IAHR (International Association for Hydraulic Research). Sapporo, Japan, 23 - 27 August, 1988. Sapporo: IAHR. Vol. 1. Pp. 772 - 781.

Kannari, P. 1994. Potkurin jääkuormat Itämeren olosuhteissa (Ice loads on propellers in Baltic conditions). Licentiate of Technology Thesis. Espoo: Helsinki University of Technology. 92 p. (In Finnish.)

Kaufmann, W. 1963. Fluid Mechanics. New York, San Fransisco, Toronto, London: McGraw-Hill. 432 p.

Keinonen, A. and Browne, R.P. 1990. Ice propeller interaction forces. Transport Canada Publication TP 10401E. 2 vols. 80 + 165 p.

Koskinen, P. and Jussila, M. 1991. Potkurin lavan jääkuormien pitkäaikaismittaus M/S Gudingenilla (Long term measurements of ice loads on propeller blade of M/S Gudingen), Espoo: Technical Research Centre of Finland, VTT Tiedotteita - Meddelanden - Research Notes 1260. 46 p. + app. 118 p. (In Finnish.)

Koskinen, P., Jussila, M. and Soininen, H. 1996. Propeller ice load models. Espoo: Technical Research Centre of Finland, VTT Tiedotteita - Meddelanden - Research Notes 1739. 82 p. + app. 1 p.

Kotras, T., Humpreys, D., Baird A., Morris, G., and Morley, G. 1985. Determination of propeller-ice milling loads. Proceedings, The 4th International Offshore Mechanics and Arctic Engineering Symposium (OMAE), 1985. New York: ASME, vol. 2. Pp. 336 - 343.

Kujala, P. 1994 a. Modelling of the ice edge failure process with curved failure surfaces. Annals of Glaciology, vol. 19, pp. 158 - 164.

Kujala, P. 1994 b. On the statistics of ice loads on ship hull in the Baltic. Thesis for the degree of Doctor in Technology. Helsinki: Acta Polytechnica Scandinavica. Me 116. 98 p.

Kurdyumov, V.A. and Kheisin, D.E. 1976. Hydrodynamic model of the impact of a solid on ice. Prikladnaya Mekhanika, Vol. 12, No. 10. Pp. 103 - 109. (In Russian.)

Kärnä, T. and Turunen, R. 1989. Dynamic response of narrow structures to ice crushing. Cold Regions Science and Technology, Vol. 17, pp. 173 - 187.

Laskow, V. and Revill, C. 1986. Engineering analysis of ice/propeller interaction data. Report prepared for the Transportation Development Centre. Calgary, Alberta: Canadian Marine Drilling Ltd. Reports TP 844E and TP 8450E.

Laskow, V., Spencer, P.A., Bayly, I.M. 1986. The MV Robert Lemeur ice-propeller interaction project: full scale data. Marine Technology, Vol. 23, No 4, pp. 301 - 319.

Malvern, L.E. 1969. Introduction to the mechanics of a continuous medium. Englewood Cliffs, New Jersey: Prentice-Hall. 713 pages.

Maeno, N. and Ebinuma, T. 1983. Pressure sintering of ice and its implication to the densification of snow at polar glaciers and ice sheets. Journal of Phys. Chem., Vol. 87, pp. 4103 - 4110.

Meaney, R., Kenny, S. and Sinha, N.K. 1991. Medium-Scale Ice-Structure Interaction: Failure zone characterization. Proceedings, The 11th International Conference on Port and Ocean Engineering under Arctic Conditions (POAC), St. John´s, Canada, 24 - 28 September, 1991. St. John’s, Canada: Memorial University of Newfoundland. Vol. I. Pp. 126 - 140.

Muhonen, A., Kärnä, T., Eranti, E., Riska, K., Järvinen, E. and Lehmus, E. 1992. Laboratory indentation tests with thick freshwater ice. Espoo: Technical Research Centre of Finland, VTT Tiedotteita - Meddelanden - Research Notes 1370. 92 p. + app. 106 p.

Newbury, S., Shih, L.Y., Browne, R.P., Revill, C.R., Kenny, S. and Zheng, Y. 1993. Experimental and theoretical evaluation of hydrodynamic pressure during non-contact propeller-ice interaction. Proceedings, The 2nd Canadian Marine Dynamics Conference, Vancouver, Canada, August 9 - 11, 1993. Vancouver: Department of Mechanical Engineering, University of British Columbia. Pp. 157 - 166.

Newbury, S., Browne, R.P. and Jones, S.J. 1994. Experimental determination of hydrodynamic non-contact loads during propeller/ice interaction. Proceedings, ISOPE 94, Osaka, Japan. Colorado: International Society of Offshore and Polar Engineering. Vol. 2. Pp. 596 - 601.

Newbury, S. 1996. JRPA # 6 Propeller/ice interaction, Model test report. St John´s: Institute for Marine Dynamics, report no. CR-1996-03. Vol. 1. 18p + app., vol. 2 app. and vol. 3 app.

Noble, P.G. and Bulat, V. 1981. A Study of ice class rules for propellers. Proceedings, The Propellers 81 Symposium. Virginia Beach, Virginia 26 - 27 May 1981. New York: The Society of Naval Architects and Marine Engineers. Pp. 49 - 65.

Okamoto, H., Shimoyama, N., Yamamoto, F., Nozawa, K., Izízuka, K. and Matsumura, H. 1981 a. Experimental study on propeller ice interaction for ice breaking merchant ship: ice load model experiment. Journal of the Society of Naval Architects in Japan, Vol. 149, No. 4, pp. 100 - 110. (In Japanese.)

Okamoto, H., Nozawa, K., Kawakami, H. and Yamamoto, F. 1981 b. Dynamic ice loads and stress analysis on the propeller of the Arctic ship: model tests in ice. Proceedings, The 6th International Conference on Port and Ocean Engineering under Arctic Conditions (POAC), Quebec City, Canada, 27 - 31 July, 1981. Quebec: Université Laval. Pp. 253 - 262.

Paul, B. 1968. Macroscopic criteria for plastic flow and brittle fracture. In: Liebowitz (Ed.): Fracture, vol II. Academic Press Inc. Pp. 313 - 496.

Pierce, P.E. and Schoff, C.K. 1982. Rheological measurements. In: Kirk-Othmer Encyclopedia of Chemical Technology, vol 20. John Wiley & Sons. Pp. 259 - 319.

Riska, K. 1991. Observations of the line-like nature of ship-ice contact. Proceedings, The 11th International Conference on Port and Ocean Engineering under Arctic Conditions (POAC), St. John´s, Canada, 24 - 28 September, 1991. St. John’s, Canada: Memorial University of Newfoundland. Vol. II. Pp. 785 - 811.

Riska, K., Rantala, H. and Joensuu, A. 1990. Full scale Observations of ship-ice contact. Espoo: Helsinki University of Technology, Laboratory of Naval Architecture and Marine Engineering, Report M-97. 54 p. + app.

Saeki, H. and Ozaki, A. 1980. Ice forces on piles. In: Tryde, P. (Ed.), Physics and Mechanics of Ice. Berlin, Heidelberg, New York: Springer-Verlag. Pp. 342 - 350.

Sanderson, T.J.O. 1988. Ice mechanics, risks to offshore structures. London: Graham & Trotman. 253p.

Sasajima, T., Bulat, V. and Glen, I. 1981. An experimental investigation of two candidate propeller designs for ice capable vessels. Proceedings, The 6th International Conference on Port and Ocean Engineering under Arctic Conditions (POAC), Quebec City, Canada, 27 - 31 July, 1981. Quebec: Université Laval. Pp. 263 - 275.

Sasajima, T. and Mustamäki, E. 1984. Ice-milling load encountered by a controllable pitch propeller. Proceedings, The 7th International Symposium on Ice, IAHR (International Association for Hydraulic Research), Hamburg, 27 - 31 August, 1984. Hamburg: Hamburgische Schiffbau-Versuchsanstalt GmbH. Pp. 281 - 295.

Sasajima, T. 1985. Ice milling loads encountered by a controllable pitch propeller. Mitsubishi Technical Bulletin, No 17. 6 p.

Savage, S.B., Sayed, M., and Frederking, R.M.W. 1992. Two-dimensional extrusion of crushed ice. Part 2: Analysis. Cold Regions Science and Technology, vol. 21, pp. 37 - 47.

Schulson, E.M. 1990. The brittle compressive fracture of ice. Acta Metall. Mater., Vol. 38, No. 10, pp. 1963 - 1976.

Singh, S.K. 1993. Mechanical behaviour of viscoelastic material with changing microstructure. PhD Thesis. Faculty of Engineering & Applied Science, Memorial University of Newfoundland. 195 p.

Singh, S.J., Jordaan, I.J., Xiao, J. and Spencer, P.A. 1993. The flow properties of crushed ice. Proceedings, The International Conference on Offshore Mechanics and Arctic Engineering (OMAE). ASME. Vol. IV. Pp. 11 - 19.

Sinha, N.K. 1979. Grain boundary sliding in polycrystalline materials. Philosophical Magazine, Vol. A 40, No. 6, pp. 825 - 842.

Soininen, H. and Liukkonen, S. 1994. Laboratory tests of pressure distribution around a propeller blade profile during ice contact. Proceedings, The International Shipbuilding Conference, St. Petersburg, Russia, 8 - 12 October, 1994. St. Petersburg: Krylov Shipbuilding Research Institute. Section B. Pp. 90 - 97.

Soininen, H., Liukkonen, S. and Muhonen, A. 1995. Laboratory tests of propeller blade profile pressure distribution under ice contact. Espoo: Technical Research Centre of Finland, Volume I, VTT Tiedotteita - Meddelanden - Research Notes 1664, 70 p. + app. 57 p., Volume II, VTT Tiedotteita - Meddelanden - Research Notes 1665, 324 p.

Soininen, H., Jussila, M., Koskinen, P., Jones, S.J., Newbury, S. and Browne, R. 1998. Propeller-ice interaction. Transactions, The Annual meeting of the Society of Naval Architects and Marine Engineers, Ottawa, Canada, October 15 - 19, 1997. New York: SNAME. Paper 15 (in print). 21 p.

Timco, G.W. and Jordaan, I.J. 1987. Time series variations in ice crushing. Proceedings, The 9th International Conference on Port and Ocean Engineering Under Arctic Conditions (POAC), Fairbanks, Alaska, USA, August 17 - 22 1987. Fairbanks, Alaska: The Geophysical Institute, University of Alaska. Vol I. Pp. 13 - 20.

Tuhkuri, J. and Riska, K. 1990. Results from tests on extrusion of crushed ice. Espoo: Helsinki University of Technology, Laboratory of Naval Architecture and Marine Engineering, report M-98. 47 p.

Tuhkuri, J. 1994. Experimental investigations on extrusion of crushed ice. Proceedings, The 12th IAHR Ice Symposium, Trondheim, Norway. Trondheim: The Norwegian Institute of Technology. Vol. 1. Pp. 474 - 483.

Tuhkuri, J. 1995. Experimental observations of the brittle failure process of ice and ice-structure contact. Cold Regions Science and Technology, Vol. 23, pp. 265 - 278.

Tuhkuri, J. 1996. Experimental investigations and computational fracture mechanics modelling of brittle ice fragmentation. Thesis for the degree of Doctor in Technology. Helsinki: Acta Polytechnica Scandinavica. Me 120. 105 p.

Veitch, B. 1992. Propeller-ice interaction. Licentiate of Technology Thesis. Espoo: Helsinki University of Technology. 102 p.

Veitch, B. and Kivelä, J. 1993. Results of ice cutting experiments with cutting tools representing propeller blade sections. Espoo: Helsinki University of Technology, Laboratory of Naval Architecture and Marine Engineering, report M-183. 167 p.

Veitch, B. and Laukia, K. 1993. The propeller-ice impact process. Proceedings, The 12th International Conference on Port and Ocean Engineering under Arctic Conditions (POAC), Hamburg 17 - 20 August, 1993. Hamburg: Hamburg Ship Model Basin. Vol. I. Pp. 378 - 389.

Veitch, B. 1994. Results of ice cutting experiments with cutting tools representing propeller blade sections. Proceedings, The 12th IAHR Ice Symposium, Trondheim, Norway. Trondheim: The Norwegian Institute of Technology. Vol. I. Pp. 886 - 895.

Veitch, B. 1995. Predictions of ice contact forces on a marine screw propeller during the propeller ice cutting process. Thesis for the degree of Doctor in Technology. Helsinki: Acta Polytechnica Scandinavica. Me 118. 140 p.

Walker, D. and Bose, N. 1994. Hydrodynamic loads and dynamic effects of cavitation on ice class propellers in simulated ice blocked flow. Propellers/Shafting 94 Symposium. SNAME. Pp. 20-1 to 20-19.

Wind, J. 1983. The dimensioning of high power propeller system for Arctic icebreakers and icebreaking vessels. Proceedings, The 5th LIPS Propeller Symposium, Drunen, the Netherlands, 19 - 20 May 1983. Drunen, the Netherlands: LIPS B.V. Paper 9. 32 p.

H.Soininen 25.5.1998

ERRATA

VTT PUBLICATIONS 343
Harri Soininen
A propeller-ice contact model

Page 9

Add to list of symbols

K_{IC}	fracture toughness

Page 10

Printed:

Q_{net}	net mass flow

Corrected:

Q_{net}	net flow rate

Page 29

Printed:

Figure 9. The contact conditions of the tests and the main parameters: α_A *is the angle of attack, w is the width of the cut and* U_P *is the velocity of the blade profile in x-direction (angle of attack direction).*

Corrected:

Figure 9. The contact conditions of the tests and the main parameters: α_A *is the angle of attack, w is the width of the cut (from the kinematic leading edge to the edge of the ice sheet) and* U_P *is the velocity of the blade profile in x-direction (angle of attack direction).*

Page 34

Printed:

Figure 14. Pressure time histories of Test No 9 (basic test) showing the cyclic nature of the pressure. Time histories of sensors No 20 and 21 at the leading edge and 6, 7, 8 and 9 at the back side (No 6 closest to the leading edge) are shown.

Corrected:

Figure 14. Pressure time histories of Test No 9 (basic test) showing the cyclic nature of the pressure. Time histories of sensors No 20 and 21 at the leading edge and 6, 7, 8 and 9 at the back side (No 6 closest to the leading edge) are shown. The triangles indicate the minimum and maximum value of the actual signal and the square the maximum location of the global transversal force.

Page 38

Printed:

Figure 19. Pressure time histories of sensors 6, 7, 8 and 9 of test No 46, confined ice.

Corrected:

Figure 19. Pressure time histories of sensors 6, 7, 8 and 9 of test No 46, confined ice. The triangles indicate the minimum and maximum value of the actual signal and the square the maximum location of the global transversal force.

Page 39.

Printed:

Figure 20. Global transverse and longitudinal loads together with pressure signals from sensors 6 and 7 for test 9 (basic test).

Corrected:

Figure 20. Global transverse and longitudinal loads together with pressure signals from sensors 6 and 7 for test 9 (basic test). The triangles indicate the minimum and maximum value of the actual signal and the square the maximum location of the global transversal force.

Page 53

Printed:

$$\sigma_1 = -S_c + \frac{S_c}{S_t^{'}}\sigma_3 \tag{2}$$

where σ_1 is the major principal stress and σ_3 is the minor principal stress.

Corrected:

$$\sigma_1 = \ \ S_c + \frac{S_c}{S_t^{'}}\sigma_3 \tag{2}$$

where σ_1 is the major principal stress (compressive stresses defined as positive) and σ_3 is the minor principal stress.

Page 56

Printed:

Figure 31. Minor principal stress directions and the relative load distribution; a) unsymmetrical loading, b) symmetrical loading.

Corrected:

Figure 31. Major compressive principal stress directions and the relative load distribution; a) unsymmetrical loading, b) symmetrical loading.

Page 57, first chapter, last sentence

Printed:

Examples of minor principal stress distribution obtained by FE-calculations (performed by the IDEAS program) for these two cases are shown in Figure 31.

Corrected:

Examples of major compressive principal stress distribution obtained by FE-calculations (performed by the IDEAS program) for these two cases are shown in Figure 31.

Page 61, row 14

Printed:

Regardless, the pressures are limited to the melting pressure in the range of strain rates of 0.1 to 1 which were actually reached...

Corrected:

Regardless, the pressures are limited to the melting pressure in the range of strain rates of 0.1 to 1 s^{-1} which were actually reached...

Page 62, 3rd chapter, row 4

Printed:

...the average pressure required for the slip line to occur would be 7.6 MPa according...

Corrected:

...the average pressure required for the slip line to occur would be 6.3 MPa according...

Page 70, 1st chapter, row 14

Printed:

The net mass flow Q_{net} out of the channel and the velocity u for the flow out of the channel during the actual extrusion phase are

Corrected:

The net flow rate Q_{net} out of the channel and the velocity u for the flow out of the channel during the actual extrusion phase are

Page 75, 3rd chapter, 1st row

Printed:

where Q_{net} is the net mass flow.

Corrected:

where Q_{net} is the net flow rate.

Page 81, Equation 43

Printed:

$$hd\sigma_3 = 2\mu pdx$$

Corrected:

$$hd\sigma_3 = -2\mu pdx$$

Page 81, Figure 42

Drawn:

$d\sigma_3$ at the left side of the element

Corrected:

$d\sigma_3$ at the right side of the element

Page 82, 1st row

Printed:

The Equation 45 is valid in the case where $p = 0$ at the outlet of the channel....

Corrected:

The Equation 45 is valid in the case where $\sigma_3 = 0$ at the outlet of the channel....

Page 109

Printed:

Daley, C., Tukuri, J. and Riska, K. 1996. Discrete chaotic ice failure model incorporating extrusion effects. Report to ...

Corrected:

Daley, C., Tuhkuri, J. and Riska, K. 1996. Discrete chaotic ice failure model incorporating extrusion effects. Report to ...